Development of Hydrotalcite-derived Ni Catalysts for the Dry Reforming of Methane at High Temperatures

vorgelegt von
Master of Science
Katharina Mette
geb. in Berlin

Von der Fakultät II - Mathematik und Naturwissenschaften
der Technischen Universität Berlin
zur Erlangung des akademischen Grades

Doktor der Naturwissenschaften
Dr. rer. nat.

genehmigte Dissertation

Promotionsausschuss:

Vorsitzender: Prof. Dr. rer. nat. Peter Strasser
Berichter/Gutachter: Prof. Dr. rer. nat. Robert Schlögl
Berichter/Gutachter: Prof. Dr. rer. nat. Thorsten Ressler
Berichter/Gutachter: Prof. Dr. rer. nat. Martin Muhler

Tag der wissenschaftlichen Aussprache: 15.07.2015

Berlin 2015

Abstract

Catalytic dry reforming of methane (DRM) is an attractive technology for industrial production of synthesis gas, an important feedstock for the production of many basic chemicals. The endothermic reaction operates at high temperatures above 640 °C. On nickel based catalysts high syngas yields are obtained. However, catalyst deactivation by coke formation over Ni based catalysts is still challenging. Deeper understanding of the structure-performance-relationships is needed to integrate the DRM in the well-established downstream syngas chemistry.

This thesis presents a systematic study on the development of a long-term active and thermally stable Ni/MgAl oxide catalyst for the DRM reaction by understanding and optimization of the catalyst synthesis. Regarding the active catalyst, particular emphasis was laid on the understanding of the formation of carbon deposits. By comprehensive structural characterizations of the material in all stages of the preparation, a synthesis route via a Ni,Mg,Al hydrotalcite-like precursor was developed that leads to nanostructuring of the catalytic material. This procedure was successfully applied to Ni/MgAl oxide catalysts with various compositions. Upon high-temperature reduction the catalysts form Ni nanoparticles which are embedded in an oxide matrix and covered by an overlayer. The nature of the overgrowth was investigated applying surface sensitive methods, revealing the presence of predominantly oxidic species. Interestingly, the overgrowth was found to effectively attenuate the carbon formation. Despite coke formation and high Ni loading up to 55 wt.-%, the CH_4 conversion in the DRM at 900 °C was stable over 100 hours. The thermal stability of the Ni nanoparticles is attributed to the embedding nature of the oxide matrix. This allows the high-temperature operation without losing substantial active Ni surface area. Furthermore, the DRM activity, as well as the carbon formation, was strongly depending on the Ni content. The incorporation of a higher amount of Ni was found to increase the activity as well as the coking propensity. By analysis of the spent catalysts thermal and compositional dependencies on the formed carbon species were found. The amount of filamentous carbon decreases with higher reaction temperature and lower Ni content. The carbon formation was found to be a continuous process over the investigated time and caused mainly by methane pyrolysis. From the overall gained insights it can be concluded, that a good catalyst have to make a compromise between activity and coke resistance, which can be controlled by an interplay of Ni dispersion, embedment and metal-support-interactions.

This work demonstrates the relevance of a detailed characterization at all stages of the catalyst preparation, as well as after the reaction, to understand and improve the catalytic performance by rational approaches. The experimental findings give new insights into the current state of reforming knowledge and coke formation and will contribute to the development of advanced catalysts for DRM.

Zusammenfassung

Die katalytische Trockenreformierung von Methan (DRM) ist ein interessantes Verfahren zur industriellen Herstellung von Synthesegas, einem bedeutenden Rohstoff für die Erzeugung von vielen Basischemikalien. Die endotherme Reaktion wird bei hohen Temperaturen über 640 °C durchgeführt. Mit auf Nickel basierenden Katalysatorsystemen werden bereits hohe Synthesegasausbeuten erreicht. Allerdings stellt die Deaktivierung der Katalysatoren durch die Bildung von Koks immer noch eine Herausforderung dar. Ein tieferes Verständnis der Zusammenhänge zwischen Struktur und Eigenschaften wird benötigt, um die DRM in die etablierte Synthesegaschemie zu integrieren.

Diese Arbeit beschreibt eine systematische Studie über die Entwicklung eines langfristig aktiven und thermisch stabilen Ni/MgAl-Oxid Katalysator für die DRM Reaktion. Daher galt besonderes Interesse dem Verständnis und der Optimierung der Katalysatorsynthese. Bezüglich des aktiven Katalysators wurde der Schwerpunkt auf das Verständnis der Bildung von Kohlenstoffablagerungen gelegt. Durch umfassende strukturelle Charakterisierungen der Materialien in allen Stadien der Präparation wurde ein Syntheserezept entwickelt, das über eine Ni,Mg,Al Hydrotalcit-ähnliche Vorstufe zu einer Nanostrukturierung des katalytischen Materials führt. Dieses Verfahren wurde erfolgreich auf Ni/MgAl-Oxid Katalysatoren mit verschiedenen Zusammensetzungen angewandt. Nach der Reduktion bei hohen Temperaturen weisen die Katalysatoren Ni-Nanopartikel auf, die in einer oxidischen Matrix eingebettet sind und von einem Überwuchs bedeckt sind. Die Beschaffenheit des Überwuchs wurde mittels oberflächenempfindlicher Methoden untersucht und zeigt das Vorhandensein von überwiegend oxidischen Spezies. Interessanterweise wurde festgestellt, dass der Überwuchs die Kohlenstoffbildung eindämmt. Trotz der Verkokung und einer hohen Ni Beladung von bis zu 55 Gew% war die CH_4 Umwandlung in der DRM bei 900 °C über 100 Stunden stabil. Die thermische Stabilität der Ni-Nanopartikel wird der einbettenden Eigenschaft der oxidschen Matrix zugeschrieben. Dies ermöglicht den Betrieb bei hoher Temperatur, ohne dass erhebliche Mengen aktiver Ni-Oberfläche verloren gehen. Des Weiteren zeigte die DRM-Aktivität, als auch die Kohlenstoffbildung, eine ausgeprägte Abhängig von dem Ni-Gehalt. Der Einbau höherer Ni-Mengen eröhte sowohl die Aktivität als auch die Verkokungsneigung. Durch Analyse der verwendeten Katalysatoren wurde eine Abhängigkeit der gebildeten Kohlenstoffspezies von der Reaktionstemperatur und der Katalysatorzusammensetzung gefunden. Die Menge von faserförmigem Kohlenstoff nimmt mit höherer Reaktionstemperatur und niedrigerem Ni-Gehalt ab. Es wurde festgestellt, dass die Kohlenstoffbildung ein kontinuierlicher Prozess ist, der hauptsächlich auf die Pyrolyse von Methan zurückzuführen ist. Aus den gewonnenen Erkenntnisse kann geschlossen werden, dass ein guter Katalysator einen Kompromiss zwischen Aktivität und Verkokungsresistenz schließen muss. Dieses Verhalten ist auf ein Zusammenspiel von Ni-Dispersion, Einbettung und Metall-Träger-Wechselwirkungen zurückzuführen.

Diese Arbeit zeigt die Bedeutung einer detaillierten Charakterisierung sowohl in allen Stadien der Katalysatorherstellung als auch nach der Reaktion, um die Katalysatoreigenschaften durch rationale Ansätze zu verbessern. Die experimentellen Ergebnisse liefern neue Erkenntnisse zum aktuellen Stand des Wissens in der Trockenreformierung und insbesondere die Bildung von Koks und werden zu der Entwicklung von verbesserten Katalysatoren für die DRM beitragen.

Contents

1 Introduction

CO_2 is the most abundant substance produced by human activities. Especially fossil power plants emit large amounts of the greenhouse gas CO_2, with global warming implications. Its further accumulation in the atmosphere must be avoided in order to prevent reinforcement of the global warming. In the last century, much attention has been paid to reduce and utilize CO_2 emissions [1]. In order to improve climate conditions, the concept of *Carbon Capture and Utilization* (CCU) is aimed to recycle anthropogenic CO_2 as a feedstock for chemical production [2]. This includes the utilization of CO_2 as a C1-source. As CO_2 is a thermodynamically very stable compound (free energy: -394.01 kJ mol^{-1} [1]), its activation requires significant amounts of energy. In terms of sustainability, CO_2 activation only makes sense if the energy is mainly produced from renewable sources. It is especially required to develop economical and effective ways to chemically retain large quantities of CO_2. One option that is considered is the catalytic conversion of CO_2 to produce *synthesis gas* (syngas) – a gas mixture of primarily CO and H_2.

1.1 Syngas

Syngas is a raw material for the production of a number of materials such as methanol, ammonia, diesel fuels or synthetic gasoline (Fischer-Tropsch process) in catalytic processes [3]. Furthermore, syngas can be burned, e.g. in gas turbines, to produce electricity and heat or can directly be used as H_2 source. In Hydroformylation reactions (oxo synthesis) of alkenes, syngas is used to produce aldehydes [3]. Depending on the application, different H_2/CO ratios are required. Different syngas production processes are available, that give different H_2/CO ratios. Furthermore, the H_2/CO ratio can be adjusted by the water gas shift reaction, subsequently.

Commercially used methods for syngas production are especially the steam reforming of natural gas (SMR – eq. (1.1)) and to some extend the gasification of coal (eq. (1.2)) [4]. Though, these processes are characterized by a high consumption of fossil fuels and high energy needs, which are provided by combustion of additional fossil fuels. Alternative routes, such as the partial oxidation of methane (POM – eq. (1.3)) or the dry reforming of methane (DRM – eq. (1.4)) are attractive alternatives [5]. In contrast to the commercial processes, the former is an exothermic reaction with less energy needs and the latter one is capable to transform CO_2 directly, though, it is highly endothermic as well.

Methane steam reforming: $CH_4+H_2O \rightarrow CO+3\ H_2$ $\Delta H_0 = 206.2\ kJ\ mol^{-1}$ (1.1)
Gasification of coal: $C+H_2O \rightarrow CO+H_2$ $\Delta H_0 = 131.3\ kJ\ mol^{-1}$ (1.2)
POM: $2\ CH_4+O_2 \rightarrow 2\ CO+4\ H_2$ $\Delta H_0 = -35.7\ kJ\ mol^{-1}$ (1.3)
Dry Reforming of Methane: $CO_2+CH_4 \rightarrow 2\ CO+2\ H_2$ $\Delta H_0 = 247.3\ kJ\ mol^{-1}$ (1.4)

1.2 Dry Reforming of Methane

Production of synthesis gas from CH_4 and CO_2 was first suggested in 1928 by Fischer and Tropsch [6] who were interested in an alternative process to coal gasification. Nowadays, the catalytic reforming of methane with carbon dioxide (eq. (1.4)) is of great interest [7], because it consumes two greenhouse gases simultaneously, CO_2 and CH_4. Furthermore, the reforming with CO_2 produces a syngas with a H_2/CO ratio of equal to or less than unity, which is especially preferable for hydroformylation reactions (oxo synthesis) of alkenes to aldehydes [8] and Fischer-Tropsch reactions of long chain alkanes [9]. The reaction equilibrium is typically influenced by the simultaneous occurrence of the reverse water-gas shift reaction (RWGS – eq. (1.5)) which lowers the H_2/CO ratio [7]. The DRM reaction is highly endothermic and therefore requires low pressures, but very high temperatures. In equilibrium state, the minimal temperature for the DRM reaction is 640 °C [10,11]. The RWGS reaction can proceed only up to 820°C [12]. Depending on the operating temperature and reactant partial pressures, other side reactions can form solid carbon (coke) during DRM [10], either by CH_4 pyrolysis (eq. (1.6)), or CO disproportionation (Boudouard reaction – eq. (1.7)), as discussed in more detail in chapter 1.2.2.

RWGS reaction: $CO_2+H_2 \longrightarrow CO+H_2O$ $\Delta H_0 = 41.2\ kJ\ mol^{-1}$ (1.5)
Methane pyrolysis: $CH_4 \longrightarrow C+2\ H_2$ $\Delta H_0 = 74.9\ kJ\ mol^{-1}$ (1.6)
Boudouard reaction: $2CO \longrightarrow C+CO_2$ $\Delta H_0 = -172.5\ kJ\ mol^{-1}$ (1.7)

Different mechanisms of the DRM reaction have been reported in literature, depending on the catalyst, the temperature and the partial pressure used. Cui et al. [13] investigated the mechanism of the DRM under conditions close to which was used in this thesis. They used a typical Ni/α-Al_2O_3 catalyst in a temperature range of 550–750 °C, using steady-state and transient kinetic methods. In the high temperature region between 650 and 750 °C, they proposed the following dual-site reaction mechanism (without considering RWGS):

methane adsorption and dissociation on metal sites ($*_m$):

$$CH_4 + (5-x)\ *_m \leftrightarrow CH_x*_m + (4-x)\ H*_m \quad (1.8)$$

CO_2 chemisorption and dissociation on the support or at the metal-support interface ($*_s$):

$$CO_2 + *_s \longrightarrow CO + O*_s \tag{1.9}$$

moving of surface oxygen species to metal sites to react with CH_x species:

$$O*_s + *_m \longrightarrow O*_m + *_s \tag{1.10}$$

$$O*_m + CH_x*_m \longrightarrow CO + {}^{x}/_{2}\, H_2 + 2\ *_m \tag{1.11}$$

the reaction between CH_x and CO_2 was revealed as the rate-determining step (rds):

$$CH_x*_m + CO_2 + (x+1)*_m \longrightarrow 2\ CO*_m + x\ H*_m \qquad \text{(rds)} \tag{1.12}$$

$$n\ CH_x*_m \longrightarrow (CH_x)n*_m \tag{1.13}$$

rapid CO and H_2 desorption:

$$CO*_m \leftrightarrow CO + *_m \tag{1.14}$$

$$2\ H*_m \leftrightarrow H_2 + 2\ *_m \tag{1.15}$$

1.2.1 Dry Reforming Catalysts

Most catalyst systems, which are already developed for the DRM reaction, are so-called “low temperature catalysts”, due to their poor thermal stability. As already mentioned, the DRM reaction is an endothermic reaction. Therefore, high temperatures will facilitate the formation of syngas and the development of high temperature stable catalysts is required. Supported transition metal-based catalysts (Ni, Co, Fe) as well as noble metal-based catalysts (Rh, Ru, Pd, Pt, Ir) were found to be highly active in DRM [14,15,16,17]. Catalysts based on noble metals are reported to be less sensitive to coke formation than non-noble metal based catalysts [18]. Especially nickel efficiently catalyzes the deposition of carbon [19]. However, considering the high cost and limited availability of precious metals, it is more profitable to develop and improve basic metal catalysts. Among them, Ni-based catalysts are the usual choice of catalytic material, due to its low cost, its natural abundance and high activity. Though, after decades of research, carbon formation over nickel catalysts is still not sufficiently understood and its prevention requires a systematic solution.

1.2.2 Catalyst deactivation and carbon deposition

Among coking there are several other reasons for catalyst deactivation, like sintering of metal particles, poisoning, or encapsulation of the active metal by reducible supports [9].

However, carbon deposition is the most significant catalyst deactivation source in DRM. There are mainly two reactions that result into carbon formation; methane pyrolysis (eq. (1.6)) and the CO disproportionation (Boudouard reaction – eq. (1.7)). Because of thermodynamics, higher temperature favors the formation of carbon due to methane pyrolysis.

It is proposed [20,21], that carbon formation from hydrocarbons proceeds by decomposition on late transition metal surfaces, such as nickel [22]. Carbon atoms are dissolving into the metal lattice forming solid solutions. Nucleation of carbon atoms on the rear interface leads to carbon formation [4,23]. As carbon formation takes place on different surface sites and by different reaction routes, various types of carbon can be formed [4]. The type of carbon depends also e.g. on the reaction temperature, choice of metal and support and on the concentration of the active species [4]. It is proposed that graphitic and less ordered carbon are mainly responsible for deactivation due to surface blocking and encapsulation of Ni particles. Carbon nanofibers (CNFs) in contrast are suggested to be mainly result in breakdown of the catalyst pellet [4]. Mainly two different CNF growth modes exist. At low metal particle-support interactions, CNFs can form with a Ni particle on top (tip growth). CNFs can also grow upward from the particle while it remains attached to the support (root growth) [24].

To attenuate carbon deposition on nickel catalysts several attempts have been made. Carbon formation by CH_4 pyrolysis can only occur above 557 °C and by the Boudouard reaction below 700 °C [10]. Thus, by applying suitable conditions, carbon deposition can be thermodynamically unfavorable. To avoid carbon deposition, high temperatures should be used. Gadalla et al. [11] reported on a limiting reaction temperature for carbon formation of 805 °C for a CO_2/CH_4 ratio of 1.2 at 1 bar. The temperature limit increases as the CO_2/CH_4 feed ratio decreases and as the pressure increases. Thus, it is recommended to use excess CO_2 in the feed.

Other approaches have aimed at tuning the properties of Ni catalysts, e.g. by using alkali metal oxide promoters, such as MgO [25], basic supports [26], Ni alloying [27,28,29], doping with metal oxides that exhibits high oxygen storage capacities like CeO_2 [30,31] or by adjustments in the catalyst preparation [32,33]. Furthermore, for the catalyst design it is important to consider the synergy of size [34], morphology, structure, and composition [35]. Carbon formation by CH_4 pyrolysis is a structure sensitive reaction [36]. This offers the possibility to inhibit carbon formation by modifications of the surface structure. E. g. by the selective poisoning of metal surface sites with sulfur [37] that can inhibit coke formation. Several attempts have been made to suppress coke formation on Ni catalysts using different supports. The addition of basic promoters such as CaO or MgO to Ni supported on Al_2O_3 can increase the activity and reduce carbon formation [38,39]. The Lewis basicity of these promoters enhances the chemisorption of CO_2 [40], a characteristic that is proposed to reduce the Boudouard reaction. The relation of carbon deposition and the catalyst structure was studied by Chen and Ren [41] for a Ni/Al_2O_3 catalyst. They reported on the influence of strong Ni-Al_2O_3 interactions on the catalytic properties during DRM at 750 °C. The formation of a $NiAl_2O_4$ spinel after calcination was found to have a suppressing effect on the carbon formation [42].

1.3 Layered double hydroxides (LDHs)

Layered double hydroxides (LDHs) are promising reforming catalyst precursors as they possess a homogeneous elemental distribution and high surface areas [43]. Upon calcination they form a spinel framework which provides a high thermal stability. LDHs are anionic clays with inter-layer spaces containing exchangeable anions. They are promising materials for a large number of applications, due to a large variety of compositions, low cost and a wide range of preparation variables that provides customized materials for specific requirements. After controlled thermal decomposition, homogeneous mixed oxides with high surface areas (100-300 $m^2\ g^{-1}$) are obtained, which are thermally stable. By further reduction of the material, small and stable metal crystallites can be obtained. Because of its properties it is suitable for many industrial applications, but especially as precursors for catalysts or catalyst supports.

1.3.1 Structure of LDHs

Layered double hydroxides (LDHs) are also known as hydrotalcite-like (htl) compounds. The hydrotalcite itself is a hydroxy carbonate of the general formula $Mg_6Al_2(OH)_{16}CO_3 \cdot 4\ H_2O$. Is structure is related to that of brucite ($Mg(OH)_2$, CdI_2 type), where octahedra of Mg^{2+}, coordinated to 6 OH^-, share edges to form infinite sheets, with the hydroxide ions sitting perpendicular to the plane of the layers (Figure 1.1) [44]. The sheets stack on top of one another, held together by weak interactions through the hydrogen atoms to form a three-dimensional structure. The brucite-like sheets may be stacked in different ways, which gives rise to a variety of possible polytype structures. Two different stacking sequences are often found, rhombohedral (3R: BC-CA-AB-BC) or hexagonal (2H: BC-CB-BC).

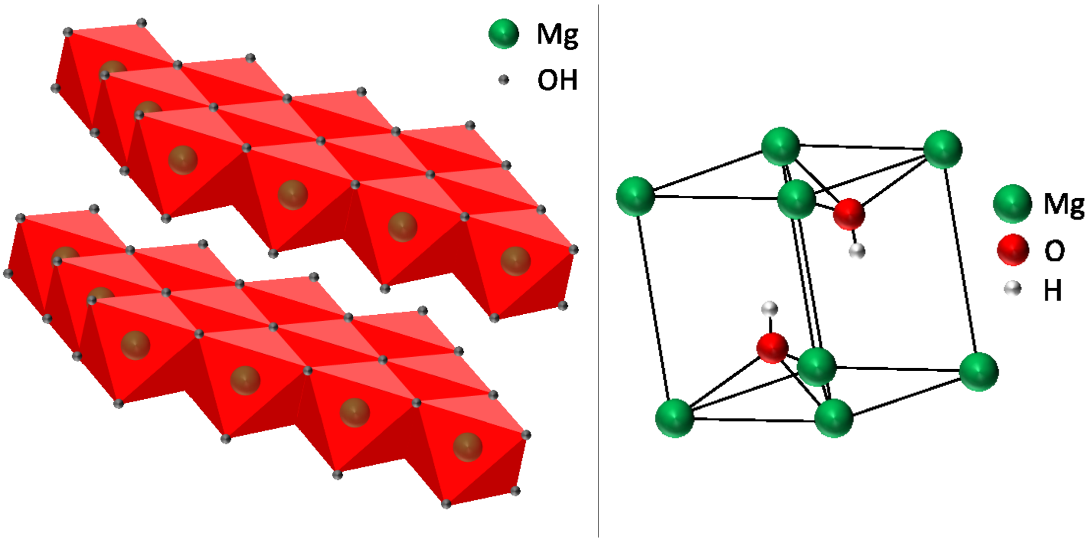

Figure 1.1: Schemata of brucite structure.

In LDHs Mg^{2+} ions are substituted by a trivalent cation, such as Al^{3+}. Thereby a positive charge is generated in the hydroxyl sheet, which is compensated by anions like CO_3^{2-}. The anions as well as water are randomly located in the interlayer between the brucite-like sheets (Figure 1.2A). The bonding between the hydroxyl groups of the octahedral layers and the interlayer ions involves a combination of electrostatic effects and hydrogen bonding [45]. The hydroxyls are tied to the interlayer anions directly or via H_2O intermediates, using hydrogen bridges (Figure 1.2B) [46]. The carbonate groups themselves are arranged flat in the interlayer [43].

The possibility of varying the di- and trivalent cations, as well as the identity of the interlayer anions leads to a large variety of materials having the general formula $[M^{II}_{1-x}M^{III}_{x}(OH)_2]^{x+}[A^{n-}]_{x/n} \cdot y\ H_2O$ and belonging to the LDH family. Recently, it has been shown that tetravalent cations such as Zr^{4+} and Sn^{4+} could also be incorporated into the brucite-like LDH-layer [47,48]. Furthermore, it is also possible to synthesize ternary, quaternary and multicomponent LDHs.

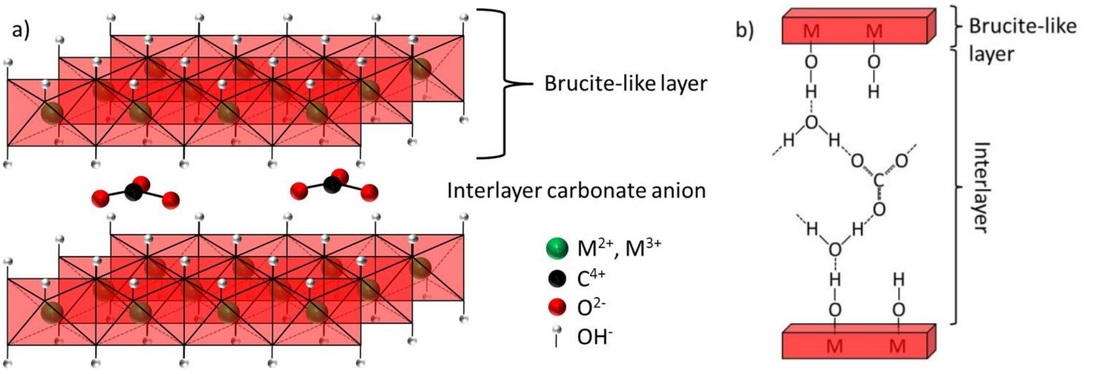

Figure 1.2: a) Schema of hydrotalcite-like structure, b) Possible sterical relationship between of CO_3^{2-} ions, H_2O molecules and OH^- groups in the interlayer.

Most metals in the first period of transition metals can form LDHs, as long as they fit into the octahedral spaces of the brucite-like sheets (ionic radius of approx.: 0.5 - 0.8 Å), like Mg^{2+}, Ni^{2+}, Zn^{2+}, Cu^{2+}, Co^{2+}, Al^{3+}, Fe^{3+} and Cr^{3+} [43]. Larger cations may destabilize the LDH structure or even inhibit its formation. Likewise electrostatic M^{3+}-M^{3+}- and M^{3+}-M^{2+}-interactions are a limiting factor for the formation of pure LDHs. Thus, in most of the cases the M^{3+} content varies in the range of $0.20 \leqq x \leqq 0.33$ [43].

Practically, there is no limitation to the intercalation of all types of anions into the LDH structure. The size, the orientation and the quantity of the anions define the thickness of the interlayer. The following families of anions are known [43]:

i) halides: F^-, Cl^-, Br^-, I^-
ii) oxoanions: CO_3^{2-}, NO^{3-}, SO_4^{2-}, ClO^{4-}, CrO_4^{2-}, MnO^{4-}, …
iii) anionic complexes: $[Fe(CN)_6]^{2-}$, $[PdCl_4]^{2-}$, …
iv) organic anions: CH_3COO^-, $C_2O_4^{2-}$, $C_6H_5SO^{3-}$, …
v) anionic polymers: PSS, PVS, …

The interlayer region is less stable then the brucite-like sheets, and therefore the LDHs have the ability to undergo anionic exchange reactions. This is used in a wide range of applications, especially in the removal of toxic anions from aqueous systems [49].

1.3.2 Synthesis of LDHs

A variety of methods exist for LDH production such as co-precipitation, urea reduction, induced hydrolysis, sol-gel technique as well as hydrothermal, microwave or ultrasound treatment [50]. Co-precipitation is one of the most important methods for the synthesis of solid catalyst precursors, based on more than one component. A subsequent calcination and/or reduction step generates the final catalyst, usually with very small and intimately mixed crystallites of the components.

1.3.3 Thermal decomposition of LDHs

Most LDHs show a similar thermal decomposition behavior. From thermogravimetry (TG) experiments of Mg-Al LDH it is known [51], that up to approximately 250 °C interlayer water is released, followed by the dehydroxylation of the brucite-like layers and the decarboxylation of the interlayer up to around 400 °C, resulting in the conversion to a mixed-oxide MgO-like phase. Above 900 °C a crystalline spinel ($MgAl_2O_4$) and $M^{II}O$ are formed. Besides, Stanimirova et al. [52] suggested in 1999 the formation of a metaphase at temperatures between 240 and 260 °C, probably due to grafting of carbonate anions to the hydroxide layers after partial dehydroxylation of OH groups of the brucite-like layers.

The most interesting properties of hydrotalcites arise when they are calcined (< 600°C [53]). This process removes the interlayer water, interlayer anions and the hydroxyls. The resulting material is a homogeneous mixture of metal oxides with a high surface area and the structure is directly related to the arrangement of the metals in the hydrotalcite. Thirty years ago, studies have shown that the calcined product can be re-hydrated in an aqueous solution to return to the LDH structure by insertion of the present anion [54]. This so-called "memory effect" can be used effectively to remove harmful anions, both organic and inorganic, from wastewater solutions.

1.3.4 Ni LDHs as reforming catalyst precursors

In recent years, a considerable amount of literature has been published on the application of hydrotalcite derived Ni catalysts for the dry reforming reaction. Takehira et al. carried out a number of investigations into the topic. In 2001 [55] they reported on a high activity and stability in the DRM using supported Ni catalysts with a fixed Ni/Mg ratio of 0.5 prepared from Ni-Mg-Al hydrotalcite-like precursors. Impregnated Ni/α-Al_2O_3 and Ni/MgO catalysts showed comparatively low activities. However, a catalyst prepared by impregnation of Ni on Mg–Al mixed oxide prepared from Mg–Al hydrotalcites (ht) showed a comparable activity. This behavior is explained by a possible regeneration of the hydrotalcite phase during the preparation, resulting in an incorporation of Ni^{2+} in the Mg^{2+} sites of the ht.

In the following years these materials were also successfully tested in steam reforming of CH_4 [56] as well as in the partial oxidation and autothermal reforming of CH_4 into synthesis gas [57]. Autothermal reforming of methane (ATR) can be defined as the combination of SMR and POM.

In 2003 Takehira et al. [58] presented a new synthesis of Ni-Mg-Al hydrotalcites where nickel was introduced via precomplexation with an $EDTA^{4-}$ ligand. The corresponding Ni-Mg-Al mixed oxides demonstrated high and stable catalytic activity and selectivity in dry reforming of methane at 800 °C. Furthermore, they observed that only 5.3 wt% coke was formed after 6 h at 800 °C.

In 2005 the group of Takehira [59,60] reported on another synthesis method where Mg-Al particles, derived from hydrotalcites, were dipped into an aqueous solution of Ni(II) nitrate. Dipping at low pH led to the formation of egg shell-type Ni-loaded catalysts that showed a high and stable activity in the steam reforming of CH_4. It is concluded that the high activity is mainly due to the enrichment of highly dispersed Ni metal particles in the surface layer of the catalyst particles.

Also other groups addressed themselves to this topic. Perez-Lopez et al. [61] investigated that the catalytic properties of Ni-Mg-Al catalysts, derived from hydrotalcites, are influenced by the M^{II}/M^{III} ratio and the Ni/Mg ratio, as well as by the calcination and reduction temperature. The differences in the catalytic properties due to these parameters affect simultaneously the crystallite size and the acid–base character of the surface. They obtained the best results for CO_2 reforming of methane at 700 °C for Ni-Mg-Al samples having a Ni/Mg ratio between 1 and 5, a Mg/Al ratio of at least 1/3 (for M^{II}/M^{III} at around 2) and if the thermal treatment was carried out at 600 °C for calcination and at 700 °C for reduction.

1.4 Co-precipitation

According to IUPAC nomenclature co-precipitation is the simultaneous precipitation of a normally soluble component with a macro-component from the same solution by the formation of mixed crystals, by adsorption, occlusion or mechanical entrapment [62].

The main advantages of precipitation are the possibility of creating very pure materials, the flexibility of the process with respect to the final product quality and the generation of homogeneous distributions of the components with a defined stoichiometry [63]. However, precipitation is usually more demanding than other preparation techniques, due to the necessity of product separation after precipitation and the large volumes of salt-containing solutions generated.

The simplest way of precipitation is the batch operation, where the metal solution is present in the precipitation vessel and the precipitating agent is added or the other way around. The main drawback is the formation of different products during the initial state of the precipitation and at the end of the process, because of the variation of the batch composition [63]. If a co-precipitation is carried out this way, it is important, that the precipitating agent is present in the precipitation vessel and the metal solution is added. In this case, the precipitating agent is always present in supersaturation, leading to a homogeneous product.

A more complex process with the simultaneous addition of both reagents under strict control of the pH and the temperature usually leads to a better homogeneity [63]. The ratio of the metal salt and precipitating agent stays constant, whereas the concentrations of the ions that are not precipitated are changing during the process. Generally, all process parameters influence the properties of the final product, like the chemical composition, the formed phase, the particle size, the pore size, the surface area, the purity and many more. Therefore, it is necessary to optimize the process parameters in order to produce the desired product.

The optimization results mostly from empirical studies. The parameters, which are affecting the properties mainly, are summarized in Figure 1.3.

High concentrations of the metal ions increase the rate of precipitation and smaller particles with higher surface areas are obtained due to increased nucleation rates [43]. Furthermore, the composition of the solutions determines the composition of the final catalyst. Hence, the choice of counterions is one important parameter. Preferably nitrates of metal precursors, which can be easily decomposed, are used as metal sources, and ammonia or sodium hydroxide and carbonate as precipitating agent. For catalytic applications, ions like chlorides or sulfates are unlikely, because they can act as poisons in the catalytic reaction.

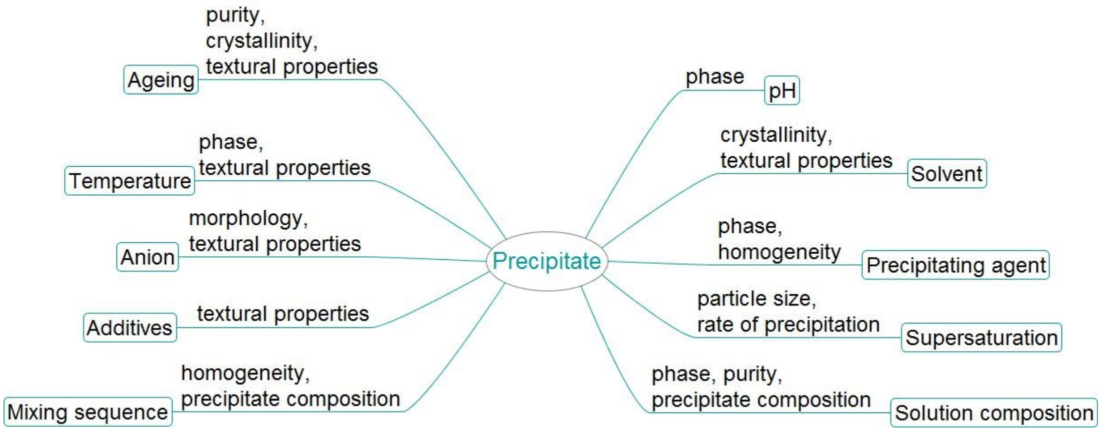

Figure 1.3: Parameters affecting the properties of the precipitate.

Another crucial determining factor is the precipitation temperature, which can control crystallite sizes and phase formations. Usually, most precipitations are carried out above room temperature, due to an increased precipitation rate at higher temperatures [63]. Nevertheless, a temperature increase can also lead to an increased crystallite size, depending on the kinetics of the formation of the precipitate. Thus, the ideal precipitation temperature has to be found experimentally. How the properties of the final precipitate are influenced by the precipitation pH, with respect to the catalytic properties, is not clear yet. Though, it is well known that it is one of the decisive factors that control the nature of the phase. Baltes et al. [64] e.g. systematically investigated the influence of precipitation parameters such as pH and precipitation temperature on Cu/ZnO/Al_2O_3 catalysts. They found correlations between the synthesis conditions, the catalyst structure and even the catalytic performance. Ageing time and conditions are at least equally important as the other factors. During ageing – the time period within which the precipitate is left in the mother liquor – the particle size can increase and initially amorphous precipitates can crystallize [63].

1.5 Objective

The work was carried out within the scope of the CO_2RRECT project (CO_2-Reaction using Regenerative Energies and Catalytic Technologies), funded by the German Federal Ministry of Education and Research (BMBF – Bundesministerium für Bildung und Forschung). Within the CO_2RRECT project coal derived CO_2 conversion technologies are developed, using renewable energies to optimize the overall energy balance of the processes. The key methods are the RWGS reaction to CO, the hydrogenation of CO_2 to formic acid and the DRM reaction to syngas.

The present thesis focusses on systematic studies to develop long-term active and thermally stable noble metal free catalysts for the dry reforming reaction of methane (DRM). After decades of research, coking during DRM over nickel catalysts is still challenging and its prevention requires a systematic solution. As already mentioned in Chapter 1.2.2, a promising way of suppressing carbon formation is to perform the DRM reaction at high reaction temperatures. Thermodynamically, 805 °C is the limiting temperature below which carbon formation is possible [11]. Thus, materials are needed which are thermally stable against sintering at more elevated temperatures. Our synthetic approach to stabilize Ni nanoparticles at high temperatures is to incorporate them into a stable oxide matrix, a concept that has previously been applied to Ni-containing perovskites [65] and spinels [66]. To achieve strong interfacial interactions between the metal and the oxide a stabilizing partial embedding of the Ni particles is attempted via the formation of both catalyst components from a single phase precursor with a mixed cationic lattice and decomposable anions. Accordingly, Ni based catalysts established from hydrotalcite-like precursors with the nominal composition of $Ni_xMg_{0.67-x}Al_{0.33}(OH)_2(CO_3)_{0.17}\cdot mH_2O$ are intended to be prepared by pH controlled co-precipitation. This approach is based on the pioneering work by Kühl et al. [67,68] on Cu/ZnAlO$_x$ catalysts from hydrotalcite-like precursors for methanol synthesis. To gain insights into the microstructure and composition, comprehensive structural characterizations of the obtained materials have to be performed. Catalytic DRM tests are to be carried out at high temperatures and particular interest is to be devoted to the understanding of the formation of carbon deposition on the nickel based catalysts. Furthermore, by the preparation of a series of catalysts with different composition an understanding can be provided concerning the structural and compositional influences on the catalytic performance, as well as on the coking behavior.

1.6 Outline of the Thesis

This work represents a successful scientific collaboration within the CO_2RRECT project between the Ruhr-Universität in Bochum and the Inorganic Chemistry Department of the Fritz-Haber-Institut in Berlin. The group of Professor Martin Muhler, namely Hendrik Düdder and Kevin Kähler from the Laboratory of Industrial Chemistry at the Ruhr-Universität contributed to the publications this thesis is based on with all catalytic measurements and provided the arising spent samples. The thesis is composed of four cumulative chapters, each dealing with another aspect of a coherent study, presenting the major findings of the present work. The Chapters are adopted from publications that cover the results obtained during this doctoral thesis. A detailed listing of the personal contributions is given in the appendix.

After a short introduction and motivation in **Chapter 1**, a comprehensive structural characterization of a Ni rich Ni/MgAlOx catalyst is described **Chapter 2** [69] using multiple characterization techniques. The thermal stability of its microstructure as well as the catalytic performance was investigated in detail. In **Chapter 3** a comprehensive structural characterization of a series of Ni/MgAlOx catalysts with different composition is described using multiple characterization techniques. By the employment of surface sensitive techniques (HR-TEM and IR), we were able to show that an oxidic overgrowth is formed on the Ni particles. The observed surface properties of the Ni based catalysts were used to propose structure-performance-relationships. Furthermore, a systematic characterization of carbon deposition during catalytic DRM is presented. **Chapter 4** [70] investigates the influence of the endothermic DRM reaction on the temperature distribution in the catalyst bed by measuring axial temperature profiles and simulations based on computational fluid dynamics (CFD). Furthermore, by investigation of spent catalysts with transmission electron microscopy (TEM) and temperature-programmed oxidation (TPO) experiments the formation of different carbon species was detected, depending on the catalyst composition and the reaction temperature. **Chapter 5** [71] describes a methodological approach to address the structural stability and the catalytic properties of a Ni-based DRM catalyst at high reaction temperatures. With this approach the effect of catalyst ageing is decoupled from the structural effects induced by coking, e.g. by enhanced metal mobility during carbon filament growth. Finally, the main findings are summarized and discussed in **Chapter 6**.

1.7 References

[1] Y. Sun, in *Carbon Dioxide Utilization for Global Sustainability*, ed. S.-E. Park, J.-S. Chang, K.-W. Lee, Vol. 153, Elsevier, Amsterdam, **2004**, 9-17.

[2] P. Markewitz, W. Kuckshinrichs, W. Leitner, J. Linssen, P. Zapp, R. Bongartz, A. Schreiber, T. E. Müller, *Energy Environ. Sci.* **2012**, 5, 7281–7305.

[3] I. Wender, *Fuel Process. Technol.* **1996**, 48, 189-297.

[4] J. Rostrup-Nielsen, L. J. Christiansen in *Concepts in Syngas Manufacture*, Vol. 10 (Ed.: G. J. Hutchings), Imperial College Press, London, **2011**, pp. 219–227.

[5] A. P. E. York, T. Xiao, M. L. H. Green, *Top. Catal.* **2003**, 22, 345-358.

[6] F. Fischer, H. Tropsch, *Brennst.-Chem.* **1928**, 3, 39-46.

[7] M. C. J. Bradford, M. A. Vannice, *Catal. Rev.: Sci. Eng.* **1999**, 41, 1-42.

[8] J.-M. Wei, B.-Q. Xu, J.-L. Li, Z.-X. Cheng, Q.-M. Zhu, *Appl. Catal., A* **2000**, 196, 167-172.

[9] D. Pakhare, J. Spivey, *Chem. Soc. Rev.* **2014**, DOI: 10.1039/ c3cs60395d.

[10] S. Wang, G. Q. Lu, G. J. Millar, *Energy Fuels* **1996**, 10, 896-904.

[11] A.M. Gadalla, B. Bower, *Chem. Eng. Sci.* **1988**, 43, 3049-3062.

[12] A. S. Al-Fatesh, A. A. Ibrahim, S. Haider, A. H. Fakeeha, *J. Chin. Chem. Soc.* **2013**, 60, 1297-1308.

[13] Y. Cui, H. Zhang, H. Xu, W. Li, *Appl. Catal., A* **2007**, 318, 79-88.

[14] O. Tokunaga, S. Ogasawara, *React. Kinet. Catal. Lett.* **1989**, 39, 69-74.

[15] A. Djaidja, S. Libs, A. Kiennemann, A. Barama, *Catal. Today* **2006**, 113, 194-200.

[16] D. Qin, J. Lapszewicz, *Catal. Today* **1994**, 21, 551-560.

[17] P. M. Torniainen, X. Chu, L. D. Schmidt, *J. Catal.* **1994**, 146, 1-10.

[18] J. R. Rostrup-Nielsen, J.-H. Bak Hansen, *J. Catal.* **1993**, 144, 38-49.

[19] J. R. Rostrup-Nielsen, D. L. Trimm, *J. Catal.* **1977**, 48, 155-165.

[20] S. Helveg, C. López-Cartes, J. Sehested, P. L. Hansen, B. S. Clausen, J. R. Rostrup-Nielsen, F. Abild-Pedersen, J. K. Nørskov, *Nature* **2004**, 427,426- 429.

[21] S. Hofmann, R. Blume, C. T. Wirth, M. Cantoro, R. Sharma, C. Ducati, M. Hävecker, S. Zafeiratos, P. Schnoerch, A. Oestereich, D. Teschner, M. Albrecht, A. Knop-Gericke, R. Schlögl, J. Robertson, *J. Phys. Chem. C* **2009**, 113, 1648-1656.

[22] R. Schlögl, *Adv. Catal.* **2013**, 56, 103-185.

[23] A. Rinaldi, J.-P. Tessonnier, M. E. Schuster, R. Blume, F. Girgsdies, Q. Zhang, T. Jacob, S. B. Abd Hamid, D. S. Su, R. Schlögl, *Angew. Chem. Int. Ed.* **2011**, 50, 3313-3317.

[24] J.-P. Tessonnier, D. S. Su, *ChemSusChem* **2011**, 4, 824–847.

[25] S. Wang, G.Q. Lu, J. *Chem. Technol. Biotechnol.* **2000**, 75, 589-595.

[26] S. Wang, G.Q. Lu, *Energy Fuels* **1998**, 12, 248-256.

[27] J.-H. Lee, E.-G. Lee, O.-S. Joo, K.-D. Jung, *Appl. Catal., A* **2004**, 269, 1–6.

[28] E. Nikolla, J. Schwank, S. Linic, *J. Catal.* **2009**, 263, 220–227.

[29] P. Djinović, I. G. O. Črnivec, B. Erjavec, A. Pintar, *Appl. Catal., B* **2012**, 125, 259–270.

[30] S. Wang, G.Q. Lu, *Appl. Catal., B* **1998**, 19, 267-277.

[31] N. Laosiripojana, W. Sutthisripok, S. Assabumrungrat, *Chem. Eng. J.* **2005**, 112, 13–22.

[32] S. Wang, G. Q. M. Lu, *Appl. Catal., B* **1998**, 16, 269-277.

[33] J. Chen, R. Wang, J. Zhang, F. He, S. Han, *J. Mol. Catal. A: Chem.* **2005**, 235, 302–310.

[34] J.-H. Kim, D. J. Suh, T.-J. Park, K.-L. Kim, *Appl. Catal., A* **2000**, 197, 191–200.

[35] C.-j. Liu, J. Ye, J. Jiang, Y. Pan, *ChemCatChem* **2011**, 3, 529-541.

[36] C. H. Bartholomew, *Catal. Rev.-Sci. Eng.* **1982**, 24, 67-112.

[37] J. R. Rostrup-Nielsen, *J. Catal.* **1984**, 85, 31-43.

[38] Z. L. Zhang, X. E. Verykios, *Catal. Today* **1994**, 21, 589.

[39] S.-B. Tang, F.-L. Qiu, S.-J. Lu, *Catal. Today* **1995**, 24, 253.

[40] G. J. Kim, D.-S. Cho, K.-H. Kim, J.-H. Kim, *Catal. Lett.* **1994**, 28, 41.

[41] Y.-G. Chen, J. Ren, *Catal. Lett.* **1994**, 29, 39-48.

[42] J. Zieliński, *J. Catal.* **1982**, 76, 157-163.

[43] F. Cavani, F. Trifirò, A. Vaccari, *Catal. Today*, **1991**, 11, 173-301.

[44] R. Rothbauer, F. Zigan, H. O'Daniel, *Zeitschrift für Kristallographie, Kristallgeometrie, Kristallphysik, Kristallchemie* **1967**, 125, 317.

[45] D. G. Evans, R. C. T. Slade, *Struct. Bonding* **2006**, 119, 1-87.

[46] J. Pérez-Ramírez, G. Mul, J. A. Moulijn, *Vib. Spectrosc.* **2001**, 27, 75–88.

[47] S. Velu, V. Ramaswamy, A. Ramani, B. M. Chandab, S. Sivasanker, *Chem. Commun.* **1997**, 21, 2107-2108.

[48] S. Velu, K. Suzuki, M. Okazaki, T. Osaki, S. Tomura, F. Ohashi, *Chem. Mater.* **1999**, 11, 2163-2172.

[49] M. Lakrairni, A. Legrouri, A. Barroug, A. de Roy, J.-P. Besse, *J. Chim. Phys. Phys.-Chim. Biol.* **1999**, 96,470-478.

[50] C. Forano, T. Hibino, F. Leroux, C. Taviot-Guého, in *Handbook of Clay Science*, ed. F. Bergaya, B. K. G. Theng, G. Lagaly, 1st Edition, Elsevier, Amsterdam, **2006**, 1021-1095.

[51] T. Hibino, Y. Yamashita, K. Kosuge, A. Tsunashima, *Clays Clay Miner.* **1995**, 43, 427-432.

[52] T. S. Stanimirova, I. Vergilov, G. Kirov, N. Petrova, *J. Mater. Sci.* **1999**, 34, 4153-4161.

[53] A. J. Marchi, C. R. Apesteguía, *Appl. Clay Sci.* **1998**, 13, 35–48.

[54] S. Miyata, *Clays Clay Miner.* **1980**, 28, 50-56.

[55] T. Shishido, M. Sukenobu, H. Morioka, R. Furukawa, H. Shirahase, K. Takehira, *Catal. Lett*. **2001**, 73, 21-26.

[56] K. Takehira, T. Shishido, P. Wang, T. Kosaka, K. Takaki, *Phys. Chem. Chem. Phys.* **2003**, 5, 3801-3810.

[57] K. Takehira, T. Shishido, P. Wang, T. Kosaka, K. Takaki, *J. Catal.* **2004**, 43-54.

[58] A. I. Tsyganok, T. Tsunoda, S. Hamakawa, K. Suzuki, K. Takehira, T. Hayakawa, *J. Catal.* **2003**, 213, 191-203.

[59] K. Takehira, T. Shishido, D. Shouro, K. Murakami, M. Honda, T. Kawabata, K. Takaki, *Appl. Catal., A* **2005**, 279, 41-51.

[60] K. Takehira, T. Kawabata, T. Shishido, K. Murakami, T. Ohi, D. Shoro, M. Honda, K. Takaki, *J. Catal.* **2005**, 231, 92-104.

[61] O. W. Perez-Lopez, A. Senger, N. R. Marcilio, M. A. Lansarin, *Appl. Catal., A* **2006**, 303, 234-244.

[62] Recommendations on Nomenclature for Contamination Phenomena in Precipitation from Aqueous Solutions, *Pure Appl. Chem.* **1974**, 37, 463-468.

[63] F. Schüth, M. Hesse, K. K. Unger, in *Handbook of Heterogeneous Catalysis*, ed. G. Ertl, H. Knoezinger, F. Schüth, J. Weitkamp, 2nd Edition, Wiley-VCH, Weinheim, **2008**, 100-119.

[64] C. Baltes, S. Vukojević, F. Schüth, *J. Catal*. **2008**, 258, 334-344.

[65] V. R. Choudhary, B. S. Uphade, A. A. Belhekar, *J. Catal*. **1996**, 163, 312-318.

[66] J. Guo, H. Lou, H. Zhao, D. Chai, X. Zheng, *Appl. Catal., A* **2004**, 273, 75-82.

[67] M. Behrens, I. Kasatkin, S. Kühl, G. Weinberg, *Chem. Mater.* **2010**, 22, 386-397.

[68] S. Kühl, A. Tarasov, S. Zander, I. Kasatkin, M. Behrens, *Chem. Eur. J.* **2014**, 20, 3782-3792.

[69] K. Mette, S. Kühl, H. Düdder, K. Kähler, A. Tarasov, M. Muhler, M. Behrens, *ChemCatChem* **2014**, 6, 100-104.

[70] H. Düdder, K. Kähler, B. Krause, K. Mette, S. Kühl, M. Behrens, V. Scherer, M. Muhler, *Catal. Sci. Technol*. **2014**, 4, 3317-3328.

[71] K. Mette, S. Kühl, A. Tarasov, H. Düdder, K. Kähler,M. Muhler, R. Schlögl, M. Behrens, *Catal. Today* **2015**, 242, 101-110.

2 Stable Performance of Ni Catalysts in the Dry Reforming of Methane at High Temperatures for the Efficient Conversion of CO_2 into Syngas

Katharina Mette, Stefanie Kühl, Hendrik Düdder, Kevin Kähler, Andrey Tarasov, Martin Muhler, Malte Behrens

Abstract

The catalytic performance of a Ni/$MgAlO_x$ catalyst was investigated in the high temperature CO_2 reforming of CH_4. The catalyst was developed using a Ni, Mg, Al hydrotalcite-like precursor obtained by co-precipitation. Despite the high Ni loading of 55 wt%, the synthesized Ni/$MgAlO_x$ catalyst possessed a thermally stable microstructure up to 900 °C with Ni nanoparticles of 9 nm. This stability is attributed to the embedding nature of the oxide matrix, and allows increasing the reaction temperature without losing active Ni surface area. To evaluate the effect of the reaction temperature on the reforming performance and the coking behavior, two different reaction temperatures (800 and 900 °C) were investigated. At both temperatures the prepared catalyst showed high rates of CH_4 consumption. The higher temperature promotes the stability of the catalyst performance due to mitigation of the carbon formation.

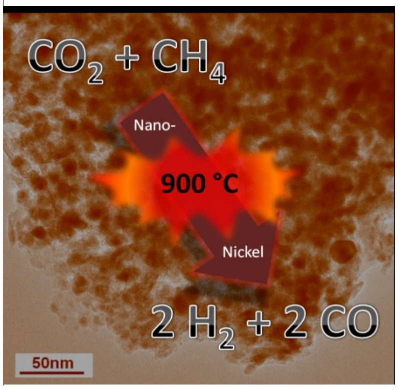

2.1 Introduction

The efficient conversion of CO_2 into various chemicals and fuels is a prospective building block for the more sustainable use of our global resources [1]. Among the various strategies that have been proposed for converting CO_2 into higher energy intermediates [2], processes that employ heterogeneous catalysis are of special interest, because they are scalable, based on a mature and flexible technology that has already been applied in the chemical industry, and can be integrated into existing value chains [3]. The dry reforming of methane (DRM) with carbon dioxide is an interesting method for converting these two greenhouse gases into CO/H_2 mixtures [Eq. (2.1)]. This reaction opens the door to utilizing anthropogenic CO_2, which is obtained from, for example, oxy-fuel-combustion processes, in the well-established downstream chemistry of syngas to afford MeOH and other base chemicals or fuels through Fischer–Tropsch synthesis.

$$CO_2 + CH_4 \rightarrow 2\ CO + 2\ H_2 \qquad \Delta H_{298} = 247\ kJ\ mol^{-1} \qquad (2.1)$$

The highly endothermic DRM reaction has long been studied as a potential alternative for the steam reforming of methane and several comprehensive reviews have been published on this topic [4,5,6]. It is well-known that Ru, Rh, and Pt catalysts are very active in this reaction. Active base metals—and Ni in particular—suffer from fast deactivation by coking [7,8]. However, from an economic point of view, Ni-based catalysts are more suitable for commercial applications than noble-metal ones. Thus, a current challenge is to find a noble-metal-free catalyst that is resistant towards coking [9]. Promising approaches in the literature include the poisoning of coke-forming sites by sulfur [10], variation of the support [11], in particular through the application of Lewis-basic materials [12], the addition of alkaline or alkaline-earth oxides as promoters [13,14], and the incorporation of Ni into a perovskite framework [15]. It has been shown that the deposition of carbon over Ni at 700 °C and over Rh at 750 °C originates from the exothermic Boudouard reaction [Eq. (2.2)] and not primarily from methane decomposition [Eq. (2.3)] [16,17].

$$2\ CO \leftrightarrow CO_2 + C \qquad \Delta H_{298} = -172\ kJ\ mol^{-1} \qquad (2.2)$$

$$CH_4 \rightarrow C + 2\ H_2 \qquad \Delta H_{298} = 75\ kJ\ mol^{-1} \qquad (2.3)$$

Thus, the process temperature is an important parameter in the DRM reaction [4]. Considering the thermodynamics of the desired endothermic DRM and of the undesired exothermic Boudouard reaction, a promising way of suppressing coking would be to perform the DRM reaction at high temperatures [18]. Typically, 750 °C is an upper limit in many literature reports. In addition, the thermodynamic yields of CO and H_2 would increase at higher temperatures. Following this concept, the primary challenge in making the Ni particles kinetically more resistant to coking involves making a large Ni surface area thermally stable against sintering at more elevated temperatures. Herein, we report the synthesis, characterization and catalytic performance of a Ni-rich bulk catalyst that shows sufficient thermal stability of its microstructure.

Our synthetic approach to stabilizing Ni nanoparticles at high temperatures was to incorporate them into a stable oxide matrix, a concept that has previously been applied to Ni-containing perovskites [15] and spinels [19]. We attempted to achieve strong interfacial interactions between the metal and the oxide by a stabilizing partial embedding of the Ni particles through the formation of both catalyst components from a single phase precursor with a mixed cationic lattice and decomposable anions. This concept was previously applied to Cu-based catalysts for MeOH synthesis, in which Cu,Zn,Al hydrotalcites were developed as promising catalyst-precursor materials [20]. The resulting catalysts are characterized by a homogeneous metal distribution and very small Cu particles that were embedded and, therefore, stabilized in an amorphous $ZnAl_2O_4$ matrix.

2.2 Results and Discussion

Following this concept, we chose a hydrotalcite-like (htl) precursor with the nominal composition $Ni_xMg_{0.67-x}Al_{0.33}(OH)_2\text{-}(CO_3)_{0.17} \cdot mH_2O$ (x=0.5). This precursor compound could be easily prepared in its phase-pure form by pH-controlled co-precipitation (see the Supporting Information, Figure S2.1). The application of htl precursors for the preparation of Ni catalysts has been studied before by several groups for the steam and dry reforming of methane. For instance, Takehira and co-workers [21,22,23,24,25,26] and Perez-Lopez et al. [27] presented different synthetic approaches to htl-derived $Ni/MgO/Al_2O_3$ catalysts, with Ni content ranging from 22 to 55 mol%, and investigated these materials in the DRM. Moderate coking levels between 500 and 700 °C were reported for a Ni/Mg/Al molar composition of 55:11:33. The high Ni content of 50 mol% (metal base) in our precursor corresponded to a Ni loading of 55 wt% in the final catalyst. This rather high value was chosen to exploit the advantage of higher loadings of cheap and abundant base-metal catalysts. The 1:2 ratio of Mg to Al was expected to lead to spinel formation, $MgAl_2O_4$, which is a sintering-stable ceramic compound. Indeed, beneficial effects on the coking behavior of Ni catalysts have been reported on alumina, magnesia, and spinel supports [28]. First, we will focus on the synthesis and thermal stability of the htl-derived 55 wt% $Ni/MgAl_2O_4$ catalyst and then consider the catalytic properties in the DRM at high temperatures and the characterization of the spent samples will be reported.

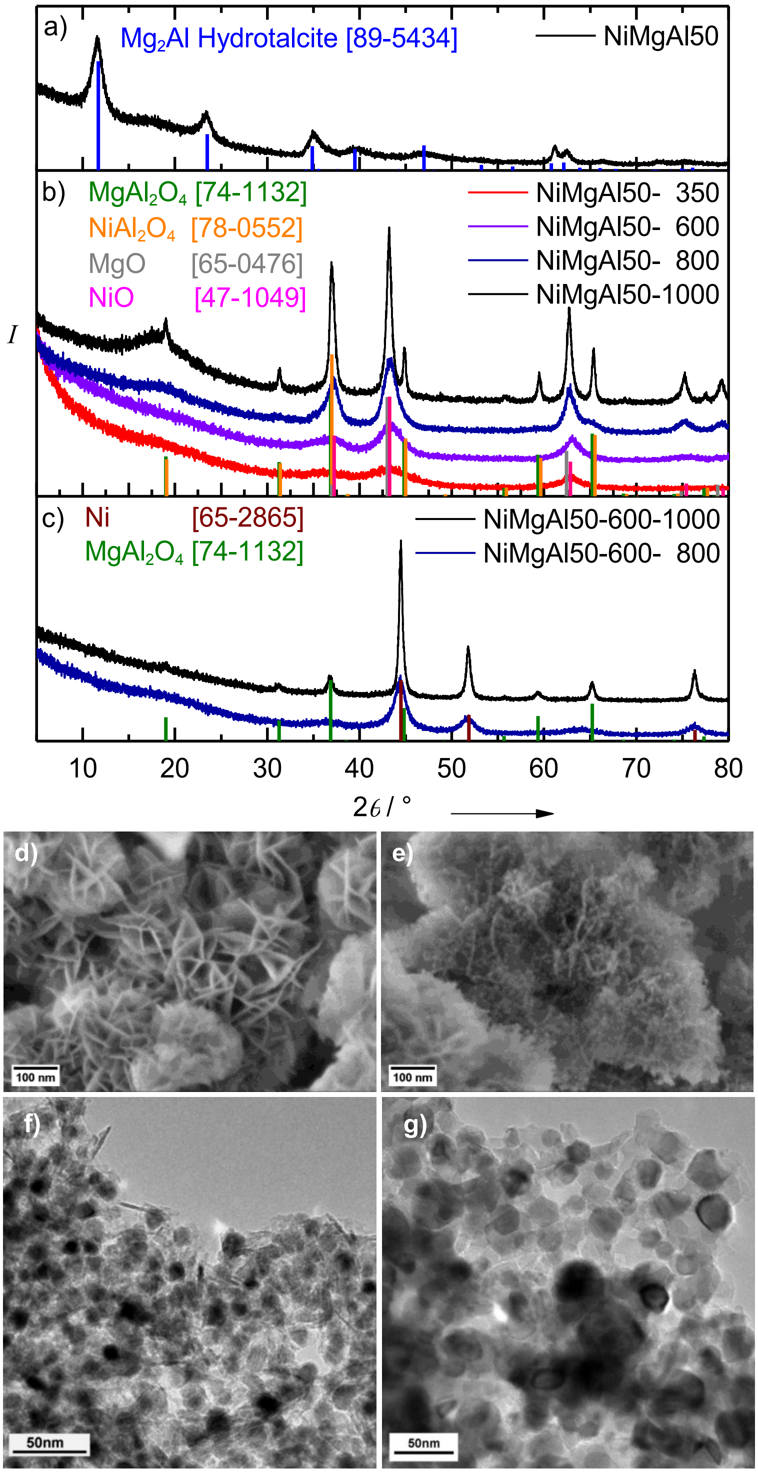

Figure 2.1 XRD patterns of the htl precursor (a), the calcination products obtained at different temperatures (b), the sample calcined at 600 °C after reduction at 800 and 1000 °C (c), SEM images of the precursor material (d) and the catalyst after reduction at 800 °C (e) and TEM micrographs of the fresh Ni/$MgAl_2O_4$ catalyst after reduction at 800 (f) and 1000 °C (g).

XRD analysis of the co-precipitated precursor confirmed the htl structure of the precursor and did not indicate the presence of any other crystalline phases (Figure 2.1a). SEM analysis revealed the typical platelet-like morphology of htl compounds, with a lateral size of up to approximately 200 nm and a thickness in the low-nm range (Figure 2.1d). The BET surface area of the precursor material was relatively high (131 m^2 g^{-1}). Upon calcination, the htl structure decomposed and the precursor underwent a weight loss of 38% (up to 1000 °C), which was already close to completion at 600 °C (for the TGA curve, see the Supporting Information, Figure S2.2). The XRD patterns of samples that were calcined at different temperatures are shown in Figure 1b. At 350 and 600 °C, only broad modulations of the background were observed at the peak positions of a rock-salt-type phase (NiO or MgO). At 800 °C, crystallization had progressed further and the first indications of a crystalline spinel phase were detected. After calcination at 1000 °C, the XRD pattern showed a mixture of rock-salt- and spinel-type phases, as expected for the decomposition of a htl compound [29,30]. Owing to the similar diffraction patterns of MgO and NiO and of $MgAl_2O_4$ and $NiAl_2O_4$, as well as the possible formation of solid solutions, no detailed phase identification could be performed based on the XRD data, in particular for the poorly crystalline materials that were obtained at lower calcination temperatures. However, after mild calcination at 600 °C, no indication of the segregation of individual species was found by SEM or by local EDX analyses at different locations (see the Supporting Information, Figure S2.3 and Table S2.1). Thus, we conclude that the calcination product that was obtained at 600 °C is an amorphous, fully dehydrated, and carbonate-free mixed Ni/Mg/Al oxide, the homogenous distribution of the metal species of which had been largely conserved during the decomposition of the htl precursor. The surface area has increased to 213 m^2 g^{-1}, owing to the weight loss and to shrinkage of the platelets.

Table 2.1 Physical properties of Ni particles of NiMgAl50-600 after reduction at different temperatures.

T_{red} / °C	Domain size / nm[a]	Particle size / nm[b]	Particle size range / nm[b]	Ni surface area / m^2/g_{cat}[c]	Ni surface area / m^2/g_{Ni}[c]	Dispersion / %[d]	Interface ratio / %[e]
800	4.30 ± 0.20	10.4 ± 1.3	2 - 21	22	46	6.0	41.3
900	7.35 ± 0.11	8.9 ± 1.6	2 - 21	19	40	5.3	58.6
1000	14.10 ± 0.20	19.4 ± 2.2	7 - 44	6	12	1.6	67.8

[a] Volume-weighted column length based on the integral peak breadths fitted using TOPAS [31]; [b] determined by TEM; [c] determined by H_2-pulse chemisorption; [d] calculated from the H_2-pulse-chemisorption measurements; [e] calculated from the Ni surface area and TEM particle size.

After reduction of the calcined material in hydrogen at 800 °C (for the TPR curve, see the Supporting Information, Figure S2.4), SEM analysis revealed that the platelet-like morphology of the htl precursor was still present, thus indicating strong resistivity of the material against sintering at high temperatures (Figure 2.1e). In addition, small bright spheres that were homogeneously distributed over the platelets were observed in the micrograph, thus indicating that, upon reduction, nanoscopic segregation of the components had taken place.

Indeed, XRD analysis (Figure 2.1c) clearly confirmed the presence of metallic Ni after calcination at 600 °C and subsequent reduction at 800 °C, with a domain size of 4 nm, according to a peak-width analysis. The oxidic component was still only poorly crystalline and no sharp peaks of the spinel could be detected. TEM analysis of individual platelets in the reduced material revealed an average particle size of Ni of about 10 nm (Figure 2.1f and the Supporting Information, Figure S2.5a). The discrepancy between the XRD- and TEM-derived size data is thought to be caused by the polycrystalline and defect-rich nature of the embedded particles [32]. The Ni surface area was determined by hydrogen-pulse chemisorption (see the Supporting Information, Figure S2.6) to be 22 m^2 $gcat^{-1}$ at a BET surface area of 226 m^2 g^{-1} after reduction. Interestingly, increasing the reduction temperature to 900 °C did not significantly influence the Ni particle size (see the Supporting Information, Figure S2.7). This result was even more important because that temperature was far above the Tammann temperature of Nickel ($T_{\text{Tammann, Ni}}$= 581 °C [33]), thus confirming the high thermal stability of this composite material. However, the domain size increased to 7 nm, in good agreement with the TEM analysis of about 9 nm (Table 2.1 and the Supporting Information, Figure S2.5b), thus suggesting that the effect of temperature was an annealing of the structural defects rather than sintering. Only treatment at 1000 °C led to pronounced sintering of the Ni particles to an average Ni particle size of about 19 nm, according to the TEM analysis (Figure 2.1g), and a domain size of about 14 nm, according to the XRD analysis. This process goes hand in hand with the onset of crystallization of the $MgAl_2O_4$ spinel in the oxide matrix (Figure 2.1c). Accordingly, the specific Ni surface area only decreased slightly to 88% by increasing the reduction temperature from 800 to 900 °C and broke down to only 27% at 1000 °C.

In summary, the characterization data show that the synthesis from the htl precursor yields a Ni catalyst that, despite its high Ni loading of 55 wt%, possesses a thermally stable microstructure up to 900 °C. This stability is probably attributed to the embedding nature of the still-amorphous oxide matrix that separates the Ni nanoparticles from each other and, therefore, protects them from sintering, thereby resulting in an interface-to-surface ratio of the particles of 41% (for detailed information, see the Supporting Information); even after thermal treatment up to 900 °C, the dispersion of the Ni particles (5–6 %, Table 2.1), as well as the total specific surface area and the exposed specific Ni surface area, was surprisingly high. Thus, these materials are promising catalysts that have the potential to withstand an increase in the reaction temperature of the DRM to study the suppression of coking.

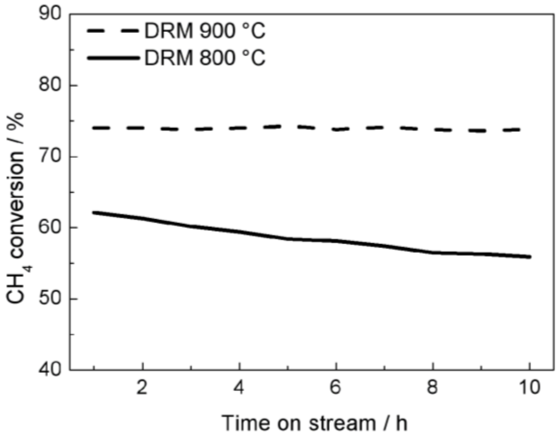

Figure 2.2 CH_4 conversion as a function of time on stream in the DRM at 800 °C and 900 °C using the Ni/MgAlOx catalyst after reduction up to 800 °C.

The catalytic activity and stability of the ex-htl catalysts were investigated in a fixed-bed reactor under isothermal DRM conditions. After a reductive pretreatment up to 800 °C, the DRM reaction was performed at 800 °C and 900 °C. At 800 °C, slight deactivation was observed, whereas, at 900 °C, a higher degree of stable conversion was detected (Figure 2.2). Even in long-term experiments, the catalyst showed a remarkable stable activity at 900 °C, thereby still achieving 94% of the initial conversion of CH_4 after 100 h (see the Supporting Information, Figure S2.8). This result was attributed to the stabilizing effect of the oxide matrix, which only allowed minor sintering of the active Ni nanoparticles, as confirmed by TEM and XRD. The integral rates of methane conversion, as determined after 60 min time on stream, were 3.5×10^{-3} mol s^{-1} g_{cat}^{-1} at 800 °C and 4.2×10^{-3} mol s^{-1} g_{cat}^{-1} at 900 °C. These values are, to the best of our knowledge, the highest reported rates for DRM catalysts in the literature.

During a subsequent temperature-programmed oxidation (TPO) experiment, the formation of CO_2 was observed, owing to the presence of carbonaceous deposits. In the TPO profile after DRM at 800 °C, two signals at 580 °C and 670 °C were identified, which afforded an overall amount of 117 mmol g_{cat}^{-1} of formed CO_2. In the DRM at 900 °C, the degree of carbon deposition decreased to 54 mmol g_{cat}^{-1}, including a third carbon species that was detected at 780 °C (Figure 2.3). Once the carbon deposits had been completely removed by TPO, the initial activity for the DRM was recovered (see the Supporting Information, Figure S2.9). Thus, the observed deactivation during the DRM at 800 °C was predominantly caused by the formation of carbon deposits and not by sintering. In agreement with the TPO results, Raman spectra of spent samples after DRM revealed a lower graphitic content at 800 °C (see the Supporting Information, Figure S2.12).

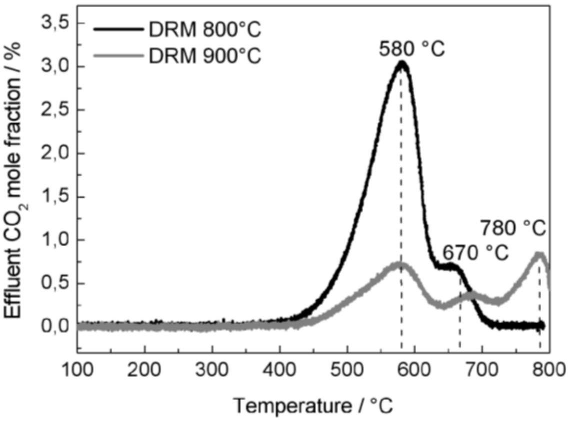

Figure 2.3 TPO profiles after DRM at 800 °C and 900 °C (F = 40 Nml min^{-1} 4.5 % O_2/Ar, β = 5 K min^{-1}, T_{max} = 800 °C) (Dry Reforming conditions: T_{Oven} = 800 °C or 900 °C, F_{total} = 240 Nml min^{-1} (32 % CH_4, 40 % CO_2, 28 % Ar (CO_2/CH_4 = 1.25))).

These results indicate that the carbon-formation mechanism is influenced by the reaction temperature. At 800 °C, a significant amount of carbon nanotubes (CNTs) is formed, thereby giving rise to the TPO peak at 580 °C, whereas, at 900 °C, fewer CNTs and a more-stable type of carbon are formed, presumably by pyrolysis of CH_4 [Eq. (2.3)]. The presence of different amounts and types of carbon in the spent samples was also observed in the TEM analysis of the catalysts after 10 h in an analogous test without a final TPO step. After reaction at 800 °C, in addition to a slight sintering of the Ni particles (see the Supporting Information, Figure S2.10 and Table S2.2), at least three different carbon species were formed, that is, carbon nanotubes (Figure 2.4a), graphitic layers (Figure 2.4c), and carbon onions with the inclusion of Ni particles (Figure 2.4b). TEM investigation of the catalyst after reaction at 900 °C (see the Supporting Information, Figure S2.11) confirmed the TPO result, because much less carbon was detected. Furthermore, the CNTs were still present but to a much lower extent and they were less well-connected to the catalyst material.

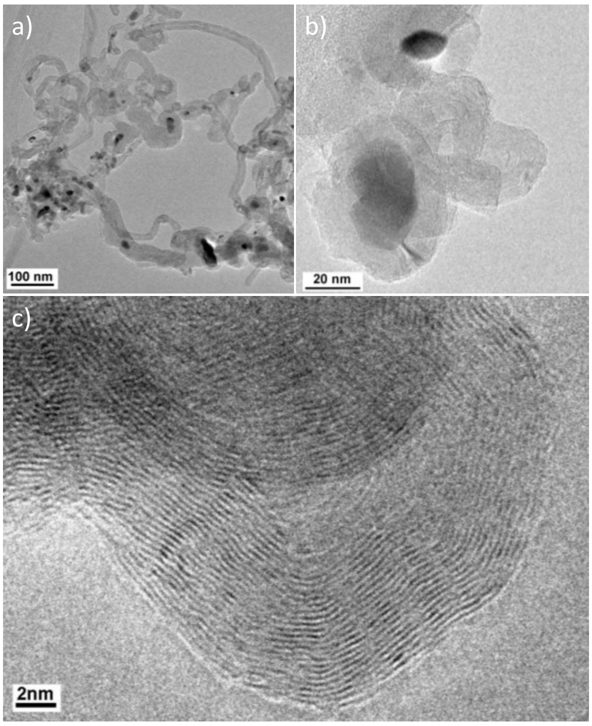

Figure 2.4 TEM micrographs of the spent sample run in DRM for 10 h at a reaction temperature of 800°C: a) CNT´s (containing Ni particles), b) isolated Ni particles in carbon onions and c) layers of graphitic carbon.

2.3 Conclusion

In summary, we have shown that mitigation of the coking problem of noble-metal-free Ni catalysts for the DRM is possible by elevating the operating temperature towards 900 °C. This favorable operating window can only be exploited if nanostructured catalysts with sufficient thermal stability are available to survive these harsh conditions. We have reported the synthesis, characterization, and catalytic testing of a highly active and stable Ni/MgAlO$_x$ catalyst that was characterized by small Ni particles, which were partially embedded in an oxide matrix with a high specific Ni and total BET surface area. Despite the high Ni loading of 55 wt%, this catalyst only showed minor sintering at 900 °C and performed stably in the DRM over 100 h with an outstanding activity. Compared to the lower reaction temperatures, the major problem of coking was (to a large extent) overcome on this stable Ni catalyst by increasing the reaction temperature to 900 °C, which led to the formation of a less-fibrous carbon material.

2.4 References

[1] C. Song, *Catal. Today* **2006**, 115, 2–32.

[2] W. Wang, S. Wang, X. Ma, J. Gong, *Chem. Soc. Rev.* **2011**, 40, 3703–3727.

[3] R. Schlögl, *ChemSusChem* **2010**, 3, 209–222.

[4] M. C. J. Bradford, M. A. Vannice, *Catal. Rev. Sci. Eng.* **1999**, 41, 1–42.

[5] Y. H. Hu, E. Ruckenstein, *Adv. Catal.* **2004**, 48, 297–345.

[6] M.-S. Fan, A. Z. Abdullah, S. Bhatia, *ChemCatChem* **2009**, 1, 192–208.

[7] A. T. Ashcroft, A. K. Cheetham, M. L. H. Green, P. D. F. Vernon, *Nature* **1991**, 352, 225–226.

[8] S. Wang, G. Q. Lu, G. J. Millar, *Energy Fuels* **1996**, 10, 896–904.

[9] C.-j. Liu, J. Ye, J. Jiang, Y. Pan, *ChemCatChem* **2011**, 3, 529–541.

[10] J. R. Rostrup-Nielsen, *J. Catal.* **1984**, 85, 31–43.

[11] M. C. J. Bradford, M. A. Vannice, *Appl. Catal., A* **1996**, 142, 73–96.

[12] T. Horiuchi, K. Sakuma, T. Fukui, Y. Kubo, T. Osaki, T. Mori, *Appl. Catal., A* **1996**, 144, 111–120.

[13] Z. L. Zhang, X. E. Verykios, *Catal. Today* **1994**, 21, 589–595.

[14] S.-B. Tang, F.-L. Qiu, S.-J. Lu, *Catal. Today* **1995**, 24, 253–255.

[15] V. R. Choudhary, B. S. Uphade, A. A. Belhekar, *J. Catal.* **1996**, 163, 312–318.

[16] H. M. Swaan, V. C. H. Kroll, G. A. Martin, C. Mirodatos, *Catal. Today* **1994**, 21, 571–578.

[17] V. A. Tsipouriari, A. M. Efstathiou, Z. L. Zhang, X. E. Verykios, *Catal. Today* **1994**, 21, 579–587.

[18] J.-W. Snoeck, G. F. Froment, M. Fowles, *Ind. Eng. Chem. Res.* **2002**, 41, 4252–4265.

[19] J. Guo, H. Lou, H. Zhao, D. Chai, X. Zheng, *Appl. Catal., A* **2004**, 273, 75–82.

[20] a) M. Behrens, I. Kasatkin, S. Kühl, G. Weinberg, *Chem. Mater.* **2010**, 22, 386–397; b) S. Kühl, M. Friedrich, M. Armbrüster, M. Behrens, *J. Mater. Chem.* **2012**, 22, 9632–9638.

[21] T. Shishido, M. Sukenobu, H. Morioka, R. Furukawa, H. Shirahase, K. Takehira, *Catal. Lett.* **2001**, 73, 21–26.

[22] K. Takehira, T. Shishido, P. Wang, T. Kosaka, K. Takaki, Phys. *Chem. Chem. Phys.* **2003**, 5, 3801–3810.

[23] K. Takehira, T. Shishido, P. Wang, T. Kosaka, K. Takaki, *J. Catal.* **2004**, 221, 43–54.

[24] A. I. Tsyganok, T. Tsunoda, S. Hamakawa, K. Suzuki, K. Takehira, T. Hayakawa, *J. Catal.* **2003**, 213, 191–203.

[25] K. Takehira, T. Shishido, D. Shouro, K. Murakami, M. Honda, T. Kawabata, K. Takaki, *Appl. Catal., A* **2005**, 279, 41–51.

[26] K. Takehira, T. Kawabata, T. Shishido, K. Murakami, T. Ohi, D. Shoro, M. Honda, K. Takaki, *J. Catal.* **2005**, 231, 92–104.

[27] O. W. Perez-Lopez, A. Senger, N. R. Marcilio, M. A. Lansarin, *Appl. Catal., A* **2006**, 303, 234–244.

[28] Y.-G. Chen, J. Ren, *Catal. Lett.* **1994**, 29, 39–48.

[29] F. Cavani, F. Trifirò, A. Vaccari, *Catal. Today* **1991**, 11, 173–301.

[30] F. Zhang, X. Xiang, F. Li, X. Duan, *Catal. Surv. Asia* **2008**, 12, 253–265.

[31] TOPAS version 3, copyright **1999**, 2000 Bruker AXS2.

[32] J. Sehested, A. Carlsson, T. V. W. Janssens, P. L. Hansen, A. K. Datye, *J. Catal.* **2001**, 197, 200–209.

[33] J. Rostrup-Nielsen, L. J. Christiansen in *Concepts in Syngas Manufacture*, Vol. 10 (Ed.: G. J. Hutchings), Imperial College Press, London, **2011**, pp. 219–227.

2.5 Experimental Section

The catalysts were prepared by constant pH-controlled co-precipitation in an automated laboratory reactor (Mettler-Toledo Labmax) at 50 °C from a 0.6 M aqueous solution of NaOH, a 0.09 M aqueous solution of Na_2CO_3, and a 0.4 M aqueous solution of the metal nitrate at pH 8.5. The obtained precursor was calcined in air at 600 °C for 3 h, thereby yielding almost-amorphous mixed oxides.

For the catalytic experiments, the ex-htl Ni/MgAlOx catalyst (10 mg, sieve fraction: 250–355 mm) that had been calcined at 600 °C prior to the experiment was used in a fixed-bed tubular quartz reactor. The sample was diluted in SiC (490 mg). For the pretreatment, the catalyst was reduced in 4% H_2/Ar (20 Nml min^{-1}). The DRM was performed at 800 or 900 °C in 40% CO_2 /32% CH_4/Ar (240 Nml min^{-1}) for 10 or 100 h, respectively. Subsequent TPO experiments were performed in 4.5% O_2/Ar (40 Nml min^{-1}). Analysis of the gaseous products was performed on a multi-channel gas analyzer (MLT 4, Emerson) with a paramagnetic oxygen detector (Magnos 16, Hartmann & Braun) for the transient experiments and a calibrated GC for the activity tests (Shimadzu GC-14B).

2.6 Supporting information

2.6.1 Synthesis

A hydrotalcite-like (htl) compound of the general composition $(Ni,Mg)_{1-x}Al_x(OH)_2(CO_3)_{x/2} \cdot 2\ H_2O$ was prepared with a Ni:Mg:Al molar ratio of 50:17:33 using the co-precipitation technique. A protocol of the precipitation process at 50 °C is seen in Figure S2.1. The nitrate solution and the precipitating agent were added simultaneously, to keep the pH constant at 8.5. After subsequent ageing and drying, the sample was calcined, reduced, and stored in air.

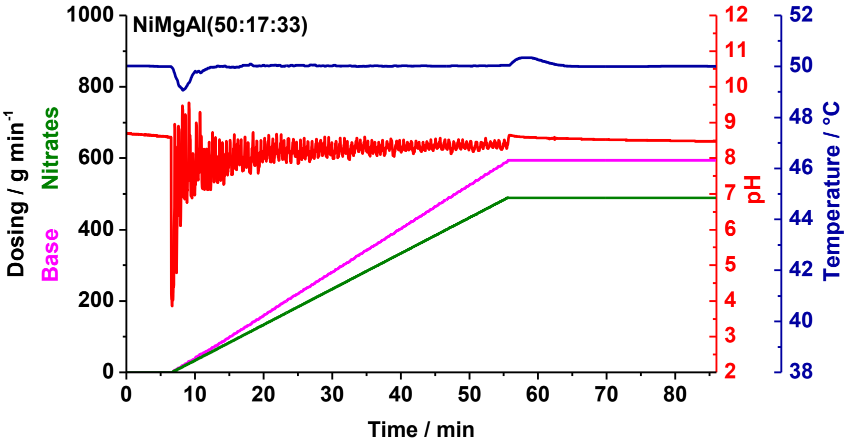

Figure S2.1 Protocol of co-precipitation (LabMax).

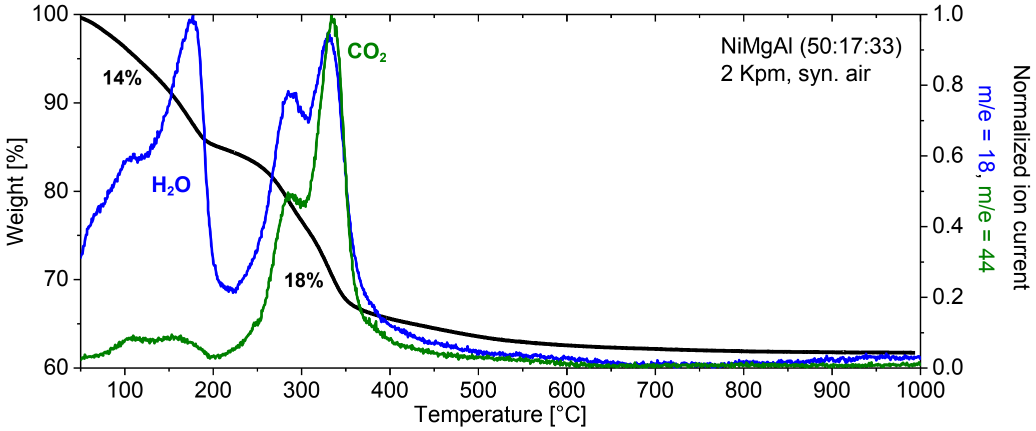

Figure S2.2 TG curve (black) and MS traces for H_2O (blue) and CO_2 (green) of the NiMgAl50 catalyst precursor.

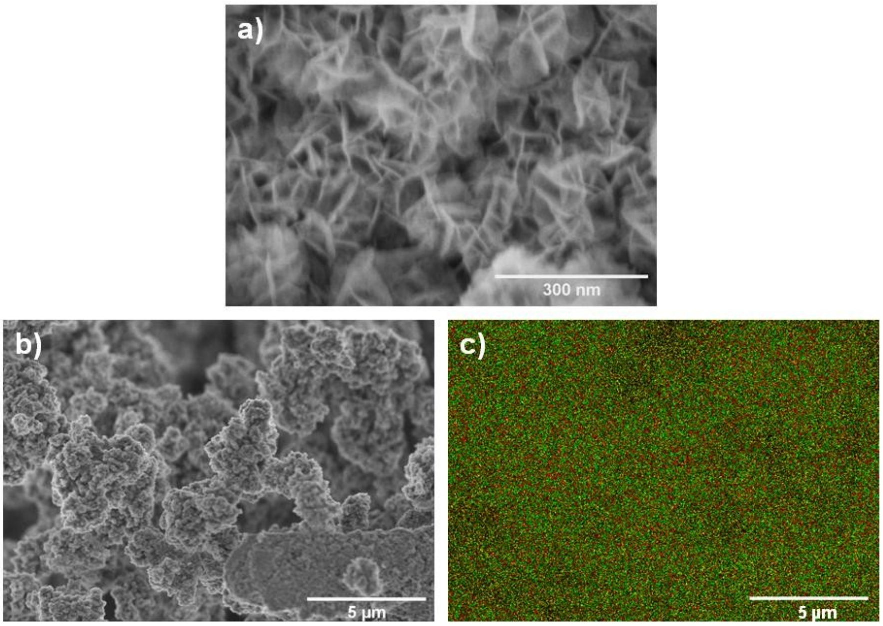

Figure S2.3 SEM + element mapping of NiMgAl50-600.

Table S2.1 EDX data of NiMgAl50-600 (spray dried!).

Element	Nom. mol%	Nom. wt.-%	EDX mol%	EDX wt.-%
Ni	50	69.2	46.2 ± 2.5	65.9 ± 2.2
Mg	17	9.8	17.7 ± 1.2	10.5 ± 0.9
Al	33	21.0	36.1 ± 1.6	23.7 ± 1.5

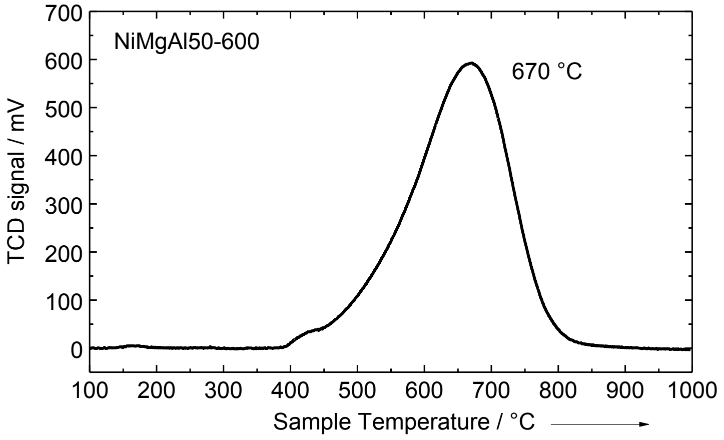

Figure S2.4 TPR of NiMgAl50-600 in 5 % H_2/Ar (80 Nml min^{-1}), 6 K min^{-1}.

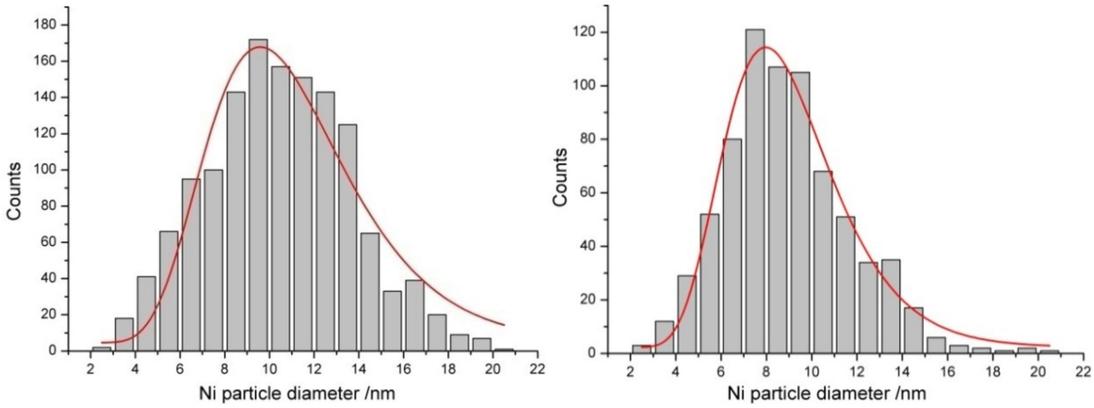

Figure S2.5 Ni particle size distribution determined from TEM images after reduction at (a) 800°C and (b) 900°C.

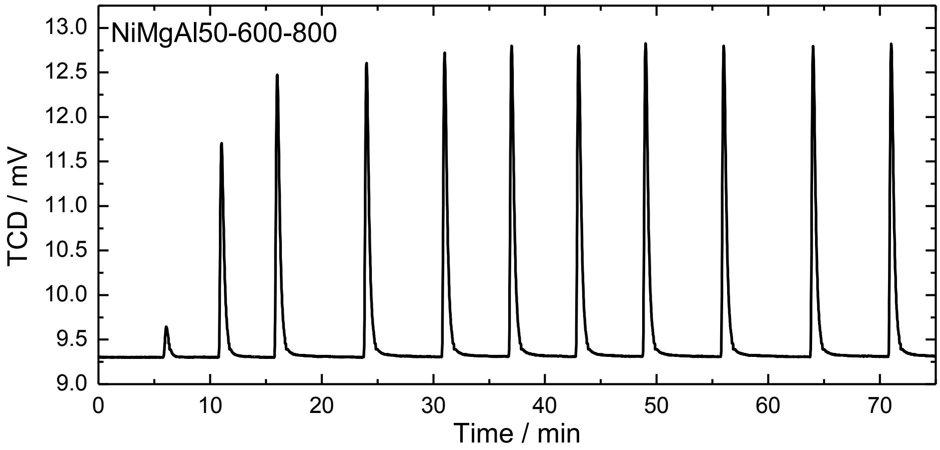

Figure S2.6 H_2 pulse chemisorption profile of NiMgAl50-600-800 at 50 °C.

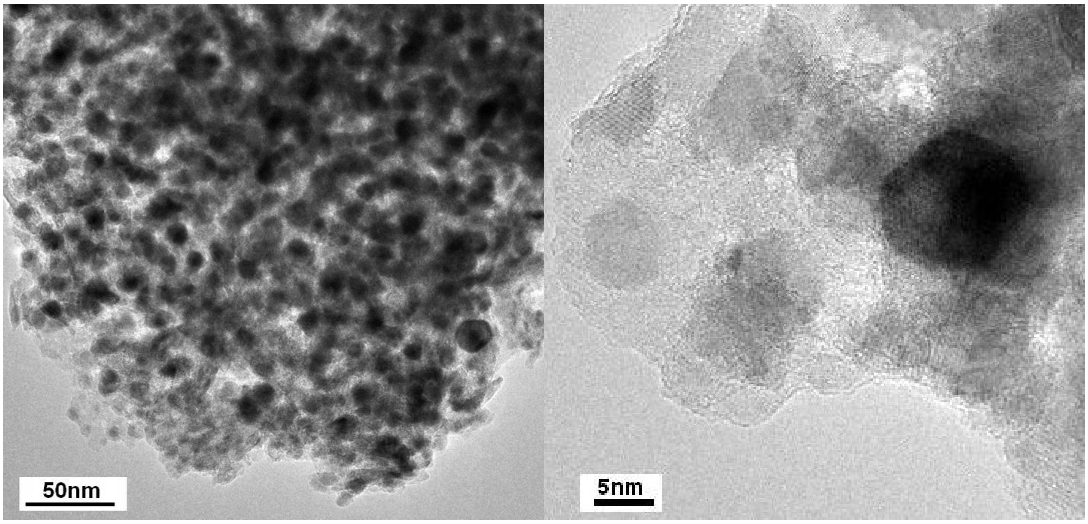

Figure S2.7 TEM images after reduction at 900 °C.

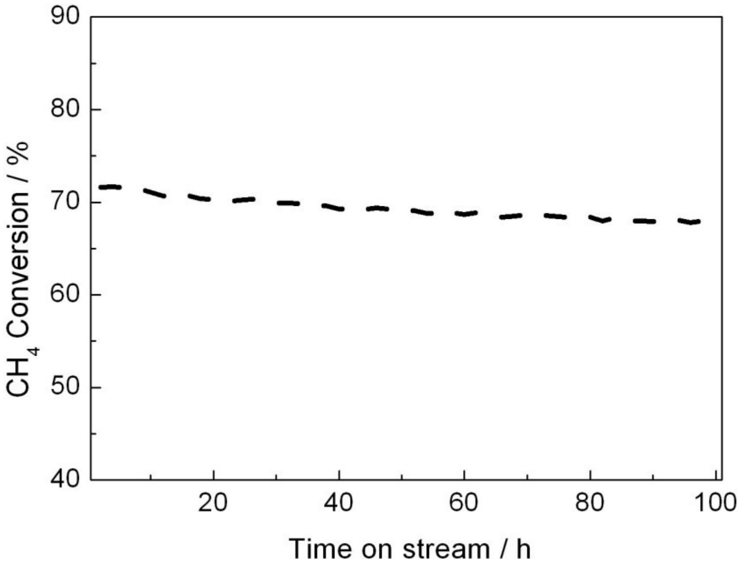

Figure S2.8 CH_4 conversion as a function of time on stream over 100 h in the DRM at 900 °C using the Ni/MgAlOx catalyst after reduction at 800 °C.

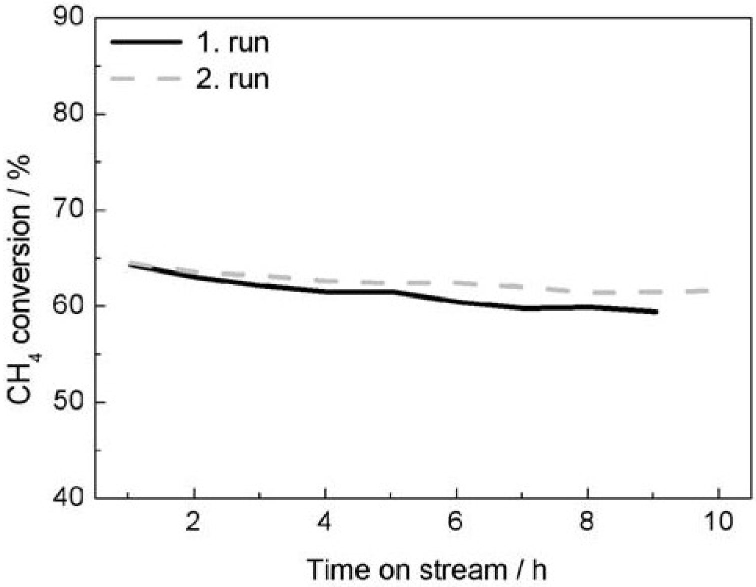

Figure S2.9 CH_4 conversion as a function of time on stream in the DRM at 800 °C using the Ni/MgAlOx catalyst after reduction at 800 °C. 1. run: initial DRM, 2. run: DRM after subsequent TPO - TPR cycle.

Table S2.2 Ni particle size distribution, activity and carbon formation of NiMgAl50-600-800 after DRM at different temperatures.

T_{red} / °C	T_{DRM} / °C	Particle size range / nm[a]	CH_4 / mmol $s^{-1} \cdot g_{cat}^{-1}$[b]	CO_2 / mmol g_{cat}^{-1}[c]
800	800	4 - 32	3.5	117
800	900	5 - 34	4.2	54

[a] determined by TEM [b] methane conversion after 1 h TOS [c] determined by TPO after 10 h TOS

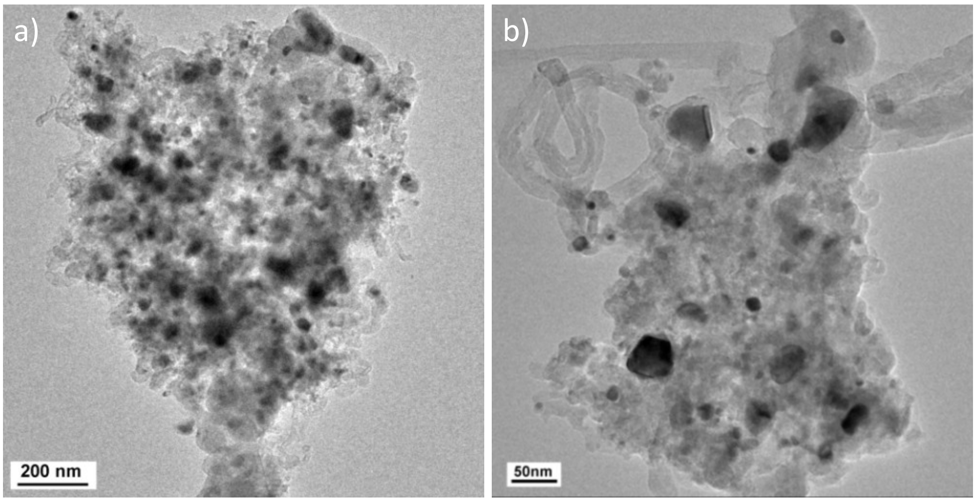

Figure S2.10 TEM images after DRM at 800 °C (pre-reduced at 800 °C): agglomerate with different regions, catalyst morphology partially preserved, Ni particles partially sintered.

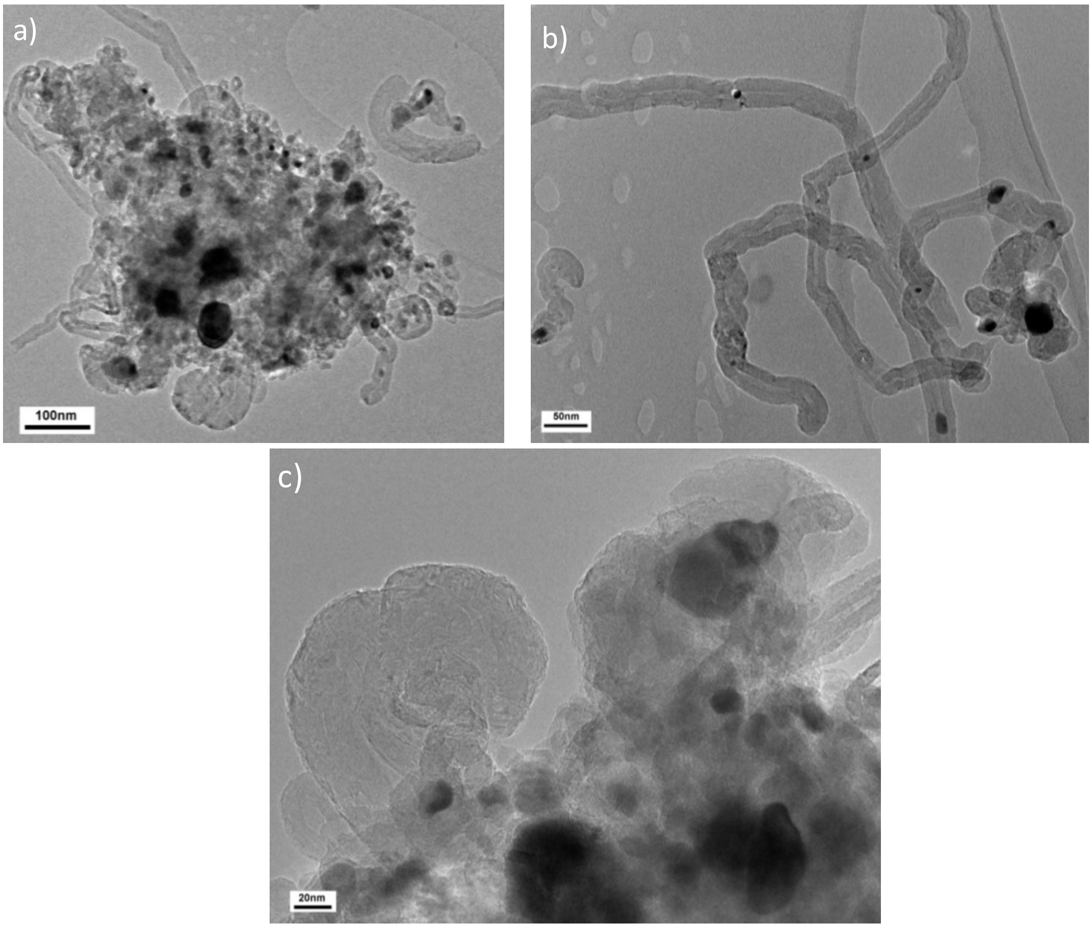

Figure S2.11 TEM images after DRM at 900 °C (pre-reduced at 800 °C): (a) agglomerate with different regions, catalyst morphology partially preserved and Ni particles partially sintered, (b) CNT´s present but less dominant and mostly apart from agglomerates (less connected), (c) graphitic carbon at the edge of agglomerates, partially with isolated Ni particles.

2.6.2 Raman spectra of spent samples

The spectrum of the spent NiMgAl50 catalyst (reduction at 1000 °C, DRM at 900 °C) exhibits 5 first order bands, the G and the D1 to D4 bands (Figure S2.12). The fitting was performed according to Sadezky et al. [S1]. In addition to the higher content of graphitic carbon after DRM at 900 °C the stronger D3 band also indicates a higher fraction of amorphous carbon.

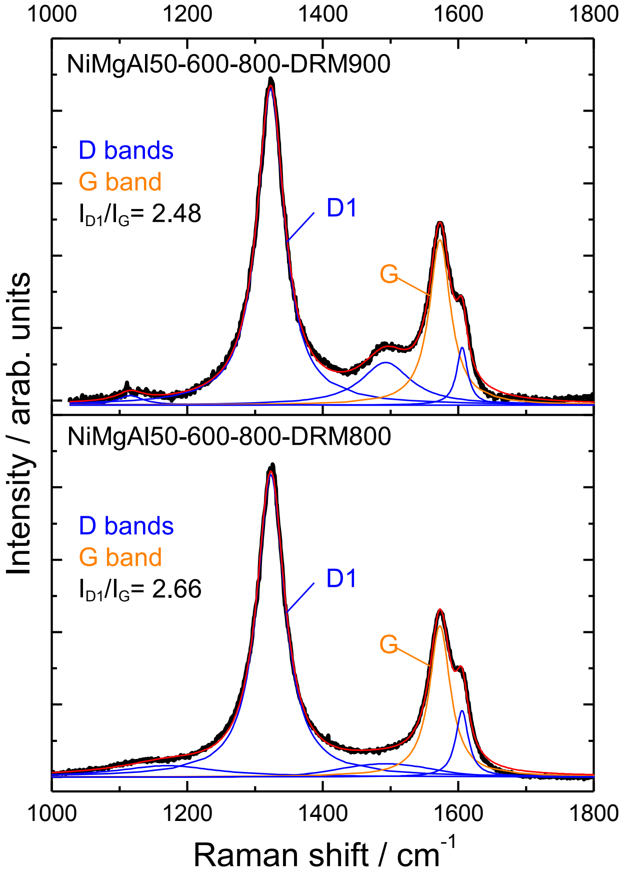

Figure S2.12 Fitted Raman spectra (633 nm) of NiMgAl50-600-800 samples after DRM at 800 and 900 °C.

2.6.3 Titration Experiments

Titration experiments have been performed in order to find a suitable pH value for the precipitation. Therefore nickel, magnesium and aluminum nitrates as well as the mixed nitrates were titrated with a mixture of NaOH and Na_2CO_3 as precipitating agent at 25 and 50 °C (Figure S2.13). As the temperature was increased from 25 to 50 °C, the pH scale was shifted to lower values. A small amount of conc. Nitric acid (65 wt%) was added to lower the pH to < 2. Thus, the neutralization curve of HNO_3 at pH 7 appears in all titration curves.

Nickel is completely solidified at pH > 8 (Figure S2.13-A). Magnesium is completely solidified at pH > 5 (Figure S2.13-B). Aluminum is completely solidified at pH > 5 (Figure S2.13-C). It also shows the typical olation in the pH range 3.0-4.5. A pronounced step-like shape of the titration curve is not observed for the Ni,Mg,Al nitrate system (Figure S2.13-D). However, the co-precipitation pH of Ni,Mg and Al form a LDH structure by NaOH and Na_2CO_3 is necessary to be above 8.0.

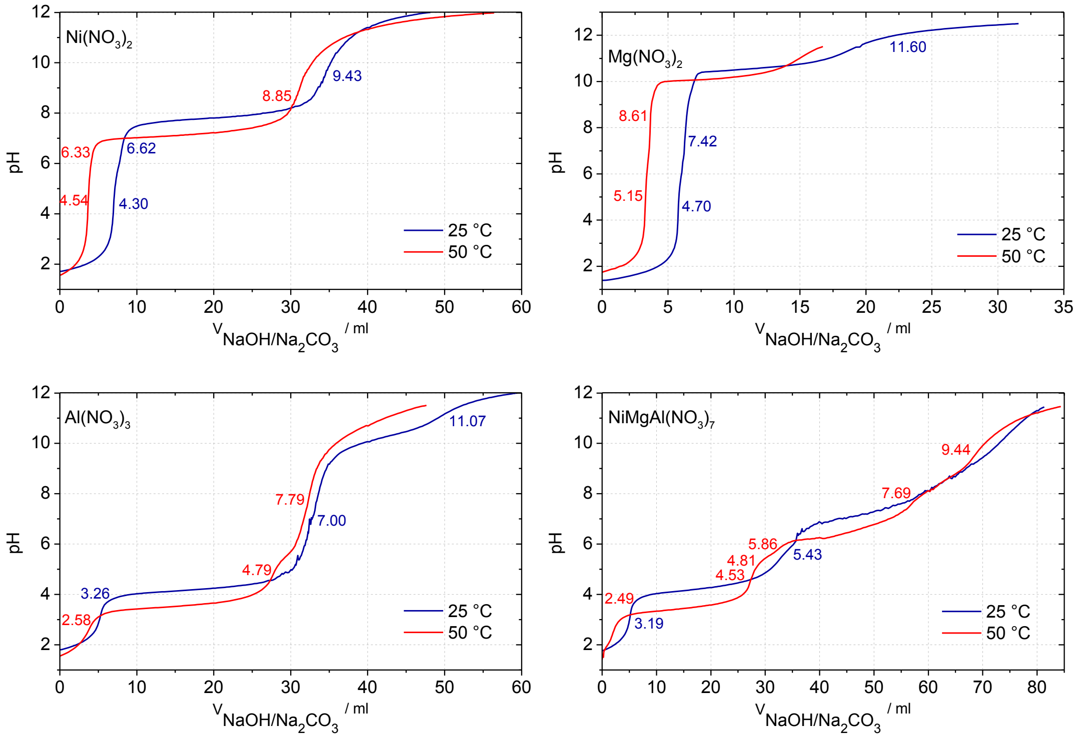

Figure S2.13 Titration curves of (A) nickel nitrates, (B) magnesium nitrate, (C) aluminum nitrate and (D) nickel, magnesium, aluminum nitrate at 25 °C (blue) and 50 °C (red).

2.6.4 Experimental Section

An automated laboratory titrator (Mettler Toledo Titrator DL77) was used for the titration experiments to investigate the precipitation pH of this system. The precipitating agent was an aqueous mixed solution of NaOH (0.150 M) and Na_2CO_3 (0.023 M). Metal nitrate solutions of 0.050 M $Ni(NO_3)_2 \cdot 6\ H_2O$, 0.017 M $Mg(NO_3)_2 \cdot 6\ H_2O$ and 0.033 M $Al(NO_3)_3 \cdot 9\ H_2O$ were used. A small amount of conc. nitric acid (65 wt%) was added to lower the pH to 1 - 2. The same amounts of salts were combined to prepare the ternary Ni,Mg,Al nitrate solution resulting in a molar Ni:Mg:Al ratio of 50:17:33. The titration experiments were performed at 25 and 50 °C. The temperature was controlled by a water bath.

The catalysts were prepared by constant pH co-precipitation at 50 °C from aqueous 0.6 M NaOH, 0.09 M Na_2CO_3 solution and 0.4 M aqueous metal nitrate solution. The nitrate solution was dosed into 400 ml deionized water with 10 g min^{-1}. An automated laboratory reactor (Mettler-Toledo Labmax) controlled the addition of the base to keep the pH constant at 8.5. The product was subsequently aged for 30 minutes in the mother liquor. The precipitate was thoroughly washed with deionized water until the conductivity of the filtrate was below 0.5 mS cm^{-1} and dried in air at 100 °C for 16 h. The obtained bluish green precursor was calcined in air at 600 °C for 3 h yielding almost amorphous mixed oxides.

X-ray powder diffraction (XRD) measurements were performed with a STOE STADI-P transmission diffractometer equipped with a primary focusing Ge(111) monochromator and a 3° linear position sensitive detector (PSD) using CuKα1 radiation. Small amounts of X-ray amorphous grease was used to fix the powder samples between two thin films of polyacetate foil. Ni domain sizes were determined using TOPAS software [S2], after reduction and subsequent passivation of the Ni metal particles by slow increase of oxygen partial pressure at room temperature. Therefore the double-Voigt approach [S3] was used and reported as LVOL-IB values (volume-weighted mean column length based on integral breadth). Specific surface areas of the calcined material and the precursors were carried out by N_2 physisorption (Quantachrome Autosorb-1) and evaluated using the BET method. The samples were outgassed for 4 h at 100 °C.

Thermogravimetric analysis (TG) and evolved gas analysis (EGA) of the decomposition reaction were achieved by using a NETZSCH STA449 thermobalance under controlled gas flow (21 % O_2 in Ar, 100 Nml min^{-1}) connected to a quadrupole mass spectrometer (QMS200 OMNISTAR, Balzers). The measurements were performed with approximately 15 mg sample in a temperature range of 30-1000 °C (2 K min^{-1}).

Temperature-programmed reduction (TPR) of the samples was performed in a fixed-bed reactor (TPDRO-1100, CE Instruments) in 5 % H_2/Ar (80 Nml min^{-1}), with a heating rate of 6 K min^{-1}, in a quartz tube. The H_2 consumption was monitored with a thermal conductivity detector (TCD).

To determine the nickel metal surface area, a H_2 pulse chemisorption method was applied. Therefore the samples were reduced in 5% H_2/Ar (80 Nml min^{-1}), with a heating rate of 6 K min^{-1} in a fixed-bed reactor. After cooling down to 50 °C in Ar, a defined volume of H_2 gas (100 %) is introduced by pulse-dosing with a volume of 250 µl. The pulses were continued until no further uptake was 12 detected. The Ni metal surface area was determined assuming a dissociative chemisorption mechanism of hydrogen (Sf= 2; 2Ni/H_2) [S4].

For morphological studies of the materials, SEM images were acquired with a Hitachi S-4800 scanning electron microscope equipped with a field emission gun. The samples were loosely dispersed on conductive carbon tape (Plano). The SEM was operated at low accelerating voltage (1.5 kV) for a better resolution of the surface features of the samples. Elemental analysis by using X-ray energy dispersive spectroscopy (EDX) was carried out at 15 kV using an EDAX detector connected to the SEM.

The microstructure of the samples was examined by using a Philips CM200 transmission electron microscope (TEM) equipped with a LaB_6 cathode. The samples were dispersed in chloroform and deposited on a holey carbon film supported on a copper grid. High-resolution images were taken with a CCD camera. Before the measurement the samples were reduced and subsequent passivated by slow increase of oxygen partial pressure at room temperature.

To characterize the carbon deposition that has been formed on the catalyst during DRM Raman spectroscopy was applied at room temperature. A LabRam spectrometer was used with a 633 nm laser excitation from a HeNe laser and a power of 20 mW at the laser output. All data were obtained with a BX40 Olympus microscope (objective 100). Acquisition times were typically 3 x 180 s. Prior to experiments, the Raman spectrometer was calibrated using a Si wafer.

For the catalytic experiments, 10 mg of the htl-derived $Ni/MgO/Al_2O_3$ catalyst (sieve fraction of 250-355 µm) with 55 wt% Ni prior calcined at 600 °C were used in a fixed-bed tubular quartz reactor. The sample was diluted in 490 mg SiC. For pretreatment, the catalyst was heated at a constant rate of 5 K min^{-1} up to 800 °C and held at this temperature for 30 min in 20 Nml min^{-1} 4 % H_2/Ar. After purging in Ar, DRM was performed at 800 or 900 °C in 240 Nml min^{-1} 40 % CO_2/32 % CH_4/Ar for 1 or 100 h, respectively. Afterwards, the sample was cooled to room temperature in Ar. In case the samples were not ex-situ characterized by TEM directly after DRM a subsequent TPO experiment was performed by heating the sample with 5 K min^{-1} in 40 Nml min^{-1} 4.5 % O_2/Ar up to 800 °C. Product gas analysis was performed using a multi-channel gas analyzer (MLT 4, Emerson) and a paramagnetic oxygen detector (Magnos 16, Hartmann & Braun) for transient experiments and a calibrated GC for the activity tests (Shimadzu GC-14B).

The interface ratio (IFR) is the part of the particle that is in contact with the support phase and therefore not accessible for reactive gases. It can be calculated as the ratio between a theoretical surface area (SA_{theo}), calculated from the particle size that is determined by TEM, and the metal surface area (SA_{Ni}), determined by H_2 pulse chemisorption.

$$\mathrm{IFR} = 1-(\mathrm{SA}_{\mathrm{Ni}} / \mathrm{SA}_{\mathrm{theo}}),$$

where $\mathrm{SA}_{\mathrm{theo}}$ is calculated from the surface area (A_{Ni}) and the volume (V_{Ni}) and the density of Ni ($\rho_{\mathrm{Ni}} = 8.90\ \mathrm{g\ cm^{-3}}$):

$$\mathrm{SA}_{\mathrm{theo}} = A_{\mathrm{Ni}} \cdot \mathrm{wt\%}_{\mathrm{Ni}} / \rho_{\mathrm{Ni}} \cdot V_{\mathrm{Ni}}$$

2.6.5 SI References

[S1] A. Sadezky, H. Muckenhuber, H. Grothe, R. Niessner, U. Pöschl, *Carbon* **2005**, 43, 1731-1742.

[S2] TOPAS version 3, copyright **1999**, **2000** Bruker AXS.

[S3] D. Balzar, *Defect and Microstructure Analysis by Diffraction*, (Eds: R. L. Snyder, H. J. Bunge, J. Fiala), Oxford University Press, New York, **1999**.

[S4] M. Fadoni, L. Lucarelli, *Stud. Surf. Sci. Catal.* **1999**, 123, 289-342.

3 Development of high-temperature stable Ni nanoparticles for the dry reforming of methane at 900 °C

Katharina Mette, Stefanie Kühl, Andrey Tarasov, Thomas Lunkenbein, Marc Willinger, Jutta Kröhnert, Sabine Wrabetz, Annette Trunschke, Hendrik Düdder, Kevin Kähler, Martin Muhler, Robert Schlögl, Malte Behrens

Abstract

The catalytic dry reforming of methane (DRM) has been studied as an attractive option to produce synthesis gas since many years. However, catalyst deactivation by coking over non-precious metal catalysts remains still unresolved. Here, we study the influence of structural and compositional properties of nickel catalysts on catalytic performance and coking propensity in the DRM to shed light on structure-performance-relationships. A series of bulk catalysts with different Ni loadings was synthesized by a controlled co-precipitation method over hydrotalcite–like precursors. The obtained Ni/MgAl oxide catalysts consist of metallic nanoparticles (7 to 20 nm). By high resolution-transmission electron microscopy (HR-TEM) an oxidic overgrowth was found on the Ni particles. The surface properties were investigated by CO adsorption using microcalorimetry and IR spectroscopy. At low Ni contents (5 mol%) the catalyst exhibits a predominantly oxidic surface with an infrared (IR) band of Ni^{2+}-CO at 2177 cm^{-1} and additionally some isolated Ni^0 sites with a CO adsorption heat of 92 kJ mol^{-1}. These properties, determined by the overgrowth, effectively diminish coke formation during DRM, while the activity is preserved. A large and dynamic metallic Ni surface at high No contents (50 mol%), however, causes significant coke formation during DRM.

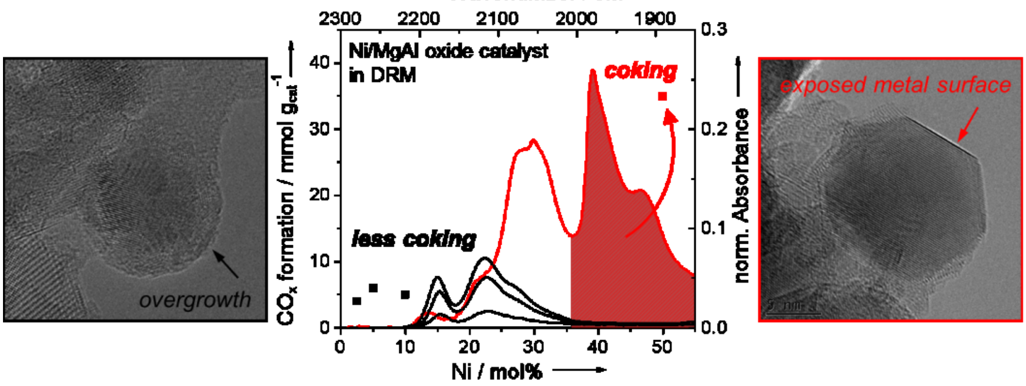

3.1 Introduction

Production of synthesis gas by dry (CO_2) reforming of methane (DRM) was first suggested in 1928 by Fischer and Tropsch [1] who were interested in an alternative to coal gasification. Already in their comparative study Ni-Al_2O_3 and Co-Al_2O_3 supported on clay fragments have been identified as the most active materials. Since then, catalyst synthesis has been developed considerably and gained in complexity [2]. Today, new methods allow better insights into the role of preparation parameters, leading to better control of the resulting material properties. For an enhanced efficiency of advanced technological processes, such as DRM, catalytic materials with well-defined properties are important. The challenging DRM process (eq. 3.1) is highly endothermic and, therefore, requires high reaction temperatures (> 640 °C [3]).In addition, coke deposition on the catalyst during DRM causes severe deactivation. Coke originates mainly from two routes: the Boudouard reaction (eq. 3.2) and methane pyrolysis (eq. 3.3). In order to prevent carbon deposition by the exothermic Boudouard reaction thermodynamically, high temperatures above 870 °C should be used [3]. For the establishment of an industrial DRM technology under these harsh conditions, catalyst development becomes a major aspect of research.

$$CO_2+CH_4 \rightarrow 2\ CO+2\ H_2 \qquad \Delta H_{298} = 247\ \text{kJ mol}^{-1} \qquad (3.1)$$

$$2\ CO \rightarrow CO_2+C \qquad \Delta H_{298} = -172\ \text{kJ mol}^{-1} \qquad (3.2)$$

$$CH_4 \rightarrow C+2\ H_2 \qquad \Delta H_{298} = 75\ \text{kJ mol}^{-1} \qquad (3.3)$$

Most of the group VIII metals were identified as suitable catalysts. In particular, the noble metals are showing high activities and selectivity for a carbon-free operation [4]. However, economical considerations prevent the commercial use of noble metals due to their high cost and limited availability. The development of a Ni-based catalyst is, therefore, desirable for commercial applications. However, one of the major challenges for the use of nickel is the high propensity towards coke formation, which becomes apparent because nickel also efficiently catalyzes the deposition of carbon [5].The preparation of coke resistant Ni catalysts can be achieved by the use of a promoter, changing the support, or by optimizing the catalyst's preparation. Furthermore, the synergy of size, morphology, structure, and composition is important to be considered for the design of Ni-based DRM catalysts [6]. A proper selection of a suitable support is crucial. In particular, the specific surface area and the acid-base properties of the support can affect the catalytic activity. Since the DRM involves the adsorption and dissociation of acidic CO_2, basic supports like MgO can enhance the ability of CO_2 chemisorption, which increases the coke resistance of the catalyst [3]. Moreover, a strong interaction between nickel and the support can improve the coke resistance significantly. SMSI (strong metal-support interaction) effects and surface overlayers are playing a major role in many catalyst systems, like in the industrial $Cu/ZnO/Al_2O_3$ methanol catalyst [7]. Here, a dynamic SMSI effect strengthens the binding of the intermediates and, thereby, increases the activity of the catalyst.

There are many experimental studies indicating that also the size of Ni particles has a strong effect on the selectivity during DRM reaction [8,9]. Kim et al. [10], for example, studied the influence of the Ni concentration on the DRM activity over a Ni/NaY catalyst. By varying the Ni content between 1 and 10 wt.% they obtained a maximum conversion of CO_2 and CH_4 with a 3.3 wt.% Ni loading. However, the coke formation increased as the amount of nickel on the support increased, whereas the intrinsic performances were found to be independent of nickel particle size in low temperature DRM. Kim et al. [11] prepared Ni-alumina aerogel catalysts with various Ni loadings to generate different Ni particle sizes. They found that large Ni particles are prone to grow carbon whisker and that a minimum diameter of about 7 nm is required for Ni particles to generate filamentous carbon. This is in agreement with the study of Martínez et al. [12] on the particle size limit for carbon filament formation. They observed that Ni-Al-La catalysts with Ni particles sizes below 10 nm showed an absence of filaments. Juan-Juan et al. [13] varied the nickel particle size between 6.3 and 7.8 nm by applying different pretreatment procedures on a Ni/Al_2O_3 catalyst. They found a direct correlation of the mean particle size and the amount of carbon deposited. The activity in DRM at 700 °C, however, was not affected by the pretreatment. In a recent study, Chen et al. [14] report on the effect of Ni crystal size on the growth of carbon nanofibers during methane decomposition at 580 °C. An optimal growth rate and yield of carbon nanofibers were achieved on 34 nm sized Ni crystals, smaller and bigger Ni particles exhibited lower growth rates.

Despite all the efforts that have been made, the preparation of coke resistant Ni catalysts for DRM remains still a significant challenge. The major task is to prepare a thermally stable, highly active and selective material. We have recently shown that a Ni/MgAl oxide catalyst obtained by co-precipitation of a hydrotalcite-like (htl) precursor can at least partly fulfill these requirements, although coke formation is not completely eliminated [15].

Catalytic applications of htl precursors as catalysts and catalyst supports have been intensively investigated in recent years and comprehensive reviews are available [16,17,18]. Their application as precursors for the preparation of Ni catalysts for DRM has been studied by several groups. Takehira and co-workers [19,20] as well as Perez-Lopez et al. [21], for instance, presented different synthetic approaches of htl-derived $Ni/MgO/Al_2O_3$ catalysts in

DRM. In [21] an influence of the catalyst composition and reduction temperature on the catalytic properties of Ni–Mg–Al catalysts prepared by continuous co-precipitation was found. These parameters affect the crystallite size and the acid–base character of the surface, leading to differences in the catalytic properties in DRM. For a molar composition of Ni:Mg:Al of 55:11:33 the highest resistance to coke deposition and highest activity have been reported, which can be ascribed to very small Ni particles of 5 nm.

The main objective of this work is to study the influence of structural and compositional properties of nickel catalysts in the DRM. Catalysts with different Ni contents were prepared by co-precipitation, extensively characterized, and studied concerning their DRM and coking performance. We show the detailed characterization of the catalyst in all stages of the preparation as well as after the reaction. To elucidate structure-activity-relationships, the surface properties were investigated by CO adsorption using microcalorimetry and IR spectroscopy. Our experimental findings give new insights into the current state of reforming knowledge and coke resistance. Selected results of individual samples presented here have already been reported in previous publications [15,22].

3.2 Results and Discussion

Ni/MgAl oxide catalysts were prepared from htl precursors. Calcination of the dried precursors and reduction in flowing hydrogen led to the final catalysts. Various characterization methods were applied at selected stages of the preparation to evaluate structural changes and to optimize the synthesis procedure. The resulting catalysts were studied to determine the influence of the catalyst composition on the catalytic activity and coking behavior in the DRM.

3.2.1 Properties of the htl precursors

A series of ternary hydrotalcite-like (htl) precursors of the general composition $(Ni^{2+},Mg^{2+})_{1-x}\ Al_x^{3+}\ (OH)_2\ (CO_3)_{x/2} \cdot nH_2O$ ($x = 0.33$) was synthesized using a constant pH co-precipitation technique (Table 3.1, for the synthesis profile see the Supporting Information (SI), Figure S3.1). Within the sample series, Mg^{2+} was partially substituted by Ni^{2+} to vary the Ni content from 0 to 50 mol% of all metal species. The Al^{3+} concentration was kept constant at 33 mol% in order to maintain a constant M^{2+}/M^{3+} ratio of 2:1 to obtain phase-pure htl compounds. The structure of hydrotalcites is based on lamellar brucite ($Mg(OH)_2$)-like layers where some divalent Mg^{2+} cations have been replaced by trivalent Al^{3+} cations generating positively charged sheets. This extra charge is compensated by CO_3^{2-}

anions located in the hydrated interlayer. The structural properties of hydrotalcites are described in various reviews [23,24,25,26].

Table 3.1 Composition and specific surface areas of the htl precursors and the mixed oxides.

Precursor Label	Ni:Mg:Al ratio	BET-SA$_{prec.}$ / m^2 g^{-1}	XRD-FWHM 003 / °2θ	Label	BET-SA$_{calc.}$ / m^2 g^{-1}
Ni50	50:17:33	134	1.175	Ni50-600	226
Ni25	25:42:33	148	1.118	Ni25-600	221
Ni15	15:52:33	171	1.023	Ni15-600	270
Ni10	10:57:33	192	n.d.	Ni10-600	250
Ni7.5	7.5:59.5:33	192	n.d.	Ni7.5-600	258
Ni5	5:62:33	140	0.945	Ni5-600	205
Ni2.5	2.5:64.5:33	118	n.d.	Ni2.5-600	215
Ni1	1:66:33	113	0.774	Ni1-600	180
Ni0	0:67:33	109	0.764	Ni0-600	134

n.d.: not determined

Powder X-ray diffraction (XRD) confirmed that all precursor materials crystallize in the htl structure (Figure 3.1). No other crystalline phase can be observed. The peak broadening of the reflections indicates that small crystallite sizes were successfully obtained. Within the series, the crystallinity of the htl phase is increasing with decreasing Ni content, as expressed in the decreased full width half maximum (FWHM) of the (003) reflection (see Table 3.1).

As previously shown for Ni50 [15], all precursors are characterized by the typical platelet-like morphology of hydrotalcites (SEM images presented in the SI, Figure S3.2a). The lateral size of the platelets is up to approximately 200 nm and the thickness is in the low nm range. The corresponding elemental mapping of Ni50 illustrates the homogeneous metal distribution of all three species (Figure S3.3). The specific surface areas (SA) of the htl precursors, determined by nitrogen physisorption (Brunauer-Emmett-Teller method (BET)) are relatively high, ranging from 109 to 192 m^2 g^{-1}, with a maximum between Ni7.5 and Ni10 (Table 3.1). All materials show a pronounced hysteresis in the N_2 isotherms as a result of mesoporosity (see the SI, Figure S3.4). Within the series, the pore sizes of the precursors increase from 42 to 132 Å with decreasing Ni and increasing MgO content (see the SI, Figure S3.5). Since the uncalcined htl material is likely not intrinsically porous, the pore size here is best understood as the average inter-particle distance between the platelets.

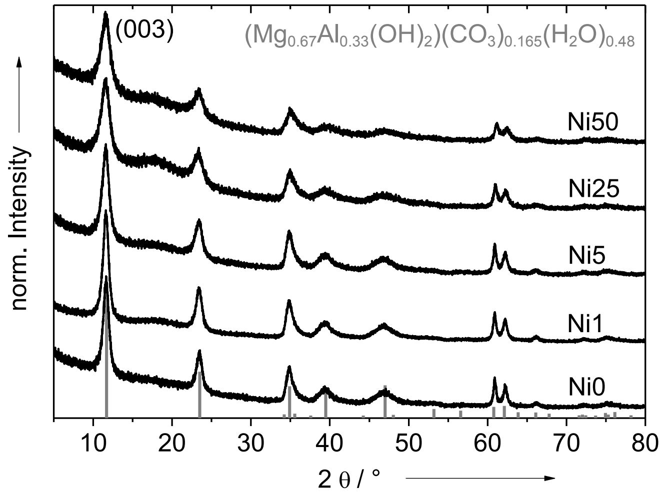

Figure 3.1 Powder XRD patterns of the NiMgAl htl precursor materials with different Ni and Mg contents. The grey bars correspond to: $(Mg_{0.67}Al_{0.33}(OH)_2)(CO_3)_{0.165}(H_2O)_{0.48}$ (ICDD: 89-5434).

The transformation of the htl precursors into mixed oxides during calcination in synthetic air was investigated by thermogravimetric measurements coupled with mass spectrometry (TG-MS). The resulting TG profiles, the total mass loss, and the corresponding MS signals of H_2O and CO_2 are shown in Figure 3.2. The precursors are characterized by the typical thermal decomposition behavior for htl compounds. After drying, the decomposition can be divided into two steps [23]: (i) release of interlayer water between 125 and 225 °C and simultaneously of small quantities of CO_2 from weakly bound carbonates and (ii) bimodal dehydroxylation of the brucitic layers and decarboxylation of the interlayer between 225 and 500 °C. The total mass loss measured for all samples ranges between 38 and 46%. The measured values are in reasonable agreement with the calculated amounts for htl decomposition into the pure oxides. Assuming a water content of $n\mathrm{H_2O} = 0.5\mathrm{H_2O}$ according to [23], a theoretical mass loss of 36 wt.-% for Ni50 and of 44 wt.-% for Ni0 was calculated. The decomposition temperatures are shifted to higher values with lower Ni content, indicating a higher thermal stability that might be attributed to the higher crystallinity that was discovered by XRD (Figure 3.1). For all samples, the decomposition can be assumed to be completed at 600 °C as no further significant mass loss is observed at higher temperatures. Therefore, 600 °C was chosen as calcination temperature.

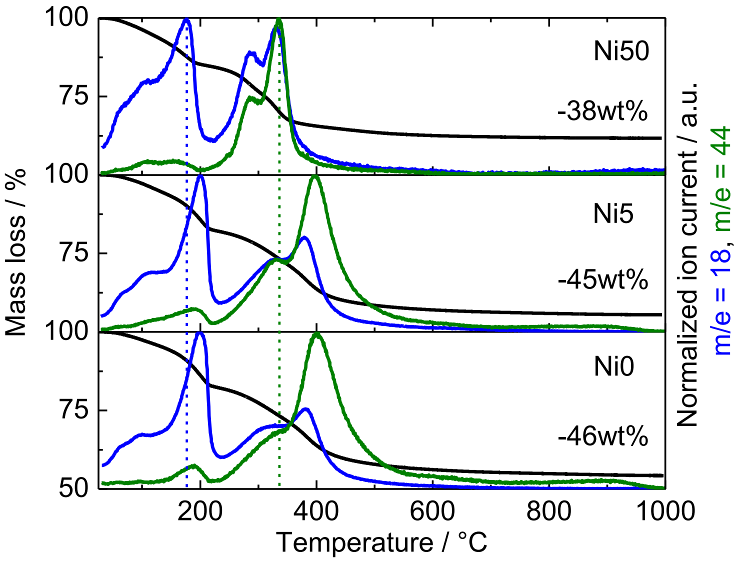

Figure 3.2 TG-MS results for the thermal decomposition of selected precursor samples in 21% O_2 in Argon (2 K min^{-1}). The black (▬) lines correspond to the mass loss (TG signal), blue (▬) and green (▬) lines to the MS traces of water ($m/z = 18$) and CO_2 ($m/z = 44$). The total mass loss is given, measured over the whole temperature range of the experiments (30-1000 °C).

3.2.2 Mixed Oxides

The mixed oxides that are obtained by calcination were investigated with various characterization methods. After calcination at 600 °C, the htl structure of the precursors is decomposed into poorly crystalline NiMgAl mixed oxides regardless of the Ni content (Figure 3.3). Similar lattice constants of MgO and NiO and of $MgAl_2O_4$ and $NiAl_2O_4$, and the possible formation of solid solutions lead to complex diffraction patterns with overlapping reflections. Broad peaks at the positions of the most intense (111), (200) and (220) lines of a rock-salt structure-type phase (NiO or MgO) are observed at $2\theta \approx 37°$, 43° and 63° 2θ, respectively. At higher angles, where the differences between the two phases are more pronounced only broad modulations of the background can be observed (Figure 3.3, right). A potential spinel phase is X-ray amorphous in all samples, as no peaks corresponding to $MgAl_2O_4$ or $NiAl_2O_4$ can be detected. The samples, however, exhibit a broad peak at 35° 2θ, indicating the presence of an unknown by-phase that might be Al_2O_3 although the reflex intensities does not fit precisely.

A satisfactory phase refinement of the diffraction pattern could not be achieved using the Rietveld (whole-profile) method. In structure refinements, the misfits are rarely caused by a single variable as the peak shape itself is a function of both the sample's microstructure (e.g. domain size, stress/strain, defects, stacking faults and anisotropy) and the instrument (e.g. radiation source, geometry and slit sizes) [27]. The adjustment of all these aspects in a single peak-shape description is not trivial. Furthermore, a preferred orientation of crystallites can influence the relative intensities of Bragg reflections. For patterns with many overlapping reflections, as in the present case, the majority of the peaks are not resolved to the baseline. Thus, the estimation of the background remains difficult [28]. In addition, fluorescence can lead to an unusually high background.

The well preserved platelet-like morphology demonstrates the stability after calcination at 600°C (images presented in SI, Figure S3.2b. The lateral size of the platelets, however, is shrunk to approximately 150 nm, leading to an increased specific surface area as well as an increased distance between the platelets (for the pore size distributions, see the SI, Figure S3.5). Within the series of the calcined samples the specific surface area decreases with decreasing Ni and increasing MgO content (Table 3.1). The reduction of surface area is proportional to an increase of pore sizes (see the SI, Figure S3.5).

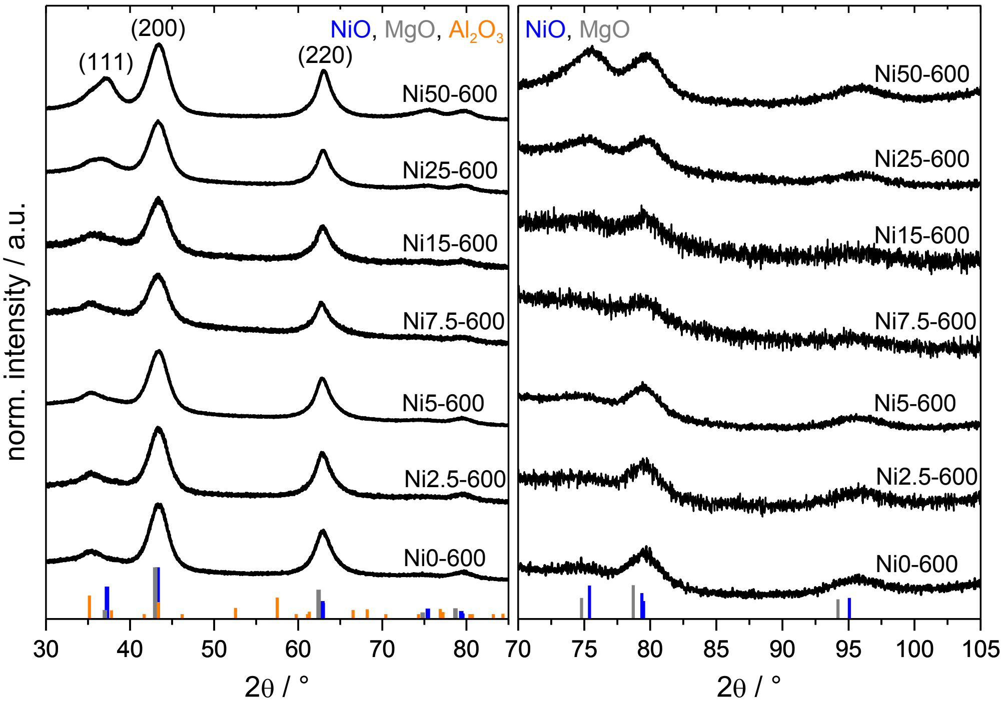

Figure 3.3 Powder X-ray diffraction patterns of the htl precursors after calcination in air at 600 °C. The blue bars (▬) correspond to: NiO (ICDD: 47-1049), the grey bars (▬) to: MgO (ICDD: 65-476) and the orange bars (▬) to Al_2O_3 (ICDD: 46-1212). On the right hand side the resolution is increased at higher angles.

Since XRD detects only crystalline materials and the oxidic components cannot be distinguished (see above), near-edge X-ray absorption fine structure measurements (NEXAFS) of Ni50-600 and Ni5-600 were accomplished to assign the crystalline and additional amorphous phases. The Al K-, Mg K- and Ni L-edges show a rich fine structure, owing to a multiplet splitting that is very sensitive to the local chemical environment.

Different oxidic reference materials were used to evaluate the NEXAFS data. Commercial NiO and co-precipitated and calcined $NiAl_2O_4$ were used as reference materials for Ni^{2+} species. Commercial γ-Al_2O_3 and co-precipitated $MgAl_2O_4$ were selected as reference materials for Al^{3+} species. Mg^{2+} species were compared with (co-) precipitated MgO and $MgAl_2O_4$. The Al K-, Ni L- and Mg K-edge NEXAFS spectra of Ni50-600 are presented in Figure 3.4 (spectra of Ni5-600 in the SI, Figure S3.6). Despite the phase pure and uniform htl precursor material, linear combination fitting of the Ni L-edge spectra of Ni50-600 with the oxidic references verifies that the nickel signal is comprised of two different species, both exhibiting a +2 oxidation state: NiO and $NiAl_2O_4$ (Figure 3.4b). A similar picture appears for the Al K-edge. Here it becomes evident that also Al^{3+} occurs in diverse environments: $MgAl_2O_3$ and Al_2O_3 (Figure 3.4a). The fitting of the Mg K-edge is more difficult. No acceptable linear combination fit could be obtained with the chosen reference materials (Figure 3.4c). This might be due to inapplicable reference materials which possess a different chemical environment than the material under study, e.g. due to the formation of solid solutions with NiO and MgO.

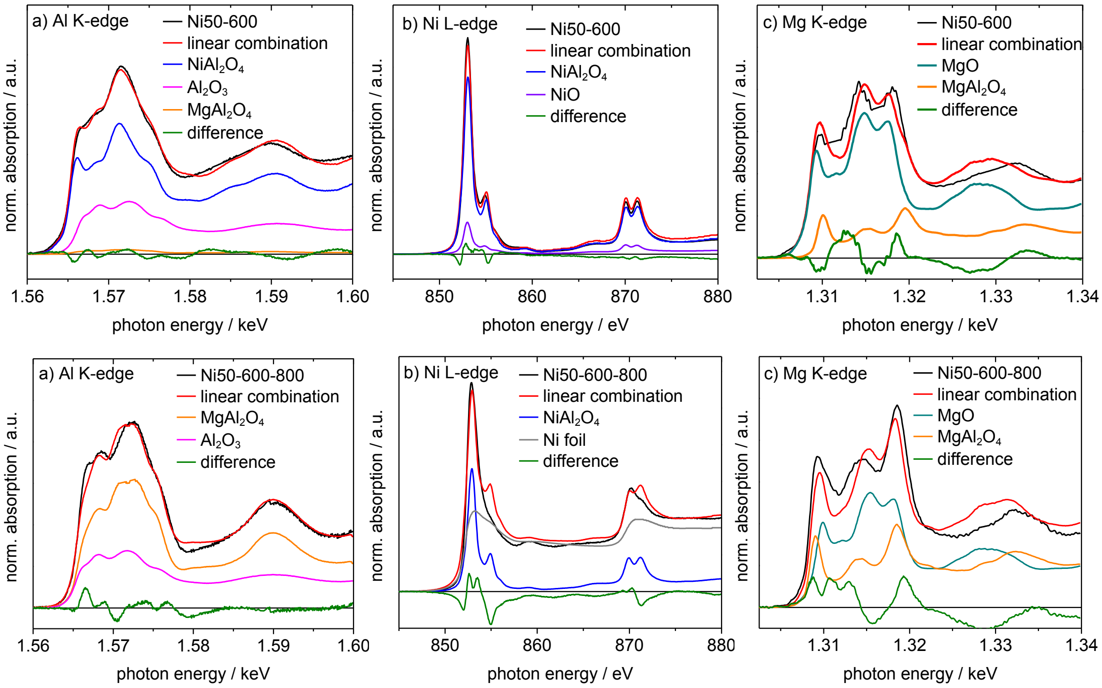

Figure 3.4 Linear correlated (a) Al K-, (b) Ni L- and (c) Mg K-NEXAFS spectra of calcined Ni50 (top) and reduced Ni50 (bottom).

The reduction behavior of the materials calcined at 600 °C was investigated by temperature-programmed reduction (TPR) measurements in 5% H_2/Ar (Figure 3.5). The reduction temperature is increasing from 663 to 914 °C with decreasing Ni content, indicating to an increased dispersion of the Ni species in the oxidic support. In general, higher reduction temperatures might be explained by the presence of $NiAl_2O_4$ that was observed by NEXAFS measurements. $NiAl_2O_4$ is reduced at higher temperatures than NiO due to a stronger interaction of Ni with the matrix [29]. Moreover, a lower reduction temperature can indicate a lower stability of the Ni phases. The quantification of the degree of reduction from the hydrogen consumption turned out to be complex for these samples. Unexpectedly, excessive hydrogen consumption was observed at high temperatures for the Ni-free sample Ni0-600. Likewise, samples with a Ni content below 10 mol% showed a higher hydrogen consumption than expected for a stoichiometric reduction of Ni^{2+} to Ni^0. CO_2, CO and CH_4 have been detected by MS during reduction of Ni0-600 (Figure 3.6a). We assume that CO_2 is released as a decomposition product of residual interlayer carbonate ions of the htl precursor and/or of organic species absorbed from the atmosphere [30,31]. According to the observed MS traces, CO_2 undergoes the reverse water gas shift reaction (rWGS, eq. 3.4) and methanation reactions (eq. 3.5), which results in a considerably higher H_2 consumption than expected and in the formation of CO and CH_4. In case of Ni1-600 and Ni5-600 the hydrogen uptake due to rWGS and methanation overlaps with the Ni^{2+} reduction.

$$CO_2+H_2 \rightarrow CO+H_2O \qquad \Delta H_{298}= 41\ \text{kJ mol}^{-1} \tag{3.4}$$

$$CO_2+4\ H_2 \rightarrow CH_4+2\ H_2O \qquad \Delta H_{298}= -165\ \text{kJ mol}^{-1} \tag{3.5}$$

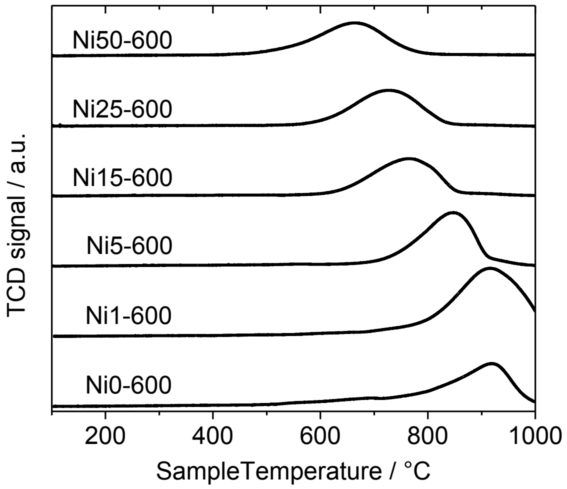

Figure 3.5 TPR profiles of the htl samples calcined at 600 °C using a linear heating ramp of 6 K min^{-1} in 5% H_2/Ar (60 ml min^{-1}).

In a subsequent temperature-programmed oxidation (TPO) of the Ni-free sample, oxygen consumption was observed at temperatures above 600 °C. At the same time, CO_2

was detected by MS (Figure 3.6b). This leads us to the assumption that CO and/or CH_4 formed during reduction undergo Boudouard (eq. 3.2) and/or pyrolysis reactions (eq. 3.3), respectively, and form carbon depositions in the catalyst bed. Thus, at sufficiently high temperatures the deposited carbon is oxidized to CO_2. Hence, under reducing conditions CO_2 derived from the decomposition of residual interlayer carbonates is partially converted to carbon even in absence of metallic Ni and/or the CO_2/CH_4 reaction mixture.

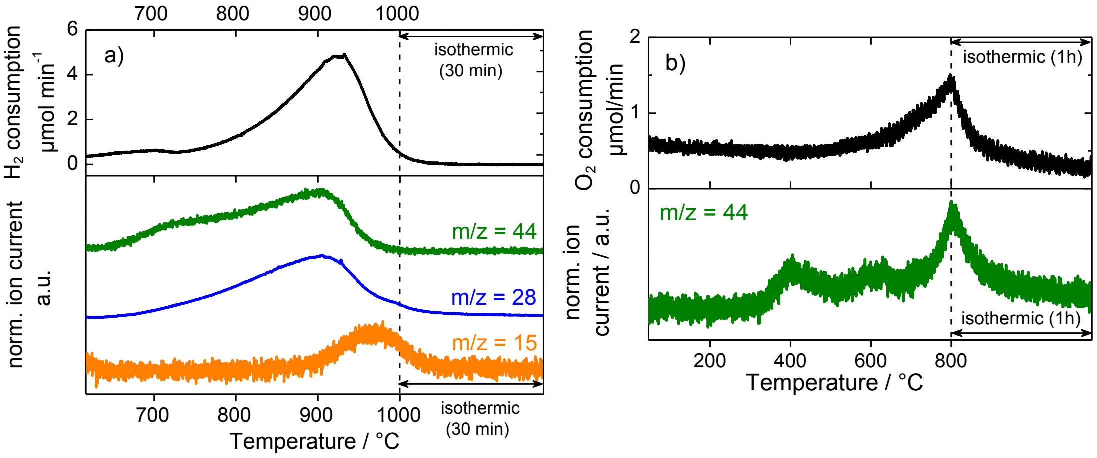

Figure 3.6 TPR-MS profile of Ni0-600 in 5% H_2/Ar (a) and subsequent TPO-MS profile in 5% O_2/He (b). MS traces of CO_2 (m/z = 44), CO (m/z = 28) and CH_4 (m/z = 15).

3.2.3 Properties of the ex-htl samples after reduction

Based on the TPR profiles suitable reduction temperatures were chosen to ensure the complete reduction of nickel oxide for all samples. Phase assignments of the reduced samples were done with NEXAFS. The Al K-, Ni L- and Mg K-edge spectra of the Ni50-600-800 fitted with the reference materials are shown in Figure 3.4 (spectra of Ni5-600-1000 in the SI, Figure S3.7). $NiAl_2O_4$ has been reduced to Ni^0 and instead $MgAl_2O_4$ has been formed. The small fraction of remaining $NiAl_2O_4$ seen in the Ni L-edge might be explained by an incomplete reduction as a consequence of insufficiently high temperatures. Based on the NEXAFS analysis the irreducible component of the catalysts after reduction is assumed to consist of $MgAl_2O_4$ and MgO, instead of the corresponding Ni oxides.

Upon reduction a nanoscopic segregation of the components has taken place and the XRD (Figure 3.7) clearly confirms the presence of metallic Ni. Under the assumption of complete NiO reduction, MgO and a spinel phase can be identified in the reduced samples. The samples with a low Ni loading hardly show evidence of metallic Ni. The most intense reflection at $2\theta = 44.5\,°$ is superimposed by MgO and the spinel phase. While the oxidic components in the catalyst with the highest Ni content (Ni50) are still poorly crystalline, the intensity of the MgO and $MgAl_2O_4$ phases rises with decreasing Ni content. However, the pattern cannot be fitted satisfactorily with a conventional Rietveld fit, because of the complex line shape of the diffraction patterns as already discussed in chapter 3.2.2. Scanning electron micrographs (Figure S3.2c) of the reduced Ni50-600 show, that the platelet-like morphology of the htl-precursor is preserved after reduction at 800 °C [15]. In addition, small spherical particles that are homogeneously distributed over the platelets are observed.

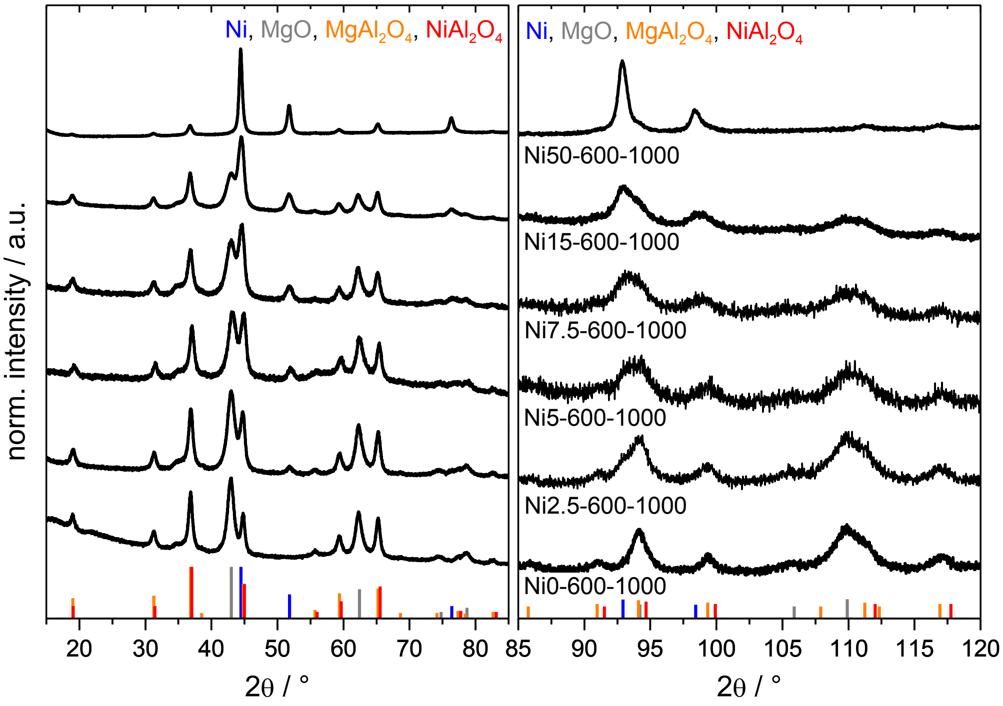

Figure 3.7 Powder XRD patterns of the mixed oxides after reduction at 1000 °C. The blue bars (▬) correspond to: Ni (ICDD: 65-2865), the grey bars (▬) to: MgO (ICDD: 65-476), the orange bars (▬) to $MgAl_2O_4$ (ICDD: 74-1132) and the red bars (▬) to $NiAl_2O_4$ (ICDD: 10-339). On the right hand side the resolution is increased at higher angles.

The morphology of the reduced samples and the size of the metallic Ni nanoparticles was further investigated by transmission electron microscopy (TEM) (Figure 3.8). Independent of the Ni content, nearly spherical Ni particles were formed, which are homogeneously dispersed in the oxide matrix. Decreasing the Ni content and simultaneously increasing Mg content alters the matrix morphology. With lower Ni content the crystallinity of the oxide matrix becomes intensified (see also Figure 3.7) and a large amount of crystalline needles are formed that likely consist of MgO or $MgAl_2O_4$. Surprisingly, the Ni content has only a minor influence on the Ni particle size. The average size ranges between 7 and 9 nm (Table 3.2). Only the catalyst with the highest Ni content shows substantial sintering and the avarage particle size is increased to 20 nm.

Table 3.2 Composition, particle sizes, Ni dispersion and IFR determined by TEM and H_2 chemisorption of the reduced samples.

Sample label	Ni content / wt.-%	Particle size TEM / nm	Ni SA / $m^2\ g_{cat}^{-1}$	Dispersion / %	IFR / %
Ni50-600-1000	55.4	19.4 ± 7.1	6.0	1.6	68.7
Ni25-600-1000	30.3	7.3 ± 2.0	5.0	2.5	82.1
Ni15-600-1000	18.9	9.0 ± 3.1	4.2	3.4	70.5
Ni10-600-1000	12.9	n.d.	3.2	3.7	n.d.
Ni7.5-600-1000	9.7	n.d.	2.7	4.2	n.d.
Ni5-600-1000	6.6	9.3 ± 3.7	3.0	6.9	37.3
Ni2.5-600-1000	3.3	n.d.	0.6	2.9	n.d.
Ni1-600-1000	1.3	7.0 ± 4.6	0.1	1.0	92.2
Ni0-600-900	0.0	-	0.0	0.0	100.0

n.d.: not determined

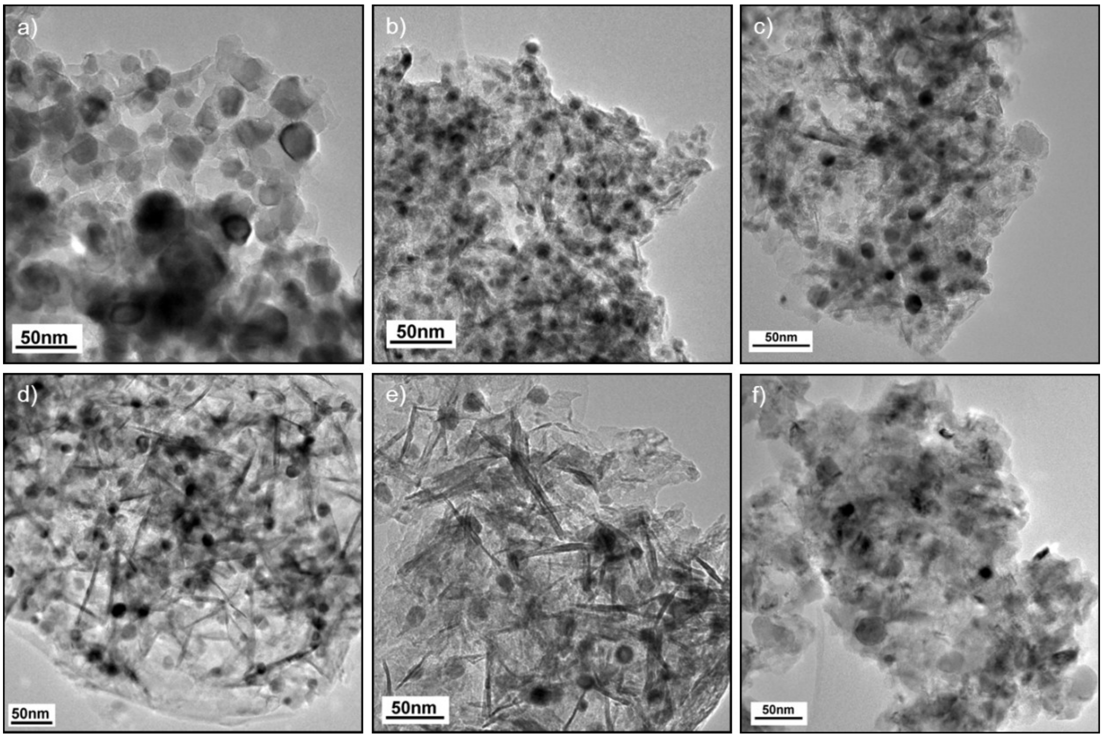

Figure 3.8 TEM micrographs of samples after reduction Ni50-600-1000 (a), Ni25-600-1000 (b), Ni15-600-1000 (c), Ni10-600-1000 (d), Ni5-600-1000 (e) and Ni1-600-1000 (f).

In a more detailed investigation, high resolution (HR) TEM/STEM (scanning transmission electron microscopy) images in combination with EDX analysis of Ni2.5, Ni5 and Ni50 were recorded. The samples have been transferred without exposure to air to the microscope assuring the absence of surface re-oxidation of the metallic Ni surface during transfer. The HR-TEM images of Ni2.5 and Ni5 at high magnification (Figure 3.9a,b) demonstrate the existence of a crystalline overgrowth on top of the Ni particles. While the coverage seems to be almost complete in these samples, the Ni50 catalyst clearly exhibits a certain fraction of exposed Ni surface (Figure 3.9c). The HR-STEM images of Ni2.5 in Figure 3.10a verify the homogeneous coverage of the nanoparticles. With increased Ni content the coverage becomes more rough and heterogeneous as it is shown by the STEM images of Ni5 in Figure 3.10b. This effect seems to be strengthened with further increasing Ni content. For the Ni50 catalyst (for HR-TEM images, see the SI, Figure S3.8) the overgrowth does not completely cover the nanoparticles and a fraction of the metallic Ni surface is exposed. The overgrowth on the Ni particles of the Ni5 sample is composed of Ni, Al and O as shown by the overlap of the corresponding EDX elemental maps in Figure 3.11a and might be interpreted as the formation of a $NiAl_2O_4$ spinel. Moreover, EDX line scans in Figure 3.11b can confirm the coexistence of Ni and Al.

The formation of a $NiAl_2O_4$ spinel is in line with previously reported data. It was observed that at high temperature nickel may react with the support, even with non-reducible alumina [32].The formation of a surface spinel is possible already during calcination at 600 °C and may hardly be identified by X-ray diffraction alone [33].A surface nickel aluminate has been observed on co-precipitated Ni,Al catalysts after reduction [34,35].The formation of such aluminates is denoted as medium metal–support interaction (MMSI) [36].

To further investigate the nature of the catalyst surface and the overgrowth various adsorption methods were applied using the products of the DRM reaction, H_2 and CO, as probe molecules.

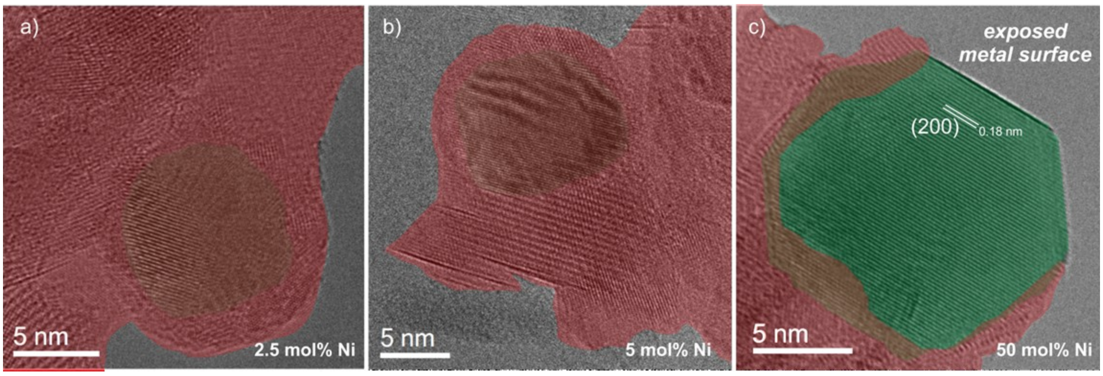

Figure 3.9 HR-TEM images of Ni2.5-600-1000 (a), Ni5-600-1000 (b) and Ni50-600-1000 (c). Red and green colors represent the overgrowth and Ni particles, respectively. (Please find uncolored images in the SI, Figure S3.9.)

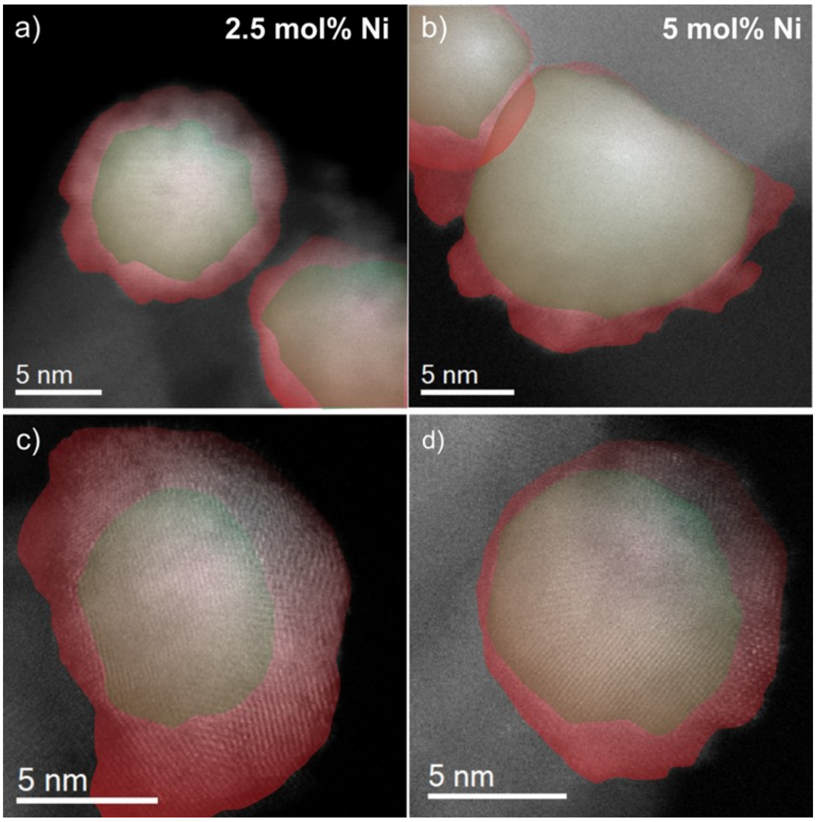

Figure 3.10 HR-STEM investigation of the overgrowth on Ni nanoparticles reduced at 1000 °C. High resolution STEM images of Ni2.5-600-1000 (a) and Ni5-600-1000 (b) Red and green colors represent the overgrowth and Ni particles, respectively. (Please find uncolored images in the SI, Figure S3.10.).

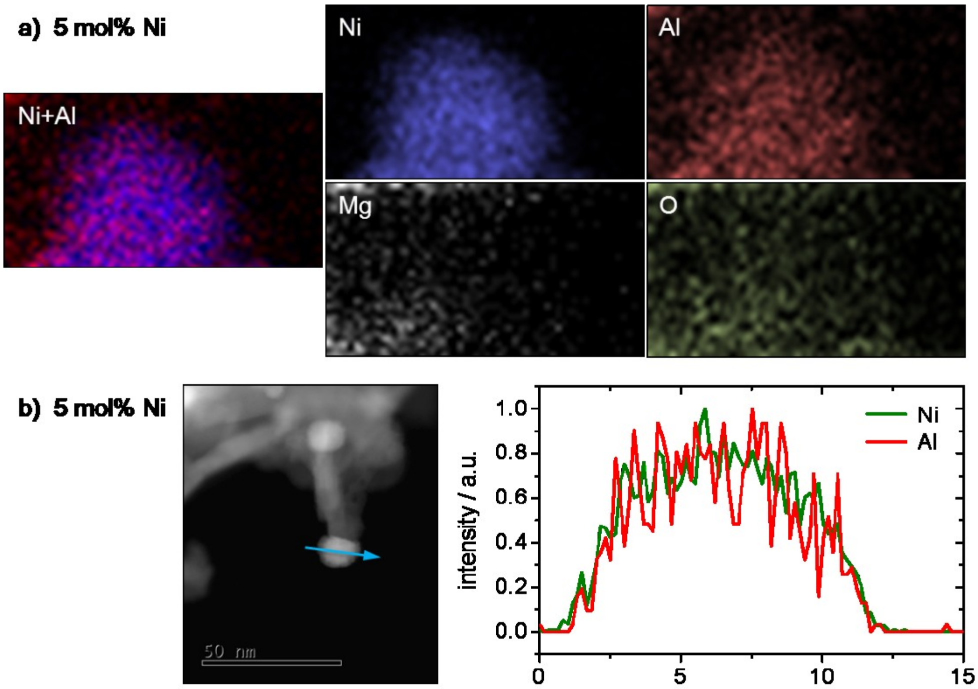

Figure 3.11 STEM-EDX elemental mapping (a) and line scans (b) of Ni nanoparticles in the Ni5-600-1000 sample.

3.2.3.1 Surface characterization

3.2.3.1.1 H_2 pulse chemisorption at 50 °C

In order to determine the accessible Ni metal surface area and to estimate the dispersion of the metal particles, H_2 pulse chemisorption measurements were applied after reduction. As expected, the Ni surface area is influenced by the Ni content. With decreasing Ni content the Ni metal surface area is decreasing (Table 3.2 and Figure 3.12a). Between the Ni content and the Ni dispersion a volcano type correlation has been found exhibiting a maximum at 5 mol% Ni (Figure 3.12b). The discrepancy between the Ni surface area, the dispersion, and the particle size can be explained by different degrees of embedment as it is reflected by the interface ratios (IFR) given in Table 3.2. As Ni5-600-1000 exhibits the lowest IFR, the particles are less embedded in the support and, therefore, possessing the highest dispersion despite similar particle sizes.

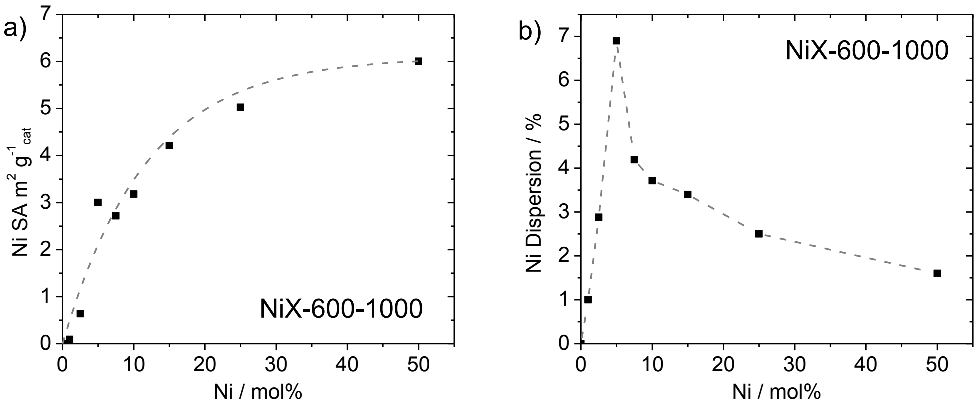

Figure 3.12 Correlations of the Ni content as a measure of Ni surface area and Ni dispersion (a) and (b) (lines are only guidelines for the eye).

3.2.3.1.2 CO adsorption at -196 °C

We applied infrared (IR) spectroscopy of adsorbed CO to gather qualitative information on the composition of the surface, the Ni oxidation state as well as the nickel dispersion. Adsorption of CO at -196 °C results in the formation of carbonyl species that interact coordinatively with unsaturated surface sites. The CO molecule forms σ-donor bonds with Mg and Al cations. Thereby, the CO stretching mode is shifted to higher wavenumbers. Adsorption of CO on Ni^0 results in π back bonding and a shift of the CO stretching mode to lower wavenumbers. In general IR bands above 2100 cm^{-1} are due to CO adsorption on cationic species. Band positions at 2100-2000 cm^{-1} indicate linear coordinated CO adsorption on metal sites, whereas vibrational modes below 2000 cm^{-1} indicates the formation of bridged carbonyls ($(Ni^0)_x$-CO) [37,38]. It can be assumed that a strong absorbance due to linearly bound carbonyls is indicative of a high dispersion. The appearance of bridged carbonyls, however, suggests the existence of agglomerates.

Since CO was dosed progressively, adsorption isotherms can be determined by plotting the integrated band areas as a function of the CO equilibrium pressure (Figure 3.13a). The different maximum areas refer to different CO adsorption capacities. A direct correlation of the CO adsorption capacity with the Ni content cannot be found. To take coupling effects between neighboring CO molecules into account, the different catalysts are compared at the same surface coverage. Therefore it is assumed that monolayer coverage (θ=1) is reached at 8 mbar CO and the isotherms were normalized accordingly.

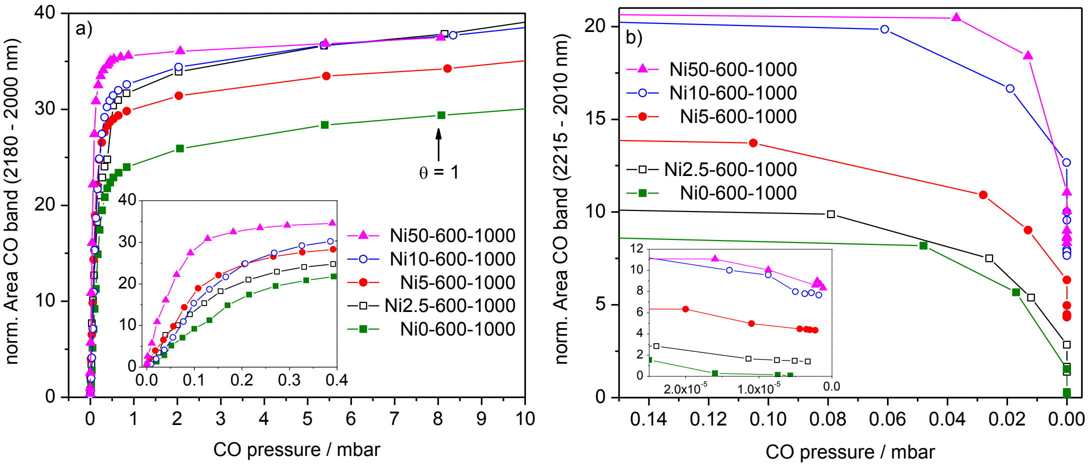

Figure 3.13 Integrated peak areas of adsorbed CO as a function of the equilibrium CO pressure at -196 °C (adsorption isotherms) (a). Integrated peak areas of desorbed CO as a function of pCO during evacuation at -196 °C (desorption isotherms) (b). Insets are showing magnified areas at low CO pressures. The areas were determined using spectra normalized to the mass per unit area of the wafer.

In Figure 3.14 the spectra of adsorbed CO at full coverage (θ=1) are compared for the reduced catalysts (a), as well as for the reference compounds (b). It should be noted that at full coverage coupling effects between neighboring CO molecules are expected, along with the appearance of molecular CO at 2143 cm^{-1}. One intense carbonyl band can be observed in all samples at 2158 cm^{-1}. The band can be ascribed to the carbonyl stretching vibration of CO chemisorbed on 5-fold coordinated Mg^{2+} ions [39]. The peak maximum for Ni50 is slightly shifted to 2162 cm^{-1} compared to the other samples. The lower intensity of the band on Ni50 might be related to the lower amount of Mg in this sample. The major difference of the Ni50 to the other samples is however the appearance of strong absorption in the range of 1800-2100 cm^{-1}. This indicates the formation of carbonyls on metallic Ni sites, both linear (2020-2065 cm^{-1}) and bridged (<2000 cm^{-1}) [37]. The absence of strong bands in this region indicates a mainly oxidic surface in the other samples.

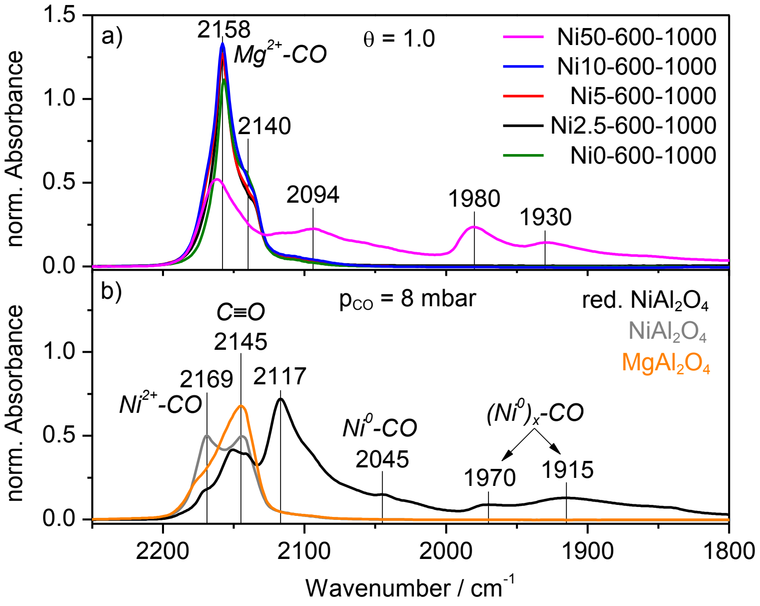

Figure 3.14 Transmission IR spectra of CO adsorbed at -196 °C on Ni catalysts at full coverage (a) and on reference samples at 8 mbar CO (b). The reduced catalysts (1000 °C, 5% H_2/Ar, 1h) were pretreated in 50 mbar of H_2 at 850 °C for 1 h. Spectra before CO dosing were used as background. The spectra were normalized to the mass per unit area of the wafer.

After CO adsorption at 20 mbar the IR cell was evacuated progressively. In Figure 3.13b the corresponding desorption isotherms are presented. The amount of residual adsorbed CO correlates with the Ni content and is reduced with decreasing Ni content. In Figure 3.15a the spectra of the residual bands are shown for reduced catalysts (top), as well as for reference compounds (bottom). The CO bands of the Ni free sample (Ni0) as well as of the $MgAl_2O_4$ reference disappear by evacuation, because Mg^{2+}- and Al^{3+}-CO bonds are mainly electrostatic and not stable under evacuation. Therefore, all bands present under this condition are related to nickel carbonyls.

Ni50 still shows a main contribution of metallic Ni species between 2100 and 1800 cm^{-1}. The formation of bridged carbonyls ($(Ni^0)_x$-CO) at 2000-1850 cm^{-1} is very distinct, indicating a high concentration of agglomerates on the surface. Additionally, the bands between 2100 and 2000 cm^{-1} suggests the coexistence of linear carbonyls and thus highly dispersed Ni^0 species. The bands at even higher wavenumbers (2100-2210 cm^{-1}) pointing to the presence of a small fraction of unreduced nickel. The reduced $NiAl_2O_4$ reference shows basically the same features.

For lower Ni concentrations (2.5-10 mol%) the presence of at least three different nickel species is suggested and characterized by absorption bands at 2078, 2117 and 2177 cm^{-1} (Figure 3.15b). The last band corresponds to Ni^{2+} species as the major band of the $NiAl_2O_4$ reference appears in the same region. All three species increase with the Ni content. The bands below 2100 cm^{-1} (linear CO species) suggest the existence of few dispersed metallic Ni species.

Irrespective of the specific assignment, CO adsorption clearly indicates the presence of cationic Ni sites on the surface after reduction at 1000 °C. Only at very high Ni concentrations (50 mol%) a metallic Ni surface is available that is characterized by the presence of isolated sites and aggregates. Lower concentrated Ni catalysts possess a mainly oxidic surface plus some isolated, dispersed metallic Ni sites.

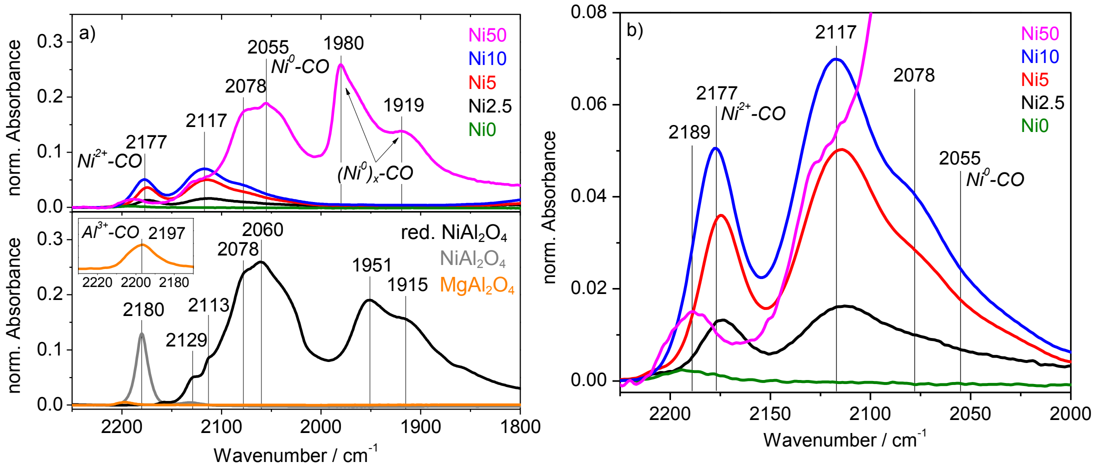

Figure 3.15 Transmission IR spectra recorded at -196 °C after adsorption of CO at 20 mbar and subsequent evacuation for 15 min of Ni catalysts (a top) and of reference samples (a bottom). (b) shows the magnified area of the C≡O stretching region. The reduced catalysts (1000 °C, 5% H_2/Ar, 1h) were pretreated in 50 mbar of H_2 at 850 °C for 1 h. Spectra recorded before CO dosing were used as background. The spectra were normalized to the mass per unit area of the wafer.

3.2.3.1.3 CO adsorption at 30 °C

The quantification of CO adsorption sites was determined by microcalorimetry through the adsorption of CO over Ni50-600-1000, Ni5-600-1000 and Ni0-600-1000 at 30 °C. In Figure 3.16 the differential heat of CO adsorption on Ni0, Ni5 (a) and Ni50 (b), is presented as a function of adsorbed CO molecules. The three catalysts exhibit very different surface sites at -196 °C as was shown by IR spectroscopy of adsorbed CO in Figure 3.15.

An initial differential heat of CO adsorption on the Ni free catalyst (Ni0) of 40 kJ mol^{-1} is obtained, which is typical for physisorption. Since CO does not chemisorb on the pure Mg,Al oxide matrix at 30 °C, the differential heat profiles of Ni5 and Ni50 are dominated by the presence of nickel.

CO adsorption on the freshly reduced Ni50 and Ni5 catalysts exhibit abnormally high differential heats of ~270 kJ mol^{-1} at low CO coverages. The CO adsorption heat on Ni (100), however, was reported to be 123 → 99 kJ mol^{-1} (at $\theta_{CO} = 0.1 \rightarrow 1$) [40]. This observation indicates that the strong adsorption involves reactions on the surface, which might be Ni catalyzed oxidation reactions of CO with the oxidic matrix. This is also indicated by the fact that the amount of adsorbed CO in this energetic regime (region I) is by a factor of two larger for the catalyst with less Ni (Ni5) and, therefore, a higher MgO content in the oxidic matrix. In region II the heats of adsorption gradually decrease with increasing surface coverage, representative for heterogeneous adsorption sites. A plateau-like state is reached at ~100 kJ mol^{-1}, typical for CO chemisorption on Ni (100) at full coverage. The plateau is more pronounced for the Ni5 catalyst. In region III values below 60 kJ mol^{-1} are reached, characteristic for physisorption. The energetic distribution of the adsorption sites is similar in both fresh samples. The adsorption isotherms of the two samples as a function of CO equilibrium pressure are plotted in Figure 3.16 (c) and (d). Ni50 exhibits a total CO capacity of ~2 µmol g$^{-1}_{cat}$ at monolayer coverage (~0.02 mbar). Ni5 in contrast exhibits ~6 µmol g$^{-1}_{cat}$ at monolayer coverage (~0.02 mbar).

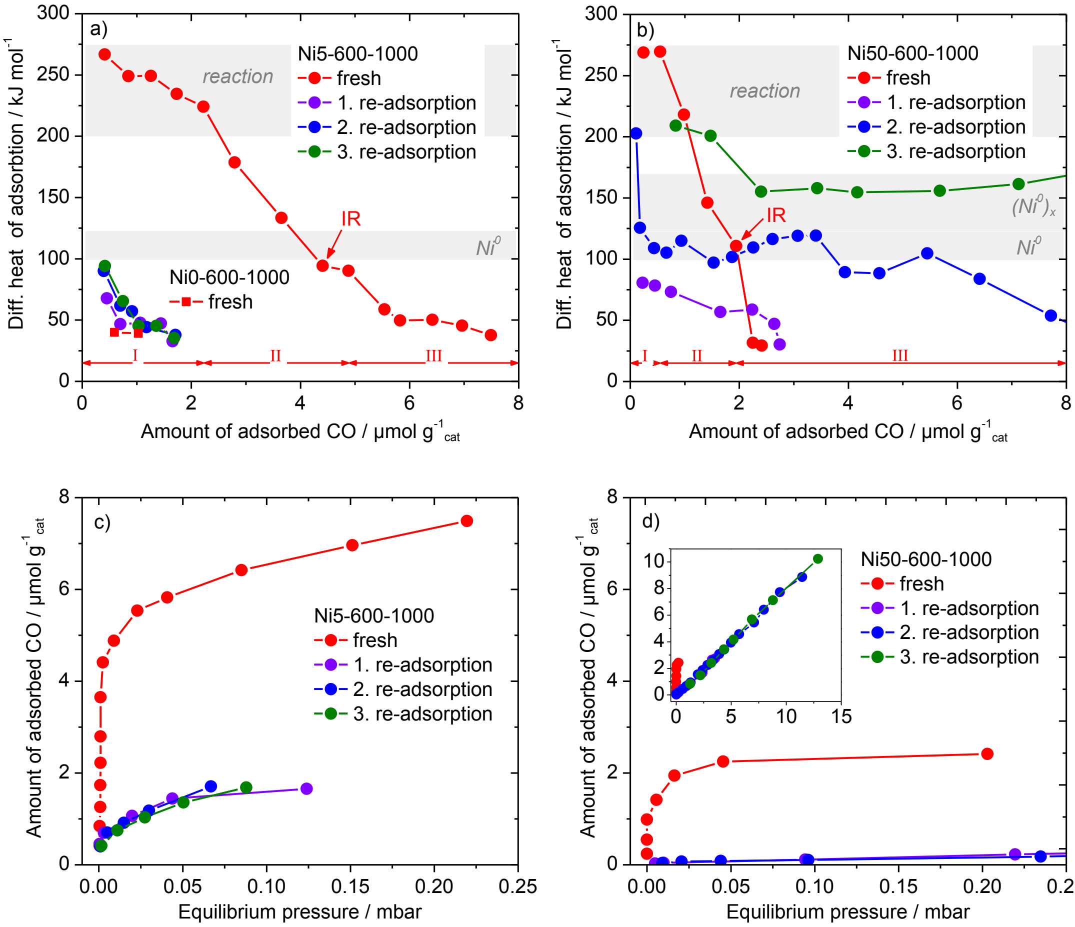

Figure 3.16 CO adsorption studied by microcalorimetry at 30 °C. Differential heats of adsorption as a function of the amount of adsorbed CO of Ni5-600-1000 and Ni0-600-1000 (a) and of Ni50-600-1000 (b). Re-adsorption profiles were each measured after evacuation at 30 °C. Marked data points refer to complementary IR spectra shown in Figure 3.17. The grey bars mark heat ranges of CO adsorption on different Ni sites. Adsorption isotherms of CO over Ni5-600-1000 (c) and Ni50-600-1000 (d) at 30 °C are shown below. The inset shows the complete adsorption isotherms during re-adsorption.

To study the influence of CO on the surface sites isothermal adsorption-desorption cycles were performed (Figure 3.16). Therefore, the samples were evacuated up to 10^{-8} mbar after the adsorption process. The initial differential heat of adsorption, as well as the number of adsorption sites of Ni5 is strongly reduced during the second cycle. Apparently, irreversible surface reactions occur, which contribute substantially to the heat signal measured during the first CO adsorption. This process might result in the formation of stable carbonyl species, blocking most surface Ni sites. Further adsorption-desorption cycles cause no further change. Before the physisorption regime (~40 kJ mol^{-1}) is reached, initial heats of re-adsorption of 65 to 95 kJ mol^{-1} were measured up to ∼1 µmol g^{-1}_{cat} CO coverage. Such heats could be ascribed to adsorbed CO over oxidized Ni species as suggested by Cerro-Alarcó et al. [41], taking into account that heats of adsorption on electron deficient metal sites are expected to be lower than those of metallic Ni. The presence of predominant Ni^{x+} species in this sample was identified by the IR measurements applied at -196 °C (see Figure 3.15). Nevertheless, IR spectra of CO adsorbed at 30 °C revealed no bands above 2100 cm^{-1} that are arising from cationic species (Figure 3.17). Hence, the interaction of CO with oxidized Ni is too weak at 30°C.

Similar to Ni5, the initial differential heat of adsorption of Ni50 is considerably reduced during the 2nd cycle. Although, the adsorption isotherm reveals, that surface saturation is not reached any more. Further adsorption-desorption cycles cause drastic change of the heat profiles and reveals the adsorption to be partially irreversible. Heats of adsorption of 100 to 200 kJ mol^{-1} were measured during the 3rd and 4th cycle. These values correlate with reported adsorption heats of bridged CO on Ni (100) of $\approx 170 \rightarrow 100$ kJ mol^{-1} (at $\theta_{CO} \approx 0 \rightarrow 1$) [42]. It can be concluded, that through the interaction with CO metallic Ni sites are regenerated and more Ni aggregates are formed. This behavior evidences a highly dynamic surface, which is likely to affect the activity and/or deactivation of a catalyst.

Based on the results derived from the differential heats of adsorption different dynamics and different quantities of surface sites have been identified for the two investigated catalysts. Both catalysts have a marked heterogeneity in the energetic distribution of adsorption sites. The Ni5 catalyst provides a higher amount of adsorption sites for CO. Thus no direct correlation of CO adsorption capacity with the Ni content is observed. While the CO adsorption on Ni5 is irreversible and remains static after the first adsorption, the mobile character of the Ni based adsorption sites in the Ni50 catalyst results probably from the generation/regeneration of metallic Ni sites.

In situ IR spectroscopy of CO adsorption were employed complementary at the same temperature (30 °C) to obtain information about the nature of the surface species involved in the adsorption processes on the catalyst surface (Figure 3.17). The equilibrium pressure of CO was adjusted to match the marked data points in the microcalorimetry measurements in Figure 3.16 a and b. Only metallic Ni species are visible, while cationic adsorption sites (>2100 cm^{-1}) are not active at 30 °C. Metal carbonyls (e.g. $Ni(CO)_4$ at 2130 cm^{-1}) were not detected. The IR spectra of the reduced Ni5 and Ni50 catalysts revealed a single intense band at 2042 cm^{-1} attributed to linearly bonded CO, and two other bands between 1900 and 2000 cm^{-1} attributed to bridged sites. The band intensity, however, is about ten times higher for Ni50.

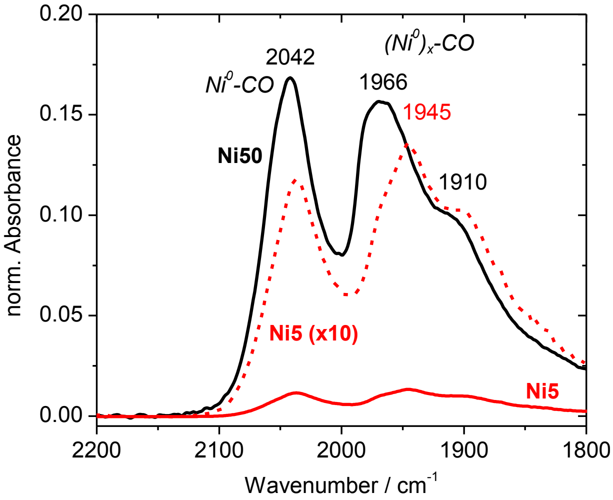

Figure 3.17 Transmission IR spectra of CO adsorbed at 30 °C on Ni5-600-1000 (a) and Ni50-600-1000 (b) catalysts in the $(Ni^0)_x$-CO region. The spectra refer to complementary data points measures by microcalorimetry shown in Figure 3.16 (arrow).

In summary, a series of Ni/MgAl oxide catalysts have been prepared and characterized. They consist of Ni nanoparticles that are formed during thermal treatment in hydrogen of NiMgAl mixed oxides obtained from htl precursors. No significant differences in particle size and shape as a function of the Ni content, except for the catalyst with the highest Ni content (50 mol%). The sample with a Ni content of 5 mol% exhibits the highest dispersion. HR-TEM images reveal the existence of an overgrowth on top of the Ni particles. The overgrowth might be interpreted as a nickel aluminate. CO adsorption at -196 °C clearly indicates that at very high Ni concentrations (50 mol%) the surface is characterized by isolated as well as aggregated metallic Ni sites. Lower concentrated Ni catalysts exhibit a predominantly oxidic surface and additionally some isolated metallic Ni sites. At 30 °C, where cationic adsorption sites are not stable, different dynamics and different quantities of surface sites have been identified for the Ni5 and Ni50 catalysts by microcalorimetry. Despite a similar energetic distribution of adsorption sites, the Ni5 catalyst provides a higher

CO adsorption capacity. Furthermore, Ni50 shows a pronounced surface dynamic resulting in the generation/regeneration of metallic Ni sites.

3.3 Catalytic properties

3.3.1 Dry reforming of methane

The catalytic activities of the reduced Ni-based catalysts derived from htl precursors in DRM are summarized in Table 3.3. The degree of methane conversion is given after 1 and after 10 hours under isothermal conditions at an oven temperature of 900 °C with a CO_2/CH_4 ratio of 1.25 at atmospheric pressure. The excess of CO_2 is chosen to reduce coke formation. According to Gadalla et al. [43] the temperature limit for carbon deposition increases as the CO_2/CH_4 feed ratio decreases. The catalysts were pretreated in 4% H_2/Ar at the corresponding reduction temperature (Table 3.3) and purged with Ar. The degree of methane conversion is increasing during 10 h of DRM for almost all investigated catalysts. No deactivation was observed under the measured conditions (CH_4 conversion over time on stream of Ni5-600-1000 is given in the SI, Figure S3.9). Even at these high degrees of methane conversion the equilibrium conversion (Ni50-600-1000: 1 bar, $T_{catalyst}$= 735 °C: 93 %, T_{oven}= 900 °C: 100 %) was not reached.

Table 3.3 Catalytic test results for the Ni/MgAl oxide catalysts for the dry reforming of methane at 900 °C and characteristics of spent catalysts.

Sample label	Ni Metal sites[a] / µmol g_{cat}^{-1}	$X_{CH_4,1h}$ / %	$X_{CH_4,10h}$ / %	D1/G band ratio[b]	CO_x formation[c] / mmol g_{cat}^{-1}
Ni50-600-1000	154	74	73	1.18	35
Ni15-600-1000	108	60	68	n.d.	13
Ni10-600-1000	81	52	61	n.d.	5
Ni7.5-600-1000	69	45	59	n.d.	6
Ni5-600-1000	77	35	50	1.59	6
Ni2.5-600-1000	16	18	46	n.d.	4
Ni1-600-1000	2	1	3	2.15	4
Ni0-600-900	0	0	0	3.17	19

[a] determined by H_2 pulse chemisorption, [b] determined by Raman spectroscopy, [c] measured by TPO: total CO_2 and CO formation

Figure 3.18a demonstrates that the CH_4 conversion rate correlates with the Ni content with a strong increase up to 15% and a much lower further increase until 50%. The sample with the highest Ni surface area shows also the highest integral specific rate of methane conversion (Figure 3.18b). From this observation it can be concluded that free Ni sites are responsible for the DRM activity, but the relationship is not linear. The structural differences on the surface of the reduced samples already mentioned in paragraph 3.2.3.1 might explain the differences in catalytic activity. Structure sensitivity is well known for the DRM [44].

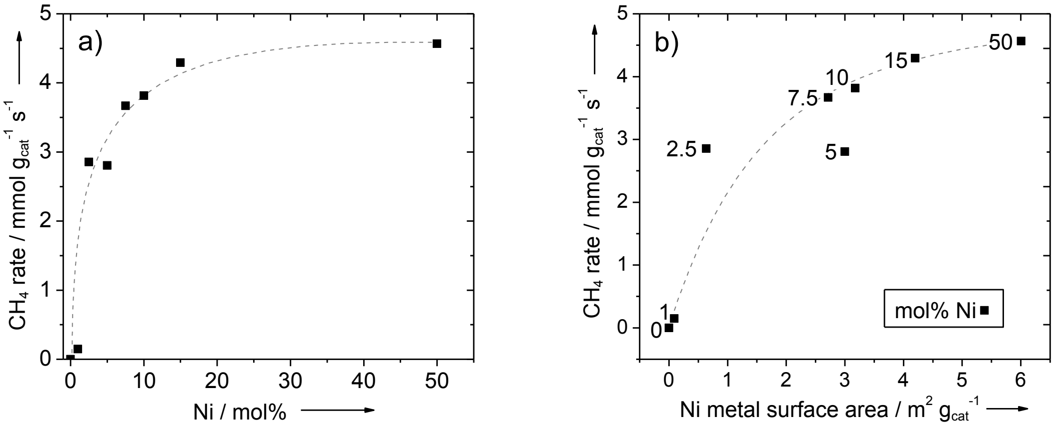

Figure 3.18 Integral specific rate of methane conversion as a function of Ni content at 900 °C after reduction at 1000 °C (a); correlation of the Ni surface area with the methane conversion rate (b) (lines are only guidelines for the eye).

3.3.2 Coking behavior

Despite the stable performance, electron microscopy investigations of the spent samples after 10 h in DRM at 900 °C revealed the presence of coke depositions on all tested catalysts (Figure 3.19). The carbon species were found to depend on the Ni content. At least three different types of carbon were identified: carbon nanofibers (CNFs), graphitic layers with and without inclusions of Ni particles and less ordered carbon. For catalysts with higher Ni contents (50 and 25 mol%) a slight sintering of the Ni nanoparticles and the formation of mainly CNFs as well as graphitic carbon are observed. Whereas on the catalyst with 5 mol% Ni purely graphitic carbon which is encapsulating the Ni particles is formed (Figure 3.19e). In contrast to the other samples the microstructure is nearly preserved during reaction and sintering of the nanoparticles cannot be observed for this catalyst. The TEM analysis of the Ni-free catalyst revealed the presence of mainly less ordered carbon (Figure 3.19f). As this catalyst has not shown any detectable CH_4 conversion in the DRM test (Table 3.3), these deposits might have been formed partially already during the reductive pretreatment. This was suggested by the TPR-MS measurements in section 3.2.2. Furthermore, after 10 hours on stream and a very low conversion of CH_4, carbon depositions by CH_4 pyrolysis could occur.

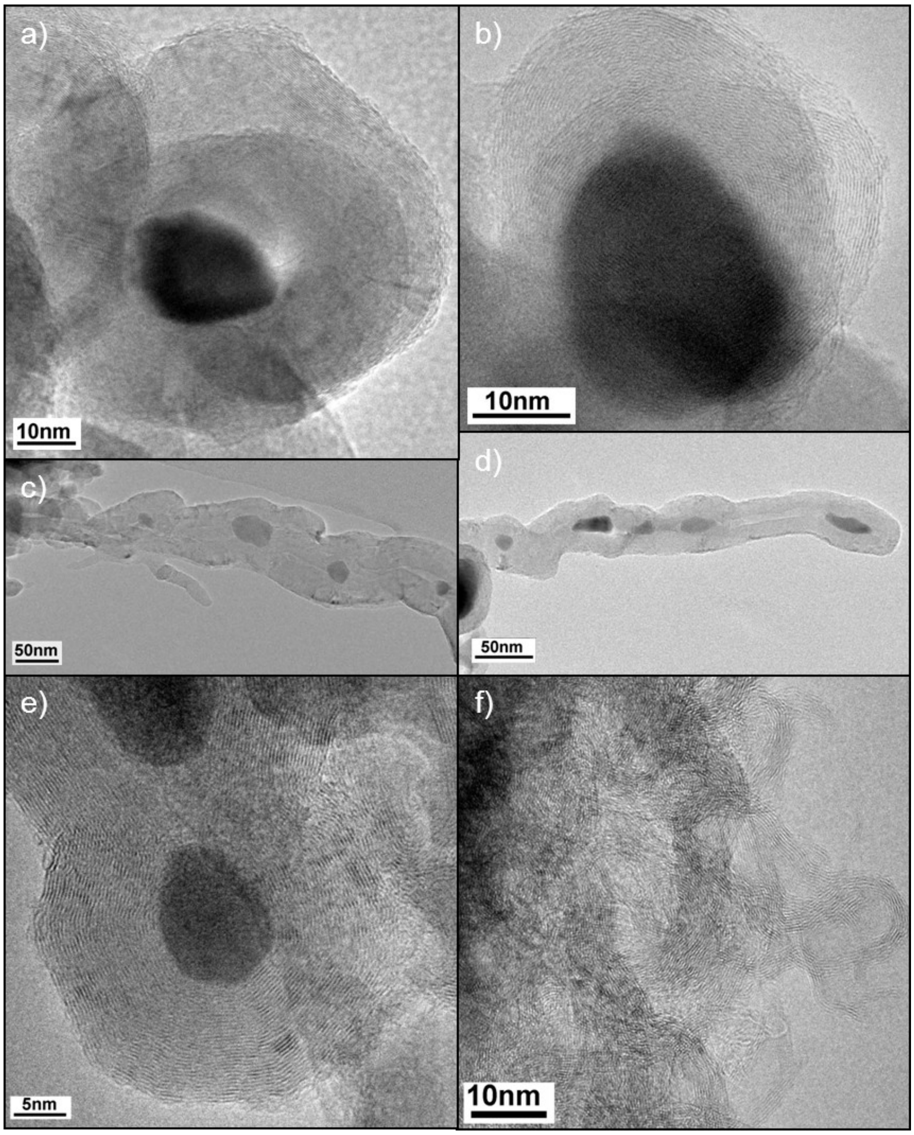

Figure 3.19 TEM micrographs of spent samples after 10 h DRM at 900 °C of 50 mol% Ni with Ni particle surrounded by graphitic carbon (a) and with CNF (c), 25 mol% Ni with graphitic carbon layer (b) and with CNF (d), 5 mol% Ni with Ni particles surrounded by graphitic carbon (e) and 0 mol% Ni with less ordered graphitic carbon (f).

For further structural information of the carbonaceous depositions Raman spectroscopy has been applied to the spent samples. Since Raman signals are very sensitive to the degree of structural disorder it is possible to gain information about the degree of graphitization. The spectra of the spent catalysts exhibit five first-order bands, the G (“graphite”) and the D1 to D4 (“defect”) bands. The deconvolution of the bands was performed according to Sadezky et al. [45]. Although CNFs contribute to the G band intensity too, the ratio is used here as a measure for the graphitic carbon content. A lower D1 to G band intensity (peak area) ratio, I_{D1}/I_G indicates a higher fraction of graphitic carbon (Table 3.3). In agreement with the TEM results, Raman spectra that have been taken of the spent samples after DRM at 900 °C revealed a lower graphitic content with lower Ni contents (Figure 3.20). These results support the assumption that the carbon formation mechanism is influenced by the catalyst composition.

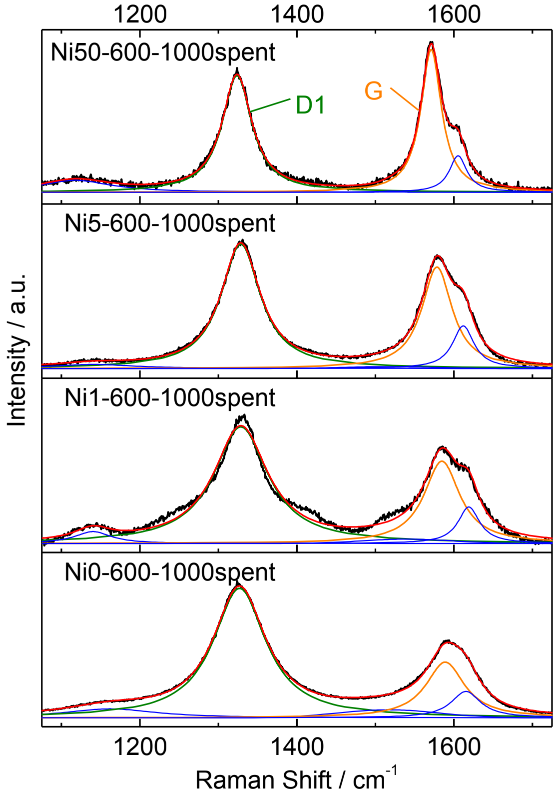

Figure 3.20 Fitted Raman spectra (633 nm) of spent catalysts after 10 h DRM at 900 °C.

To further examine the nature of surface carbon species on the catalysts, in situ TPO experiments have been performed subsequent to the DRM activity tests in a fixed-bed reactor. The TPO profiles are shown in Figure 3.21, where coke depositions are oxidized by O_2 to CO_2 and CO. Generally, various forms of carbon are different in terms of reactivity. Therefore, different peak numbers and positions for the various Ni contents point to the formation of diverse carbon species, in agreement with the TEM results (Figure 3.19). On the catalysts with 50, 15 and 10 mol% Ni the appearance of three peaks in the TPO profile suggests that there are at least three kinds of carbon species present. The peaks of Ni50 are centered at 600 °C, 690 °C and at 775 °C. Düdder et al. [22] performed TPO experiments of carbonaceous reference materials. Referring to these results, we assign the low temperature peak around 600 °C to carbon filaments, whereas the high temperature peak around 775 °C fits well with the oxidation of high surface area graphite (HSAG). Only less ordered carbon was found by TEM in the Ni free sample. Therefore, the peak at 680 °C is assigned to the decomposition of less ordered carbon. The catalysts with 2.5 and 5 mol% Ni generate only graphitic carbon which is also in accordance with the TEM results. Both the catalyst with 1 mol% Ni and the Ni free sample show the presence of two carbon species each, having a minor contribution of graphitic carbon around 740 °C in common. Whereas the origin of the peak at 650 °C in the Ni1 sample could not precisely be assigned, the peak at 680 °C in the Ni-free sample is attributed to less ordered carbon.

When operated over an active catalyst a strong heat consumption during the highly endothermic DRM reaction leads to a much lower effective bed temperature (735 °C for Ni50-600-800 at T_{oven} = 900 °C). Accordingly, the bed temperature is much higher in the absence of nickel. Based on thermodynamics the carbon formation due to the exothermic Boudouard reaction is negligible at temperatures higher than 720 °C [22]. Hence, we can conclude that the origin for carbon formation on the Ni-free sample is gas phase pyrolysis of methane. Additionally, the Ni free sample showed the formation of CO at the same peak position as CO_2 due to an incomplete combustion during TPO after DRM. It is a known phenomenon for carbon species to form CO upon TPO in absence of a catalyst [46]. Thus, it is likely, that Ni (or NiO) works as a catalyst for the oxidation of carbon species to CO_2.

Although the formation of filamentous carbon might only minor influences the activity, but they can destroy the catalyst particles and block the reactor [6]. Combined with the TEM observations of the spent catalysts, it can be concluded that the formation of filamentous carbon is greatly inhibited for the samples with Ni contents of ≤ 10 mol%.

Since, in the TPO experiments the coke depositions are oxidized with O_2 to CO_2 and CO, the total amount of CO_x formed, is a measure for the amount of carbon which was deposited during the reaction. An almost linear correlation between the Ni content and the CO_x formation, i.e. amount of deposited carbon, can be observed. Only the sample without Ni is not following this trend, but has a higher carbon amount deposited than the Ni15 catalyst. The Ni-free material probably follows a different mechanism (Figure 3.22a). Between 10 and 1 mol% Ni the carbon formation reaches a kind of plateau, where the amount of carbon formed is nearly constant. A minimum in carbon formation was found on the catalyst with 2.5 mol% Ni, resulting from mainly graphitic carbon. A volcano type correlation of the Ni dispersion and the CO_x formation is revealed (Figure 3.22b), with a maximum at 5 mol% Ni.

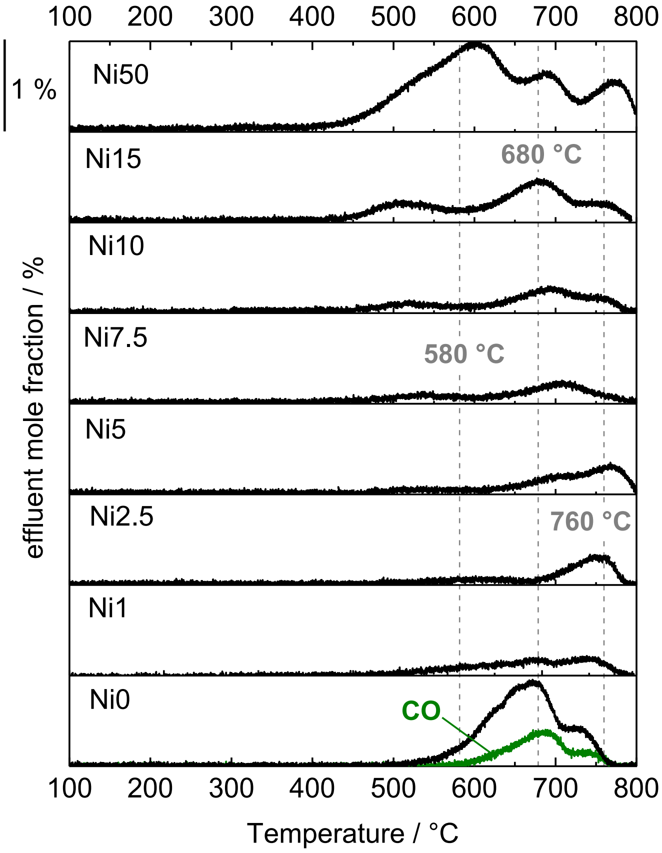

Figure 3.21 TPO profiles of catalysts after 10 h of DRM at 900 °C. Effluent mole fraction of CO_2 (and CO, green) were detected while heating with 5 K min^{-1} in 4.5% O_2/Ar.

The coking ability can be related to the observed formation of an overgrowth after reduction. For the samples that are least coking, an almost complete overlayer was detected (TEM) and only a small number of isolated metallic Ni centers (IR). The sample (Ni50) that forms the most carbon, however, exhibit an incomplete overgrowth (TEM) and predominantly large agglomerates of metallic Ni sites (IR) on the surface. The observed dynamic behavior of Ni50 during CO adsorption-desorption cycles might also relate to the enhanced coking ability.

Several studies investigating the structure sensitivity of carbon formation on Ni catalysts have been carried out before. Previous DFT calculations by Bengaard et al. [47] presented a comprehensive mechanistic picture of the steam reforming process and the graphite formation on a Ni catalyst. Due to lower activation barriers carbon is stronger bound on the step sites. Accordingly, step sites are also suggested to be the nucleation sites of graphite. Blocking of the step sites by using adequate promoters, therefore, leads to suppression of graphite formation. It is also stated that a critical cluster size of ~25 Å for graphene islands growing out on the Ni facets from step sites is needed for graphite formation. Nucleation cannot proceed on particles with smaller facets than this. Therefore, very small, multifaceted particles do not grow graphite. Recently, Rinaldi et al. [48] studied the carbon growth on Ni particles supported on carbon nanofibers (CNFs) and the influence of carbide formation. Surface sensitive techniques were employed to show that carbon grows from a carbide layer on top of metallic nickel particles. Carbon incorporation into metallic Ni particles was discovered as the initial stage of Ni carbide formation. Thus, the ability to form carbon requires a free Ni metal surface.

Based on our experimental results and previous observations we conclude that coking needs a large, free metallic Ni surface to incorporate carbon and grow graphene islands [47,48] and step sites as active centers for nucleation [47]. Our results have shown that covering the metallic Ni surface with oxide species due to MMSI and thus the variation of available metallic surface is an interesting alternative to size reduction and to mitigate coking during DRM.

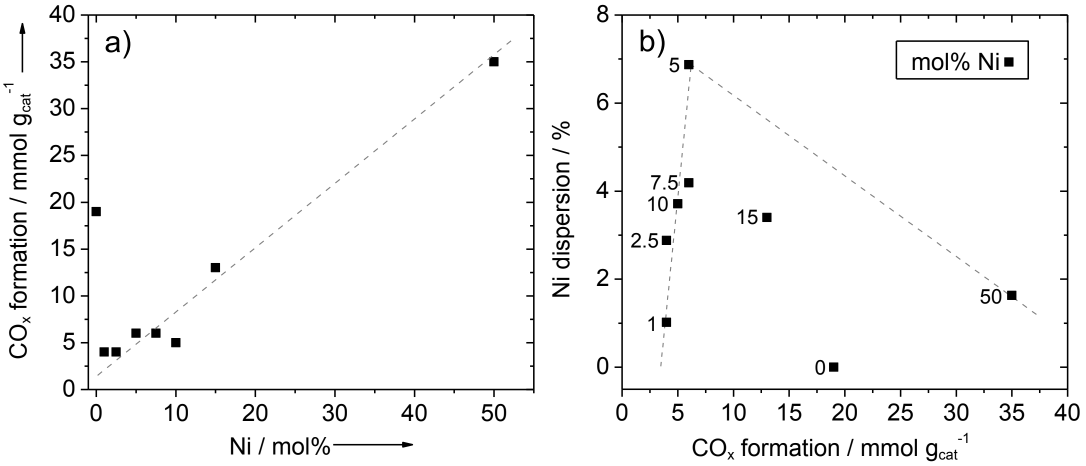

Figure 3.22 CO$_x$ formation during subsequent TPO measurements per mol Ni (a), correlation between Ni dispersion determined by H_2 chemisorption and CO$_x$ formation during subsequent TPO measurements (b) (lines are only guidelines for the eye).

Additional to the results obtained in the tubular fixed-bed reactor, the effect of catalyst composition on the coking kinetics during DRM at 900 °C has been explored *in situ* in a magnetic suspension thermobalance with a vertical geometry (Figure 3.23). It is noted that due to the large amount of catalyst and the non-ideal flow conditions in this experiment, no reliable catalytic data on activity and stability can be obtained, but the coking behavior can be directly measured by monitoring the changes in the sample weight. Also an exact measurement of the temperature directly within the catalyst bed was not possible and when comparing the temperatures recorded in this experiment with those of the catalytic tests great care must be taken. Exemplary three samples were investigated after reduction at 1000 °C.

The catalyst with the highest Ni content (50 mol%), with 15 mol% and with 5 mol%, as a representative for the least-coking regime, were investigated. A higher Ni loading resulted in a higher degree of coke formation (Figure 3.23a). This is in general agreement with the observations made by TPO in the fixed-bed reactor.

For the catalyst with 5 mol% Ni no weight gain was observed. The Ni15 catalyst resulted in a slightly increased mass, while for the catalyst with a Ni content of 50 mol% an instantly continuous weight gain was observed due to carbon formation. The amount of carbon after 10 h adds up to 65 mmol g_{cat}^{-1} (Ni50) and 3 mmol g_{cat}^{-1} (Ni15). The formation rate of the carbon deposition was determined to 8.5 wt.-% h^{-1}. As no deactivation was observed over 10 h times on stream at 900°C in a fixed-bed reactor (Table 3.3), the continuous coke formation implies that deactivation of the Ni50 catalyst is probably not related to the total amount of carbonaceous deposits but rather to the type of carbon formed. Figure 3.23b demonstrates a higher CH_4 conversion rate for the higher loaded catalyst in agreement with the results in the fixed-bed reactor and a slight deactivation.

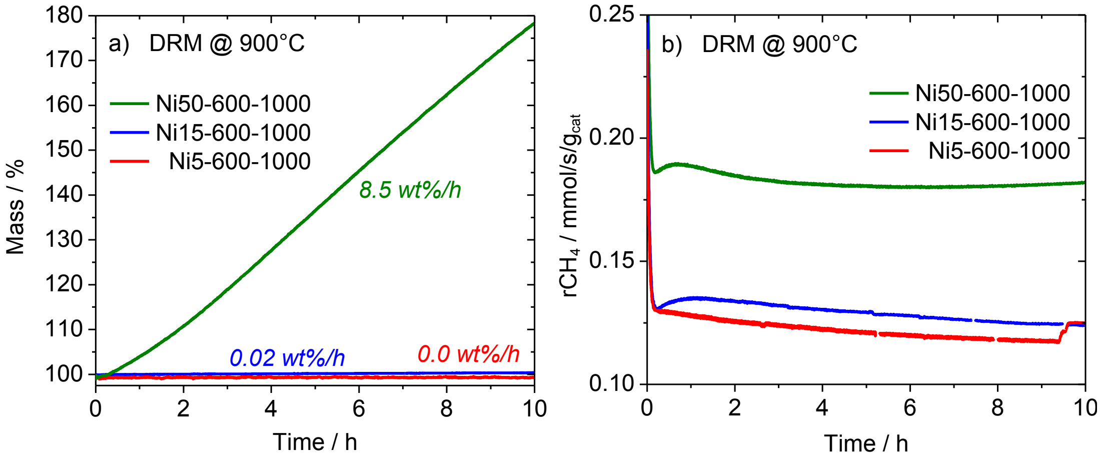

Figure 3.23 Thermogravimetric measurements under dry reforming conditions at 900 °C. The effect of varied catalyst composition on the catalyst weight increase as a measure of carbon formation rate (a) and CH_4 conversion rate (b) are shown.

3.4 Conclusion

A series of non-precious metal catalysts has been synthesized by constant pH co-precipitation with Ni contents between 0 and 55 wt%. The resulting Ni/MgAl oxide catalysts exhibit average spherical Ni particle sizes between 7 and 20 nm after a thermal treatment at 1000 °C. By the employment of surface sensitive techniques (HR-TEM and IR), we were able to show that an oxidic overgrowth is formed on the Ni particles. The overgrowth might be interpreted as a nickel aluminate formed due to medium metal support interaction. At very high Ni concentrations (50 mol%) the particles are only partially covered. CO adsorption clearly indicates that in this case the surface is characterized by very dynamic aggregated metallic Ni sites. In lower concentrated catalysts the particles show a complete coverage. The surface exhibits a predominantly oxidic surface and additionally some isolated metallic Ni sites.

The effect of different catalyst compositions on the catalytic performance was studied in the dry reforming (DRM) reaction. The catalysts showed increasing integral rates of methane conversion with increasing Ni content and increasing metal surface area. Although all catalysts have shown minor carbon formation, their performance was stable over the investigated 10 h of DRM. We have shown that DRM features the formation of CNFs, graphitic and less ordered carbon. The amount as well as the type of carbon is influenced by the Ni content in the catalyst composition. Between 10 and 1 mol% Ni the lowest amount of carbon is formed.

The observed surface properties of the Ni based catalysts were used to propose structure-performance-relationships. We suggest that the overgrowth is the main reason for the suppression of carbon formation observed for certain catalysts. The overgrowth blocks all extended metallic Ni sites that are nucleation centers for carbon formation. However many isolated sites need to be present in order to preserve the DRM activity. If the surface, however, is only partially covered and the free metallic Ni surface is large enough to grow graphene islands the carbon formation is promoted.

Accordingly, the formation of an overgrowth by an adapted catalyst synthesis is desirable. In an optimized catalyst the overgrowth will cover just enough of the metallic Ni surface that carbon formation is effectively blocked while the reaction can still proceed on the isolated sites.

3.5 Experimental Section

3.5.1 Synthesis conditions

The catalysts were prepared from hydrotalcite-like (htl) precursors with the general formula $Ni_xMg_{0.67-x}Al_{0.33}(OH)_2(CO_3)_{0.17} \cdot mH_2O$ by constant pH co-precipitation. The precipitation took place in an automated laboratory reactor (Mettler-Toledo Labmax) at T=50 °C from aqueous 0.6 M NaOH, 0.09 M Na_2CO_3 solution and 0.4 M aqueous metal nitrate solution at pH 8.5. The nitrate solution and the precipitating agent were added simultaneously to keep the pH value constant. The precipitates were aged for 0.5 h in the mother liquor, filtrated, thoroughly washed with water until the conductivity of the filtrate was < 0.5 mS cm^{-1} and dried at 100 °C over night. The obtained precursors were calcined in air at 600 °C for 3 h. An exemplary protocol of the precipitation process of the precursor with 50 mol% at 50 °C can be found in the supporting information (SI, Figure S3.1). The amount of nickel was varied between 0 - 50 mol%, i.e. $0 \leq x \leq 0.5$ (Ni-loadings ranging from 0 - 55 wt% in the final catalyst). The molar (Ni,Mg):Al ratio was fixed at 67:33. Nine precursor samples were prepared with 0, 1, 2.5, 5, 7.5, 10, 15, 25, and 50 mol% Ni.

The precursor samples are labeled NiX, X being the nominal molar Ni content Ni:(Mg+Al) in %. The calcined samples are labeled NiX-T_{calc}, T_{calc} being the calcination temperature in °C. The reduced samples are labeled NiX-T_{calc}-T_{red}, T_{red} being the reduction temperature in °C. For example, the reduced sample with 50% Ni after calcination at 600 °C and reduction at 800 °C is denoted as Ni50-600-800.

3.5.2 Characterization

Powder X-ray diffraction (XRD) measurements were performed using a Bruker D8 Advance reflection diffractometer equipped with a Lynx-Eye energy discriminating position sensitive detector (1D-PSD) using CuKα1 radiation. Kβ radiation was suppressed with a Ni-filter.

Specific surface areas of the calcined material and the precursors were carried out by N_2 physisorption (Quantachrome Autosorb-6) and evaluated using the BET method. The samples were outgassed for 4 h at 80°C. Pore size distributions were determined from the desorption branches of the isotherms using the BJH method.

Thermogravimetric analysis (TG) and evolved gas analysis (EGA) of the decomposition reaction were achieved by using a NETZSCH STA449 thermoanalyzer under controlled gas flow (21 % O_2 in Ar, 100 Nml min^{-1}) connected to a quadrupole mass spectrometer (QMS200 OMNISTAR, Balzers). The measurements were performed with approximately 15 mg sample in a temperature range of 30-1000 °C (2 K min^{-1}).

Temperature-programmed reduction (TPR) of the samples was performed in a fixed-bed reactor (TPDRO-1100, CE Instruments) in 5 % H_2/Ar (60 Nml min^{-1}), with a heating rate of 6 K min^{-1}, in a quartz tube. According to Monti and Baiker [49] the sample mass was varied to gain equivalent amounts of NiO (10 mg) and signals of comparable peak areas. The H_2 consumption was monitored with a thermal conductivity detector (TCD). The TCD detector was calibrated by reducing a known amount of CuO.

The X-ray absorption near-edge structure spectra (NEXAFS) were measured at the ISISS beamline at the BESSY II synchrotron facility of the Helmholtz-Zentrum Berlin (Germany). The beamline was operated with 60 μm exit slit. For the detection of the Ni L-edges an energy region of 840–880 eV were measured, for the Al K-edge of 1550-1590 eV and for the Mg K-edge of 1295-1340 eV. The measurements were performed in vacuum at room temperature. The reduced samples were measured without prior air contact. For the measurement the samples were pressed to pellets. The Athena 0.8.056 software package was used for data evaluation.

To determine the nickel metal surface area, a H_2 pulse chemisorption method was applied. Therefore the samples were reduced in 5% H_2/Ar (80 Nml min^{-1}), with a heating rate of 6 K min^{-1} in a fixed-bed reactor. After cooling down to 50 °C in Ar, a defined volume of H_2 gas (100 %) is introduced by pulse-dosing with a volume of 250 µl. The pulses were continued until no further uptake was detected. The Ni metal surface area was determined assuming a dissociative chemisorption mechanism of hydrogen (Sf= 2; 2Ni/H_2) [50]. The amount of H_2 gas adsorbed per gram catalyst (V_m) was used to determine the Ni dispersion (D_{Ni}).

$$D_{Ni} = Vm \cdot M_{Ni} \cdot Sf / \text{wt.-\%}$$

The interface ratio (IFR) is the part of the particle that is in contact with the support phase and therefore not accessible for reactive gases. It can be calculated as the ratio between a theoretical surface area (SA_{theo}), calculated from the particle size that is determined by TEM, and the metal surface area (SA_{Ni}), determined by H_2 pulse chemisorption.

$$IFR = 1-(SA_{Ni} / SA_{theo}),$$

where SA_{theo} is calculated from the surface area (A_{Ni}) and the spherical particle volume (V_{Ni}) and the density of Ni (ρ_{Ni} = 8.90 g cm^{-3}):

$$SA_{theo} = A_{Ni} \cdot \text{wt.-\%} / \rho_{Ni} \cdot V_{Ni}$$

Infrared spectroscopy (IR) was employed to characterize the catalysts surface. The IR experiments were carried out in transmission mode using a Perkin-Elmer 100 FTIR spectrometer equipped with an in situ cell, allowing thermal treatments in controlled atmosphere, cooled with liquid nitrogen. A spectrum of the empty cell at -196 °C served as background for the measurements. After pre-reduction at 1000 °C (6 Kpm) in 5% H_2/Ar for 1 h, self-supporting wafers of the samples were prepared. Subsequently, the catalysts were re-reduced in the IR cell at 850 °C (10 Kpm) in 50 mbar H_2 for 1 h and evacuated at 25 °C. CO was adsorbed at -196 °C progressively (p_{CO}= 0-20 mbar). Stepwise desorption followed. For improved comparison of the peak intensities, the spectra have been normalized with respect to the mass per unit area. The reference spinels were pretreated in the IR cell at 850 °C (10 Kpm) in 200 mbar O_2 for 1 h. After CO adsorption and desorption, the $NiAl_2O_4$ was reduced in the IR cell at 850 °C in 50 mbar H_2 for 1 h, to prepare the reduced $NiAl_2O_4$ sample.

Microcalorimetry experiments were performed using a SETRAM MS70 Calvet calorimeter. The samples were pre-reduced *ex situ* at 1000 °C (6Kpm) in 5% H_2/Ar for 1 h. CO was adsorbed progressively at 30 °C after re-reduction of the catalysts in the calorimeter in 50 mbar H_2 at 450 °C (10 Kpm) for 5 h and subsequent evacuation up to 10^{-8} mbar at 30 °C. Subsequently, another adsorption cycle was performed under identical conditions in order to evaluate the reversibility of the adsorbed CO molecules. The adsorption-desorption procedure was repeated three times. IR measurements of CO adsorption were performed complementary to the microcalorimetry experiments at 30 °C using the same dosing steps.

For morphological studies of the materials, SEM images were acquired with a Hitachi S-4800 scanning electron microscope equipped with a field emission gun. The samples were loosely dispersed on conductive carbon tape (Plano). The SEM was operated at low accelerating voltage (1.5 kV) for a better resolution of the surface features of the samples. Elemental analysis by using X-ray energy dispersive spectroscopy (EDX) was carried out at 15 kV using an EDAX detector connected to the SEM.

For the determination of the particle- size distribution, images were taken with a Philips CM200 transmission electron microscope (TEM) equipped with a LaB_6 cathode or a field electron gun. The samples were dispersed in chloroform and deposited on a holey carbon film supported on a copper grid. High-resolution images were taken with a CCD camera. Before the measurement the fresh samples were reduced and subsequent passivated by slow increase of oxygen partial pressure at room temperature. For the investigation of spent samples after DRM, the samples were reactivated after TPO by reduction and exposed to a second DRM run with the conditions described above. After cooling down the catalysts were taken out carefully and separated from the dilutant by sieving afterwards.

HR-TEM and HR-STEM images were recorded on a FEI Titan 80-300 equipped with a Cs corrector at 300 kV and a double corrected JEOL JEM-ARM200F equipped with a CEOS CESCOR and a CEOS CETCOR hexapole aberration correctors for probe and image forming lenses, respectively, and a cold field emission gun (CFEG). Prior to the TEM investigation, the samples were reduced at 1000 °C and transferred from the glove box to the microscope under inert atmosphere using a vacuum transfer holder (Gatan).

To characterize the carbon deposition that has been formed on the catalyst during DRM Raman spectroscopy was applied at room temperature. A LabRam spectrometer was used with a 633 nm laser excitation from a HeNe laser and a power of 20 mW at the laser output. All data were obtained with a BX40 Olympus microscope (objective 100). Acquisition times were typically 3 x 180 s. Prior to the experiments, the Raman spectrometer was calibrated using a Si wafer. D1/G band ratios were determined using the fitted band areas. The fitting was performed according to Sadezky et al. [45].

Thermogravimetric experiments for the investigation of coking behavior have been performed in a Rubotherm DynTHERM magnetic suspension thermobalance. Prior the experiment the catalysts were reduced with 5 K min^{-1} at 800 °C in 5% H_2/Ar. Upon reaching the desired reaction temperature the system was purged in Ar for 1 h. Afterwards the DRM was performed at 900 °C in 120 Nml min^{-1} 40% CO_2 / 32% CH_4 / Ar for 10h.

3.5.3 Catalytic performance

The catalytic experiments were performed in a continuous flow system at atmospheric pressure using a fixed-bed tubular quartz reactor of 8 mm inner diameter. The reactor was equipped with a ceramic tube in the radial center of the reactor to measure the temperature at the sample position. For steady-state measurements calibrated on-line GC analysis (Shimadzu 14-B) was used to analyze the product gas composition. For transient studies a coupled IR-detector (CO, CO_2 & CH_4) and a TCD for H_2 (Emerson MLT4 multi channel analyzer) and a paramagnetic O_2 detector (Magnos 16) were used.

For the catalytic test, 10 mg of the calcined catalyst (sieve fraction of 250 - 355 μm) was diluted with 490 mg of high purity SiC (sieve fraction of 125 - 180 μm). Initially, the catalyst was activated by reduction in 4% H_2/Ar (99,9% / 99,999%) and a total flow of 20 Nml min^{-1} with a linear heating rate of 5 °C min^{-1}. The final temperature of 1000 °C was held constant for 30 min. Subsequently, the catalyst was cooled to the specified reaction temperature in Ar (99,999%). The dry reforming reaction was carried out with a gas mixture consisting of CH_4 (99,9995%), CO_2 (99,9995%) and Ar in a ratio of 32:40:28. The total flow was set to 240 Nml min^{-1}. To ensure a CO_2/CH_4 ratio $\geq$ 1:25 at any time, the CH_4 partial pressure was increased stepwise while starting the experiment. The reaction was performed at constant furnace temperature with a reaction time of 10 h. The reaction was followed by a holding period of 10 min and cooling in Ar for 2.5 h. In case the sample was not ex-situ characterized by TEM directly after DRM, subsequent a TPO experiment was performed with flow rates of 20 Nml min^{-1} of 4.5% O_2/Ar (99,995% / 99,999%) and a linear heating rate of 5 °C min^{-1}. The final temperature of 800 °C was kept constant until no more O_2 consumption was observed. Compared to a previous publication that included some of the samples reported here [22], the results for this paper were re-measured with the full sample series at a different site leading to slightly deviating results.

The methane turnover frequencies (TOF) were calculated by the methane conversion rate divided by the number of metal sites which was determined by H_2 pulse chemisorption.

3.6 References

[1] F. Fischer, H. Tropsch, *Brennst.-Chem.* **1928**, 3, 39-46.

[2] K. P. de Jong (Ed.), *Synthesis of Solid Catalysts*. Wiley-VCF, Weinheim, **2009**.

[3] S. Wang, G. Q. Lu, G. J. Millar, *Energy Fuels* **1996**, 10, 896-904.

[4] A. T. Ashcroft, A. K. Cheetham, M. L. H. Green, P. D. F. Vernon, *Nature* **1991**, 352, 225-226.

[5] J. R. Rostrup-Nielsen, D. L. Trimm, *J. Catal.* **1977**, 48, 155-165.

[6] C.-j. Liu, J. Ye, J. Jiang, Y. Pan, *ChemCatChem* **2011**, 3, 529-541.

[7] M. Behrens, F. Studt, I. Kasatkin, S. Kühl, M. Hävecker, F. Abild-Pedersen, S. Zander, F. Girgsdies, P. Kurr, B.-L. Kniep, M. Tovar, R. W. Fischer, J. K. Nørskov, R. Schlögl, *Science* **2012**, 336, 893-897.

[8] D. Baudouin, U. Rodemerck, F. Krumeich, Ai. de Mallmann, K. C. Szeto, H. Ménard, L. Veyre, J.-P. Candy, P. B. Webb, C. Thieuleux, C. Copéret, *J. Catal.* **2013**, 297, 27-34.

[9] V. Y. Bychkov, Y. P. Tyulenin, A. A. Firsova, E. A. Shafranovsky, A. Y. Gorenberg, V. N. Korchak, *Appl. Catal., A* **2013**, 453, 71-79.

[10] G. J. Kim, D.-S. Cho, K.-H. Kim, J.-H. Kim, *Catal. Lett.* **1994**, 28 41-52.

[11] J.-H. Kim, D. J. Suh, T.-J. Park, K.-L. Kim, *Appl. Catal., A* **2000**, 197, 191-200.

[12] R. Martínez, E. Romero, C. Guimon, R. Bilbao, *Appl. Catal., A* **2004**, 274, 139-149.

[13] J. Juan-Juan, M. C. Román-Martínez, M. J. Illán-Gómez, *Appl. Catal., A* **2009**, 55, 27-32.

[14] D. Chen, K. O. Christensen, E. Ochoa-Fernández, Z. Yu, B. Tøtdal, N. Latorre, A. Monzón, A. Holmen, *J. Catal.* **2005**, 229, 82-96.

[15] K. Mette, S. Kühl, H. Düdder, K. Kähler, A. Tarasov, M. Muhler, M. Behrens, *ChemCatChem* **2014**, 6, 100-104.

[16] S. Kannan, *Catal. Surv. Asia* **2006**, 10, 117-137.

[17] F. Li, Feng; X. Duan. Applications of layered double hydroxides, in: X. Duan, D. G. Evans (Eds.), *Layered double hydroxides*, Springer Berlin, Heidelberg, **2006**, 193-223.

[18] Z. P. Xu, J. Zhang, M. O. Adebajo, H. Zhang, C. Zhou, *Appl. Clay Sci.* **2011**, 53 139-150.

[19] T. Shishido, M. Sukenobu, H. Morioka, R. Furukawa, H. Shirahase, K. Takehira, *Catal. Lett.* **2001**, 73, 21-26.

[20] A. I. Tsyganok, T. Tsunoda, S. Hamakawa, K. Suzuki, K. Takehira, T. Hayakawa, *J. Catal.* **2003**, 213, 191-203.

[21] O. W. Perez-Lopez, A. Senger, N. R. Marcilio, M. A. Lansarin, *Appl. Catal., A* **2006**, 303, 234-244.

[22] H. Düdder, K. Kähler, B. Krause, K. Mette, S. Kühl, M. Behrens, V. Scherer, M. Muhler, *Catal. Sci. Technol.* **2014**, 4, 3317-3328.

[23] F. Cavani, F. Trifirò, A. Vaccari, *Catal. Today* **1991**, 11, 173-301.

[24] V. Rives, *Layered double hydroxides: present and future*. Nova Science Publishers, New York, **2001**.

[25] D. G. Evans, R. C. T. Slade. Structural Aspects of Layered Double Hydroxides, in: X. Duan, D. G. Evans (Eds.), *Layered double hydroxides*, Springer Berlin, Heidelberg, **2006**, 1-87.

[26] C. Forano, T. Hibino, F. Leroux, C. Taviot-Guého. Layered Double Hydroxides, in: F. Bergaya, B. K. G. Theng, G. Lagaly (Eds.), *Handbook of Clay Science*, Elsevier, Amsterdam, **2006**, 1021-1094.

[27] L. B. McCusker, R. B. von Dreele, D. E. Cox, D. Louër, P. Scardi, *J. Appl. Cryst.* **1999**, 32, 36-50.

[28] J. I. Langford, D. Louër, *Rep. Prog. Phys.* **1996**, 59, 131-234.

[29] A. M. Becerra, A. E. Castro-Luna, *J. Chil. Chem. Soc.* **2005**, 50, 2, 465-469.

[30] P. Arnoldy, J. A. Moulijn, *J. Catal.* **1985**, 93, 38-54.

[31] B. Scheffer, P. Molhoek, J. A. Moulijn, *Appl. Catal.* **1989**, 46, 11-30.

[32] J. R. Rostrup-Nielsen, *Catalysis, Science and Technology*, (Eds: J. R. Anderson, M. Boudart), vol. 5, Springer, Berlin, **1984**, 1-117.

[33] M. Lo Jacono, M. Schiavello, A. Cimino, *J. Phys. Chem.* **1971**, 75, 1044-1050.

[34] J. R. H. Ross, M. C. F. Steel, A. Zeini-Isfahani, *J. Catal.* **1978**, 52, 280-290.

[35] A. Al-Ubaid, E. E. Wolf, *Appl. Catal.* **1988**, 40, 73-85.

[36] A. M. Ruppert, B. M. Weckhuysen, *Handbook of Heterogeneous Catalysis*, **2008**, 1178-1188.

[37] G. Poncelet, M. A. Centeno, R. Molina, *Appl. Catal., A* **2005**, 288, 232-242.

[38] F. Abild-Pedersen, M. P. Andersson, *Surf. Sci.* **2007**, 601, 1747-1753.

[39] G. Spoto, E. N. Gribov, G. Ricchiardi, A. Damin, D. Scarano, S. Bordiga, C. Lamberti, A. Zecchina, *Prog. Surf. Sci.* **2004**, 76, 71-146.

[40] J. T. Stuckless, N. AI-Sarraf, C. Wartnaby, D. A. King, *J. Chem. Phys.* **1993**, 99, 2202-2212.

[41] M. Cerro-Alarcó, B. Bachiller-Baeza, A. Guerrero-Ruiz, I. Rodríguez-Ramos, *J. Mol. Catal. Chem.* **2006**, 258, 221-230.

[42] R. S. Bordoli, J. C. Vickerman, J. Wolstenholme, *Surf. Sci.* **1979**, 85, 244-262.

[43] A. M. Gadalla, B. Bower, *Chem. Eng. Sci.* **1988**, 43, 3049-3062.

[44] J. Wei, E. Iglesia, *J. Phys. Chem. B* **2004**, 108, 4094-4103.

[45] A. Sadezky, H. Muckenhuber, H. Grothe, R. Niessner, U. Pöschl, *Carbon* **2005**, 43, 1731-1742.

[46] P. Wang, E. Tanabe, K. Ito, J. Jia, H. Morioka, T. Shishido, K. Takehira, *Appl. Catal., A* **2002**, 231, 35-44.

[47] H. S. Bengaard, J. K. Nørskov, J. Sehested, B. S. Clausen, L. P. Nielsen, A. M. Molenbroek, J. R. Rostrup-Nielsen, *J. Catal.* **2002**, 209, 365-384.

[48] A. Rinaldi, J.-P. Tessonnier, M. E. Schuster, R. Blume, F. Girgsdies, Q. Zhang, T. Jacob, S. B. Abd Hamid, D. S. Su, R. Schlögl, *Angew. Chem. Int. Ed.* **2011**, 50, 3313-3317.

[49] D. A. M. Monti, A. Baiker, *J. Catal*. **1983**, 83, 323-335.

[50] M. Fadoni, L. Lucarelli, *Stud. Surf. Sci. Catal.* **1999**, 123, 289-342.

3.7 Supporting information

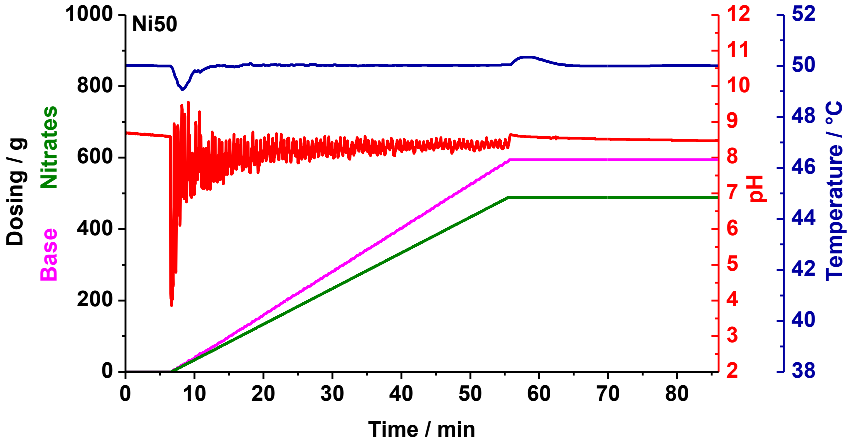

Figure S3.1 Synthesis protocol Ni50 by pH constant co-precipitation. The red line corresponds to the pH, the blue line to the temperature. The green and the pink lines correspond to the dosing amount of the nitrate and the basic solution, respectively.

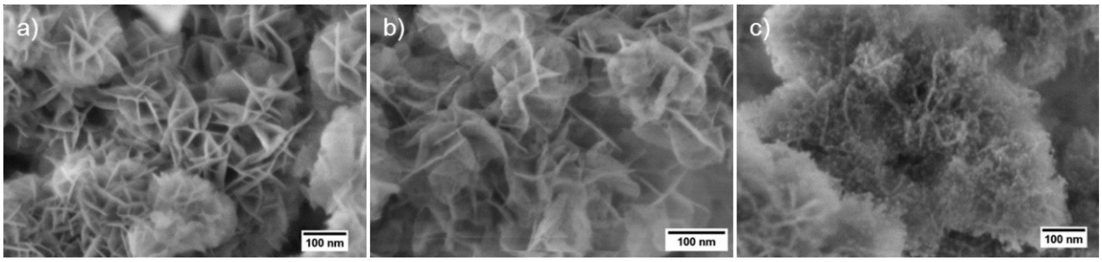

Figure S3.2 The SEM images [15] of the Ni50 htl precursor shows the typical platelet-like morphology of hydrotalcites (a), of calcined Ni50-600 (b) and of reduced Ni50-600-800 which shows the preserved platelet-like morphology of the htl precursor and revealing the formation of small spherical particles (c).

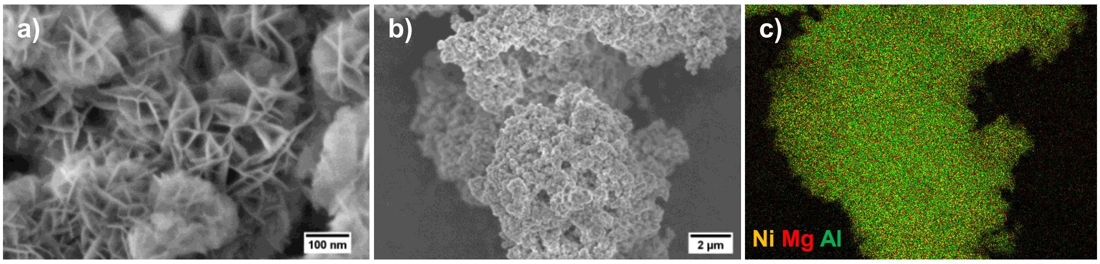

Figure S3.3 The SEM images of the Ni50 htl precursor shows the typical platelet-like morphology of hydrotalcites (a and b) and the corresponding Ni, Mg, Al mapping illustrates the homogeneous metal distribution of all three species.

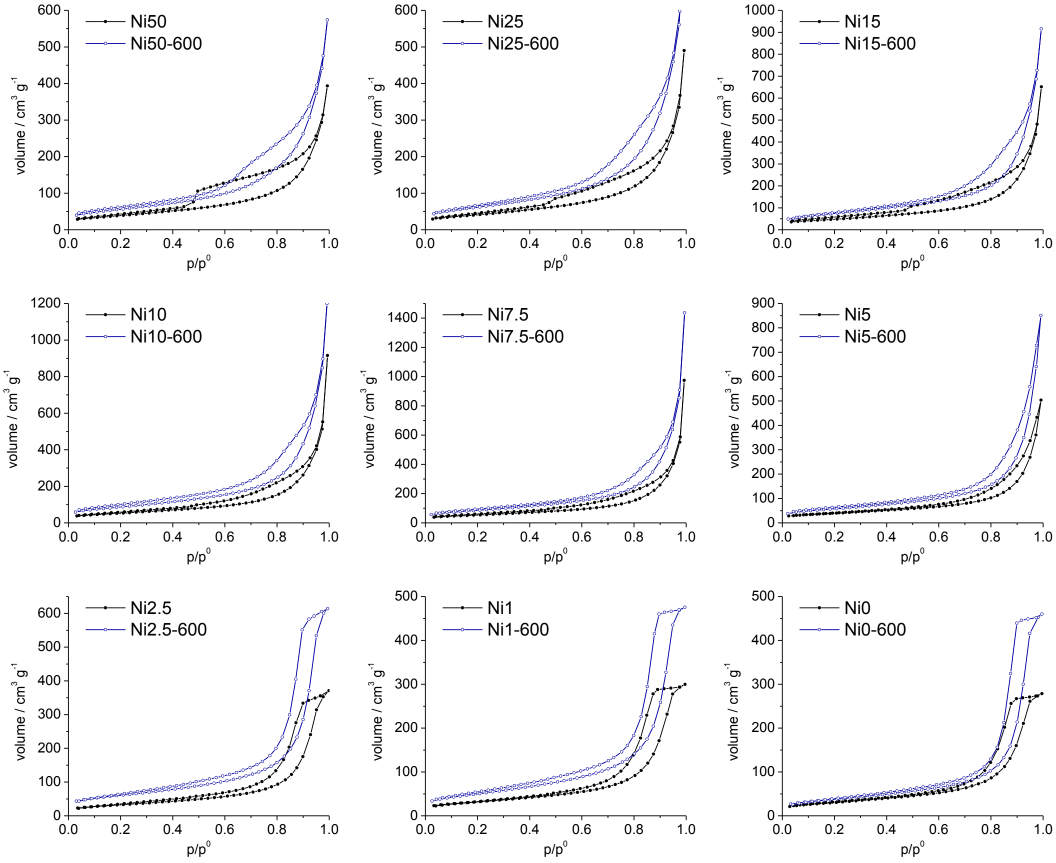

Figure S3.4 BET N_2 isotherms of precursors and calcined samples.

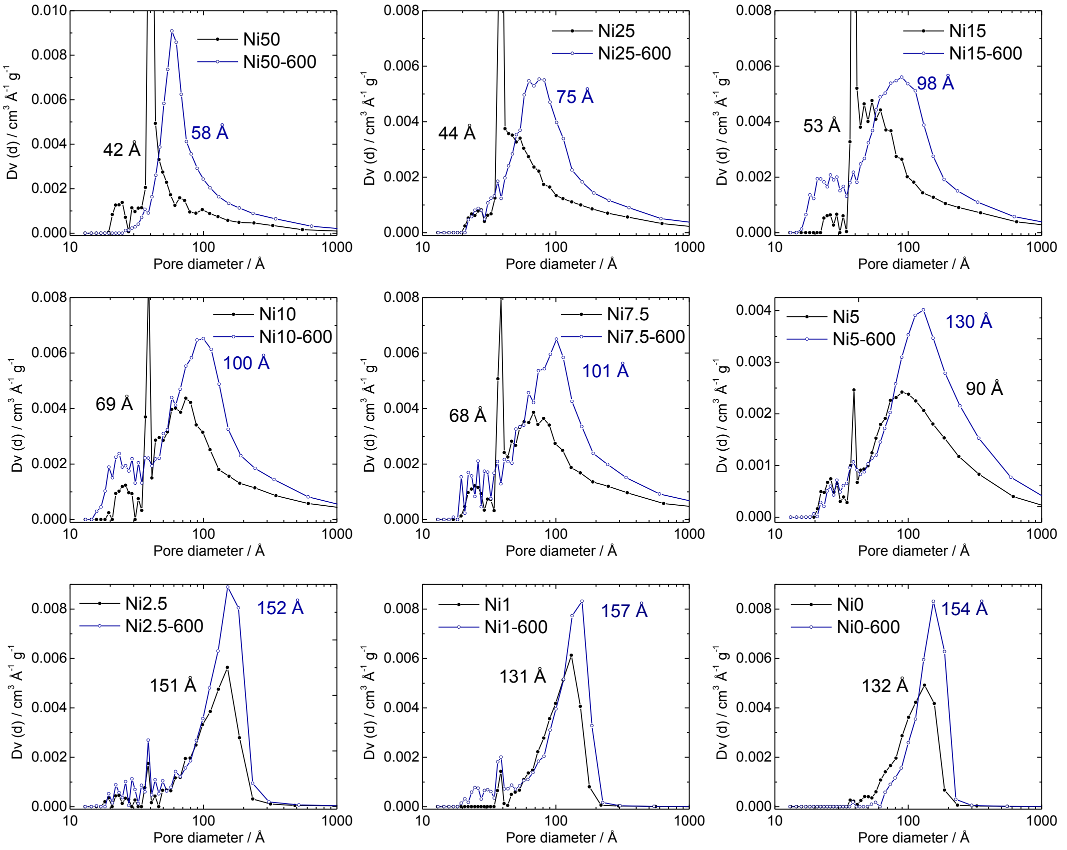

Figure S3.5 BET Pore size distribution (PSD) of precursors and calcined samples determined from desorption branch of N_2 isotherms with BJH method (The narrow PSD around 39 Å is attributed to the Tensile Strength Effect (TSE) and has not been taken into account in the analysis [S1]).

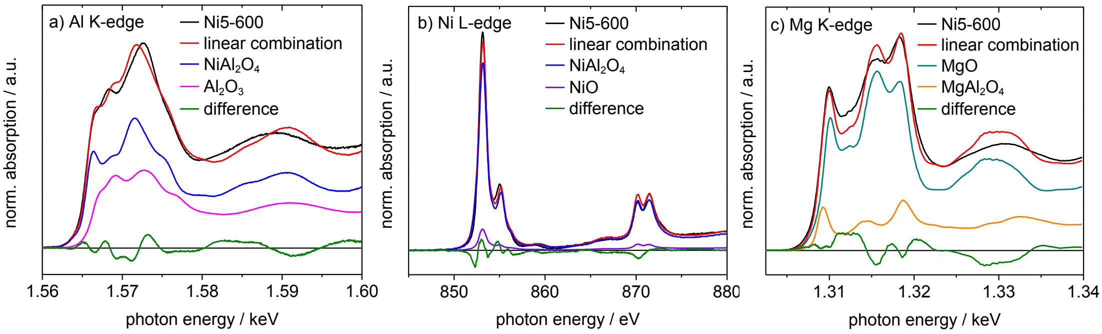

Figure S3.6 Fitted (a) Al K-, (b) Ni L- and (c) Mg K-NEXAFS spectra of Ni5-600.

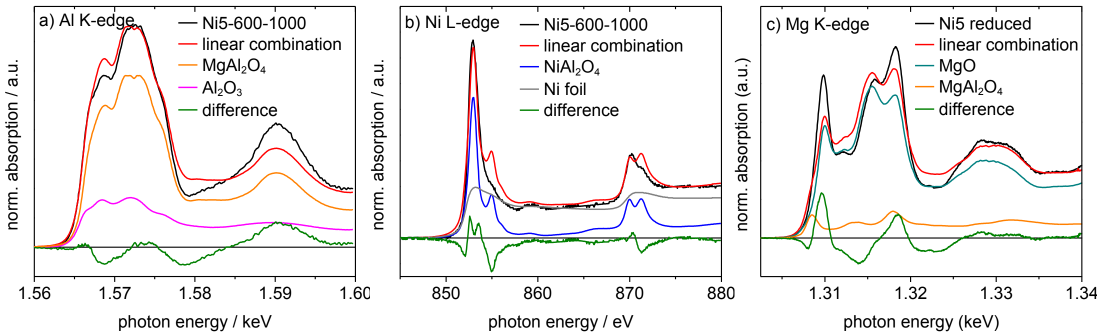

Figure S3.7 Fitted (a) Al K-, (b) Ni L- and (c) Mg K-NEXAFS spectra of Ni5-600-1000.

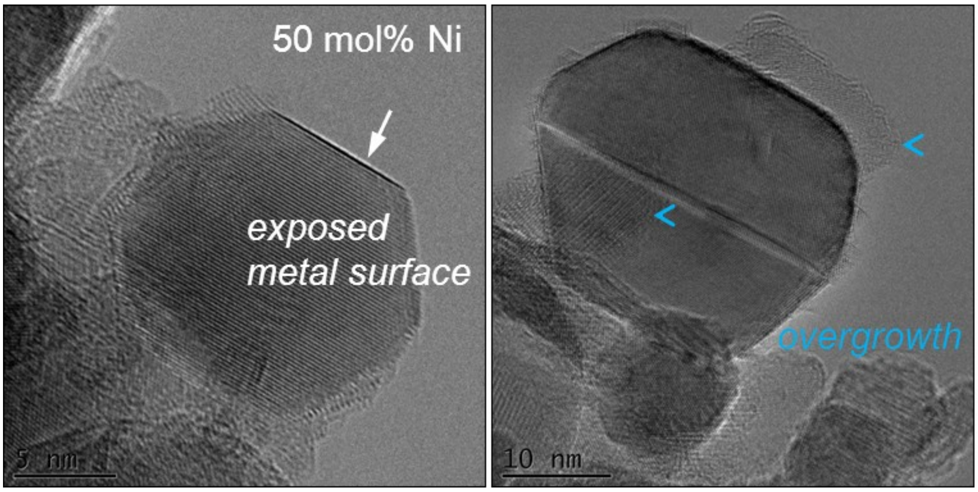

Figure S3.8 HR-TEM images of Ni nanoparticles in Ni50-600-1000. The arrowheads indicate the overgrowth.

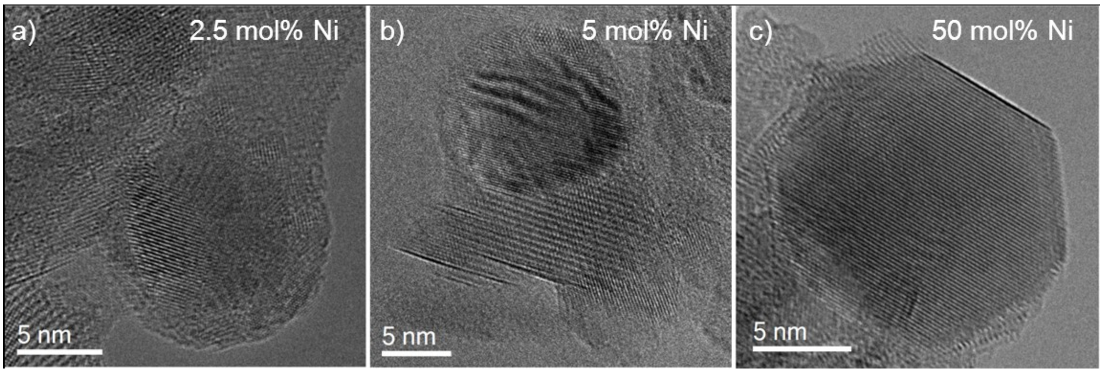

Figure S3.9 HR-TEM images of Ni2.5-600-1000 (a), Ni5-600-1000 (b) and Ni50-600-1000 (c) (uncolored version).

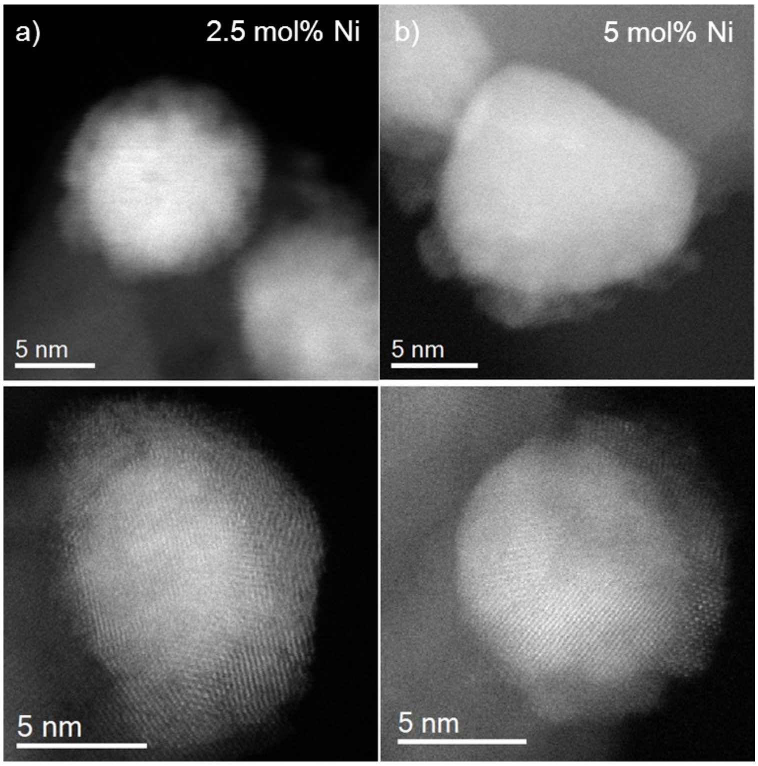

Figure S3.10 HR-STEM investigation of the overgrowth on Ni nanoparticles reduced at 1000 °C. High resolution STEM images of Ni2.5-600-1000 (a) and Ni5-600-1000 (b) (uncolored version).

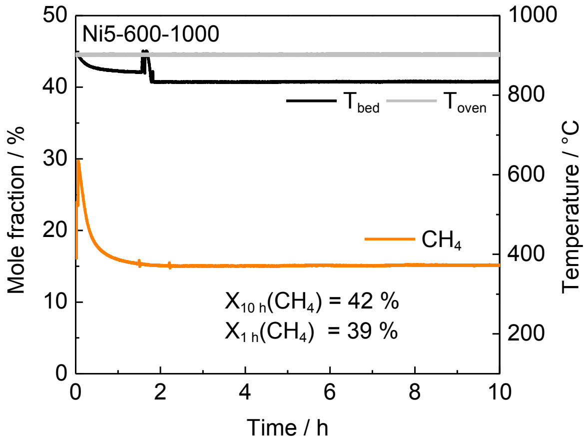

Figure S3.11 Effluent mole fraction of methane of Ni5-600-1000 during DRM at 900 °C in 32% CH_4 and 40% CO_2 in Ar.

3.7.1 SI References

[S1] J. C. Groen, L. A. A. Peffer, J. Pérez-Ramírez, *Microporous Mesoporous Mater.* **2003**, 60, 1-17.

4 The role of carbonaceous deposits in the activity and stability of Ni-based catalysts applied in the dry reforming of methane

Hendrik Düdder, Kevin Kähler, Bastian Krause, Katharina Mette, Stefanie Kühl, Malte Behrens, Viktor Scherer, Martin Muhler

Abstract

Highly stable Ni catalysts with varying Ni contents up to 50 mol% originating from hydrotalcite-like precursors were applied in the dry reforming of methane at 800 and 900 °C. The integral specific rate of methane conversion determined after 10 h on stream was 3.8 mmol s^{-1} g_{cat}^{-1} at 900 °C. Due to the outstanding high activity, a catalyst mass of just 10 mg had to be used to avoid operating the reaction in thermodynamic equilibrium. The resulting WHSV was as high as 1.44×106 ml g_{cat}^{-1} h^{-1}. The observed axial temperature distribution with a pronounced cold spot was analyzed by computational fluid dynamics simulations to verify the strong influence of this highly endothermic reaction. Transmission electron microscopy and temperature-programmed oxidation experiments were used to probe the formation of different carbon species, which was found to depend on the catalyst composition and the reaction temperature. Among the formed carbon species, multi-walled carbon nanofibers were detrimental to the long-term stability at 800 °C, whereas their formation was suppressed at 900 °C. The formation of graphitic carbon at 900 °C originating from methane pyrolysis played a minor role. The methane conversion after 100 h of dry reforming at 900 °C compared to the initial one amounted to 98% for the 25 mol% Ni catalyst. The oxidative regeneration of the catalyst was achieved in the isothermal mode using only carbon dioxide in the feed.

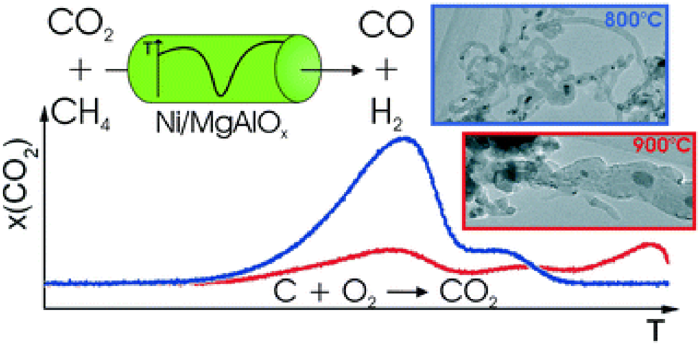

4.1 Introduction

Due to the threatening shortage of crude oil, one of the major challenges of present research is the environmentally friendly and sustainable production of raw materials for fuel production and chemical synthesis. CO, as a component of synthesis gas, is one of the most important industrially used C1 building blocks, which is applied in many large-scale processes such as the synthesis of hydrocarbons, methanol, and dimethyl ether as well as in oxo-synthesis [1,2]. A promising feedstock for CO production may be CO_2, which can be recycled using renewable energy and reincorporated in the value-added chain as a carbon source. Additionally, using CO_2 as a feedstock for industrial products may help to improve the climate balance to a minor extent, as the global warming caused by the continuously increasing emission of the well-known greenhouse gases CO_2, NO_x and CH_4 is a huge environmental problem [3,4].

One efficient way to generate synthesis gas starting from CO_2 is the dry reforming of methane (DRM, eqn (4.1)). The resulting synthesis gas is characterized by a H_2/CO ratio close to unity, which is therefore an interesting feedstock particularly in oxo- or Fischer–Tropsch synthesis [5,6,7,8].

$$CO_2+CH_4 \leftrightarrow 2\ H_2+2\ CO \qquad \Delta_r H_0 = 247\ \mathrm{kJ\ mol^{-1}} \qquad (4.1)$$

In addition to noble metals such as Pt, Rh, or Ru, Ni-based catalysts are known to be active in the DRM [9,10]. The noble metal catalysts are highly stable during the DRM, but are less suitable because of their high prices, whereas the non-noble metal catalysts suffer from a lack of stability due to strong coking at moderate temperatures [11,12]. The carbon deposits formed during the DRM can differ in their morphology and reactivity [13].

Table 4.1 summarizes examples of catalyst activities in the DRM reported in the literature [14,15,16,17,18,19,20,21,22]. For a better comparison, specific average reaction rates $r_{\mathrm{CH_4}}$ were calculated for all catalysts according to eqn (4.2), where m_{cat} is the catalyst mass and $\dot{n}_{\mathrm{CH4,in}}$ and $\dot{n}_{\mathrm{CH4,out}}$ are the molar flows of methane at the entrance and the exhaust of the reactor, respectively.

$$r_{CH_4} = \frac{\dot{n}_{CH_4,in} - \dot{n}_{CH_4,out}}{m_{cat}} \qquad (4.2)$$

The molar flows can be estimated based on the reported weight hourly space velocity (WHSV), CH_4 conversion, feed gas composition, and catalyst mass. As described in ref. [22], we recently succeeded in synthesizing a Ni-based catalyst from a hydrotalcite-like (htl) precursor that shows outstanding stabilities during the DRM even at 900 °C. It has to be pointed out that many studies report degrees of methane conversion exceeding 90%. Those measurements reach thermodynamic equilibrium and, as a result, comparisons of activity and stability may be misleading because of too small space velocities. In this study, reaction conditions were chosen far below the equilibrium conversion, resulting in exceptionally low catalyst amounts to ensure a sufficiently high space velocity.

Table 4.1 Evaluated average reaction rates of selected catalysts from the literature.

Catalyst	Ref.	WHSV/ml g^{-1} h^{-1}	T_{DRM}/°C	X_{CH_4}/%	Reaction rate/mmol s^{-1} g_{cat}^{-1}
1 wt% Ni/Al_2O_3	14	20 000	800	74	0.09
10 wt% Ni/Al_2O_3	15	52 000	800	80	0.13
10 wt% Ni/Al_2O_3	15	52 000	900	95	0.15
13.6 wt% NiO/5.1 wt% MgO/SA	16	40 000	800	34	0.08
13.6 wt% NiO/5.1 wt% MgO/SA	16	40 000	850	48	0.12
13.6 wt% NiO/5.1 wt% MgO/SA	16	40 000	900	60	0.15
β-Mo_2C	17	2870	847	92	0.02
Ni–Co/Al_2O_3	14	20 000	800	61	0.08
NiO/$MgAlO_x$	18	34 000	800	95	0.12
NiO–CaO (Ni/Ca = 3)	19	11 500	850	98	0.07
NiO–CaO (Ni/Ca = 3)	19	70 000	850	62	0.27
$NiRhCe_2Zr_{1.51}$	20	30 000	800	94	0.03
$NiRhCe_2Zr_{1.51}$	20	12 000	800	40	0.04
2Ni–1Zr/MCM-41	21	50 000	800	95	0.15
55 wt% Ni/$MgAlO_x$	22	1 440 000	800	62	3.5
55 wt% Ni/$MgAlO_x$	22	1 440 000	900	74	4.2

Considering the thermodynamic equilibrium composition of the major components CO_2, CH_4, CO, H_2, C, and H_2O (Figure 4.1), a promising way to overcome the deactivation caused by coking is to carry out the DRM at elevated temperatures. According to these thermodynamic calculations, the carbon formation due to the exothermic Boudouard equilibrium (eqn (4.3)) is negligible at temperatures higher than 750 °C. However, increasing the temperature causes sintering of the active metal particles and thereby loss of active surfaces. Furthermore, endothermic homogeneous gas phase reactions are favored, for instance, the pyrolysis of methane (eqn (4.4)) [6].

$$2\,CO \leftrightarrow CO_2 + C \qquad \Delta_r H^0 = -172\ \mathrm{kJ\ mol^{-1}} \qquad (4.3)$$

$$CH_4 \rightarrow 2\,H_2 + C \qquad \Delta_r H^0 = 75\ \mathrm{kJ\ mol^{-1}} \qquad (4.4)$$

$H_2+CO_2 \leftrightarrow H_2O+CO$ $\Delta_rH^0 = \quad 41\ kJ\ mol^{-1}$ (4.5)

$C+O_2 \rightarrow CO_2$ $\Delta_rH^0 = -394\ kJ\ mol^{-1}$ (4.6)

In addition to the need for an efficient catalyst for CO_2 conversion, a substantial heat transfer into the reactor is required due to the high endothermicity of the DRM. To establish a sustainable process, the use of renewable energy sources such as wind or solar power is required. These regenerative energies are supplied non-continuously, and the DRM additionally offers an alternative in terms of energy storage [23]. A suitable approach to store and transmit surplus energy is through chemical energy transmission systems (CETS) [24,25,26].

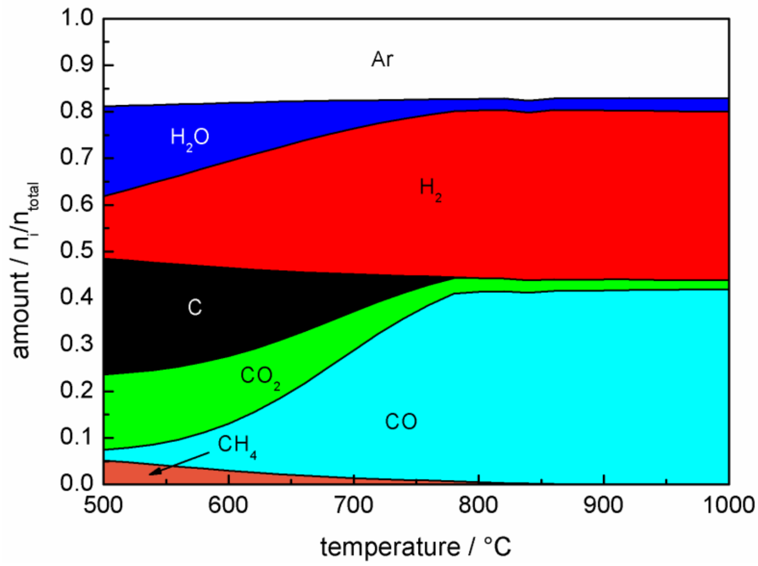

Figure 4.1 Calculated product distribution in thermodynamic equilibrium of 32% CH_4 and 40% CO_2 in Ar as a function of temperature considering the products C, HO, CO_2, CH_4, H_2 and CO. The calculations were based on a Gibbs free energy minimization implemented in CHEMCAD 6.4.2 by Chemstations.

These CETS are based on a reversible reaction network: at energy-rich periods the energy is used to perform an endothermic forward reaction such as the DRM, thereby storing power in chemical bonds, whereas at energy-lean periods an exothermic backward reaction such as methanation or Fischer–Tropsch synthesis can be used to release the stored energy. This application can additionally be combined with long-distance heat pipelines allowing the product to be transported to a consumer, where the conversion via the reverse reaction releases the stored energy [23,27,28]. As an alternative to the direct storage of primary energy, synthesis gas produced by the DRM can be converted to high-density energy carriers [23]. Following this concept and using primarily regenerative surplus energy, it is possible to perform even highly endothermic reactions in an economically and ecologically favorable way.

In our present study, Ni catalysts prepared from htl precursors with varying Ni contents, which have large surface areas and are thermally stable at elevated temperatures, were investigated [22]. Additionally, strong interactions between the Ni nanoparticles and the support matrix can be achieved with an htl precursor [18,29,30,31,32,33,34]. The role of the reaction temperature as well as the Ni loading in the nature of the carbon deposits and their influence on the activity and the long-term stability of the catalysts were investigated using steady-state activity tests combined with transient kinetic measurements such as temperature-programmed oxidation (TPO) supported by transmission electron microscopy (TEM) to identify the generated carbon species. The influence of the endothermic reaction on the temperature distribution in the catalyst bed was investigated by measuring axial temperature profiles and simulations based on computational fluid dynamics (CFD).

4.2 Experimental

4.2.1 Catalyst preparation

A series of Ni/$MgAlO_x$ catalysts was synthesized from htl precursors with the general formula $Ni_xMg_{0.67-x}Al_{0.33}(OH)_2(CO_3)_{0.17} \cdot mH_2O$, which were obtained by the constant pH co-precipitation method at 50 °C using aqueous 0.6 M NaOH, 0.09 M Na_2CO_3, and 0.4 M metal nitrate solutions at pH 8.5. The precipitates were aged for 0.5 h in the mother liquor, filtered, thoroughly washed with water, and dried at 100 °C. The amount of Ni was varied between 0–50 mol%, i.e. $0 \leq x \leq 0.5$, leading to Ni amounts of 0 to 55 wt% in the final catalyst. The precursors were calcined in air at 600 °C for 3 h.

4.2.2 Catalyst characterization

X-ray powder diffraction (XRD) measurements were performed with a STOE STADI-P transmission diffractometer equipped with a primary focusing Ge(111) monochromator and a 3° linear position-sensitive detector (PSD) using $CuK_{\alpha,1}$ radiation. Small amounts of X-ray amorphous grease were used to fix the powder samples between two thin films of polyacetate foil. Specific surface areas of the calcined material were measured by N_2 physisorption (Quantachrome Autosorb-1) and evaluated using the BET method. Prior to the physisorption measurements, the calcined samples were outgassed for 4 h at 150 °C. Temperature-programmed reduction (TPR) of the samples was performed in a fixed-bed reactor in a quartz tube (TPDRO-1100, CE Instruments) using 5% H_2 in Ar and a total flow of 80 Nml min^{-1} with a linear heating rate of 6 °C min^{-1}. The H_2 consumption was monitored with a calibrated thermal conductivity detector (TCD). To determine the specific Ni surface area, the H_2 pulse chemisorption method was applied. The samples were reduced in a fixed-bed reactor using 5% H_2 in Ar, a total flow of 80 Nml min^{-1} and a heating rate of 6 °C min^{-1} to 1000 °C. After cooling to 50 °C in Ar, a defined volume of pure H_2 was introduced by dosing pulses of 250 µl, until no further H_2 uptake was detected. The Ni metal surface areas were determined assuming dissociative hydrogen chemisorption and an adsorption stoichiometry of $H_{ads}:Ni_{surf} = 1:1$ [35].

After the TPO experiments, the samples were reactivated by reduction and exposed to a second DRM run under the conditions described below to obtain the spent samples for microstructural characterization. Afterwards, the catalysts were separated from the diluent by sieving, dispersed in $CHCl_3$ and deposited on a holey carbon film supported on a copper grid. The microstructure of the spent catalysts was examined by using Philips CM200 transmission electron microscopes (TEM) equipped with a LaB_6 cathode or a field electron gun. High-resolution images were taken with a CCD camera. For good statistics, 40 to 80 images were taken for each sample on different agglomerates and regions of the catalysts.

4.2.3 Catalytic DRM tests

The catalytic DRM tests were performed in a continuously operated flow system at atmospheric pressure using a fixed-bed tubular quartz reactor of 8 mm inner diameter. The reactor was equipped with a ceramic tube of 3 mm outer and 1 mm inner diameter in the radial center of the reactor. By means of a movable thermocouple inside this ceramic tube, temperature profiles in the axial direction were obtained. For the steady-state measurements, a calibrated on-line gas chromatograph (GC, Shimadzu 14-B) was used to analyze the product gas composition every 60 minutes. The GC was equipped with two columns (Porapak N and Molsieve 5 A) and a TCD. For the transient studies, a coupled IR detector (CO, CO_2 & CH_4) and a TCD for H_2 (Emerson MLT4 multichannel analyzer) and a paramagnetic O_2 detector (Magnos 16) were used.

For the catalytic tests, 10 mg of the calcined catalyst (sieve fraction of 250–355 µm) was diluted with 490 mg of high purity SiC (sieve fraction of 125–180 µm). Initially, the catalyst was activated using a linear temperature ramp; it was reduced in a total flow of 20 Nml min^{-1} of 4% H_2 in Ar (purity 99.9%, 99.999%) by heating to the desired maximum temperature of reduction with a linear heating rate of 5 °C min^{-1}. The final temperature was held constant for 30 min. Afterwards, the catalyst was cooled or heated to the specified reaction temperature in Ar (99.999%). The dry reforming reaction was carried out with a gas mixture consisting of CH_4 (99.9995%), CO_2 (99.9995%) and Ar in a ratio of 32 : 40 : 28. The total flow was set to 240 Nml min^{-1}. To ensure a CO_2/CH_4 ratio ≥ 1.25 at any time, the

CH_4 partial pressure was increased stepwise while starting the experiment. The reaction was performed at a constant furnace temperature with reaction times of 1, 10, and 100 h. Subsequent to the catalytic tests, the sample was cooled to room temperature in Ar, and a TPO experiment was performed with flow rates of 20 or 40 Nml min^{-1} of 4.5% O_2 in Ar (99.995%, 99.999%) and a linear heating rate of 5 °C min^{-1}. The final temperature of 800 °C was held constant until O_2 consumption was no longer observed. Additionally, a blank experiment with 490 mg of pure SiC including a subsequent TPO experiment was performed.

4.2.4 CNT growth experiments

CNT growth experiments were performed in the same reactor with 10 mg of the 50 mol% Ni catalyst diluted with 490 mg of SiC. The catalyst was heated to 800 °C at a rate of 5 °C min^{-1} in a flow of 20 Nml min^{-1} of 4% H_2 in Ar [36]. The reduced catalyst was cooled to 680 °C. Afterwards, a mixture of 32 Nml min^{-1} CH_4 (99.9995%) and 68 Nml min^{-1} % H_2 (99.9999%) was fed to the reactor for 1 h. The catalyst was then cooled to room temperature in flowing Ar and a subsequent TPO experiment was performed in analogy to the TPO experiments after the DRM.

4.2.5 TPO experiments using carbon reference samples

TPO experiments with different commercially available carbon samples were carried out to obtain reference TPO profiles. CNTs with different amounts of the residual growth catalyst were obtained from Bayer: Baytubes C 70 P containing in total less than 5% of inorganic impurities and Baytubes C 150 HP with less than 1% of inorganic impurities. High surface area graphite powders (HSAG) were used with different specific surface areas: HSAG 100 with 80 m^2 g^{-1} and HSAG 300 with 270 m^2 g^{-1}. For the TPO experiments, the carbon samples were diluted with 490 mg of SiC and placed in the same reactor used for the DRM tests. A TPO experiment similar to the DRM measurements was performed at a heating rate of 5 °C min^{-1}, a maximum temperature of 800 °C, and a total flow of 40 Nml min^{-1} of 4.5% O_2 in Ar. The final temperature was held constant until O_2 was no longer consumed.

4.2.6 Simulation of the axial temperature profiles

The temperature profiles were obtained by moving a thermocouple in the axial direction. As a reference, the temperature profile of pure SiC under DRM conditions was recorded. The temperature profiles of the catalysts during the DRM were obtained after 1 h of time on stream under steady-state conditions. The reactor simulations were carried out using the commercial CFD software FLUENT version 14.0 (Fluent Inc., USA) and appropriate user-defined subroutines. A more detailed description of the model, on which the simulation was based, will be published elsewhere. Due to the complexity of the flow phenomena occurring in fixed-bed reactors, there is a need for complex computational meshes and boundary conditions to determine the actual velocity field in the bed [37,38]. In order to reduce the associated computational effort, the fixed-bed must be handled as a porous medium, which corresponds to the assumption of a quasi-homogeneous reactor model on the sub-grid scale [39]. The energy equation for this porous medium is based on the one-temperature model implemented in ANSYS FLUENT 14.0. It suggests that the temperature of the solid phase equals that of the gas phase due to the local thermal equilibrium between the gas and solid phases. It also assumes one effective thermal conductivity for the porous region [40]. This assumption is justified for the current case because of the low Biot number of the system of about $\mathrm{Bi} = 3 \times 10^{-3}$, mainly resulting from the high thermal conductivity of the used diluent. The flow in the fixed bed is modeled as a porous fluid region with extra terms in momentum balance to allow additional resistance to the flow [40]. Due to the high diameter ratio of the reactor and the particle, the void fraction of the porous fixed-bed was set to a constant value of $\psi = 0.4$. Therefore, an inhomogeneous void fraction distribution only occurs at very small reactor wall distances and does not significantly affect the velocity distribution. The low Reynolds number of the system amounts to about 25 in the tube and 50 in the fixed-bed predict laminar flow. Thus, turbulence modeling was not required. The flow in the porous medium was influenced by the solid matrix removing energy from the reaction zone [40]. The simulation was based on the dry reforming of methane (eqn (4.1)) and the reverse water–gas shift reaction (eqn (4.5)). The kinetic expressions were taken from Richardson and Paripatyadar [27], whereas the equilibrium constant of the RWGS was taken from ref. [41]. Because of the small crushed catalyst and inert particles, external mass and heat transfer limitations were absent [27], leading to an isothermal temperature distribution in the particles with an effectiveness factor of 1.0.

4.2.7 Regeneration of the catalyst

Regeneration of the catalyst was carried out using either the temperature-programmed or the isothermal mode after the DRM at 800 °C. Subsequent to the DRM and cooling to room temperature in Ar, the catalyst was either heated with a linear heating ramp of 5 °C

min^{-1} to a maximum temperature of 800 °C in 4.5% O_2 in Ar or 10% CO_2 in Ar with a total flow of 40 Nml min^{-1}, followed by a further DRM run at 800 °C. For the isothermal regeneration after 20 h of DRM, the feed gas composition was changed to 10% of CO_2 in Ar with a total flow of 40 Nml min^{-1} for 1 h. Afterwards, methane was dosed again, and the DRM was carried out for another 20 h.

4.3 Results and discussion

4.3.1 Characterization of the samples

A series of htl precursors was calcined at 600 °C, resulting in the decomposition of the precursor structure into nearly X-ray amorphous NiMgAl oxides (Figure 4.2A). Only broad modulations of the background are observed at the peak positions of a rock salt structure-type phase such as NiO or MgO. Due to the similar diffraction patterns of MgO and NiO, no detailed phase identification can be achieved based on XRD for the poorly crystalline materials. The surface area was increasing from 134 to 226 $m^2\ g^{-1}$ with increasing Ni content and decreasing Mg content (Table 4.2).

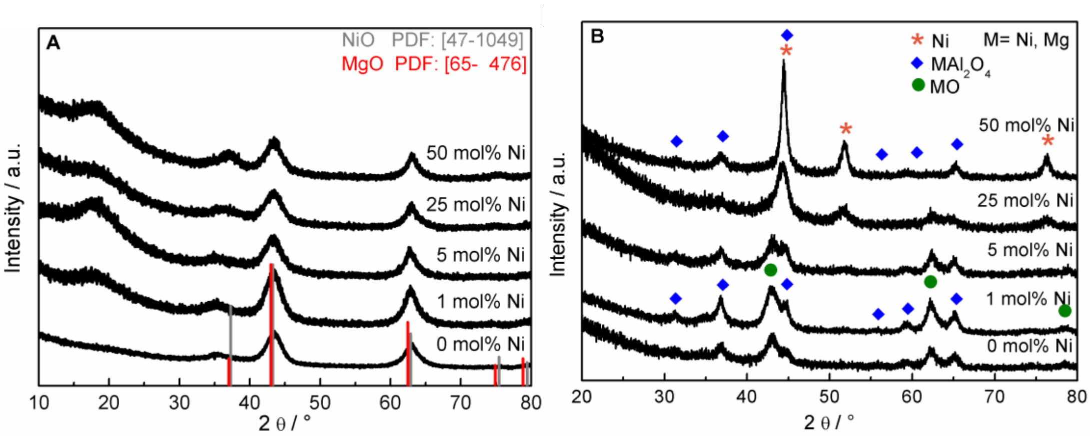

Figure 4.2 XRD patterns of the samples with different Ni contents (A) after calcination of the htl precursor at 600 °C and (B) after reduction at 1000 °C.

Table 4.2 Specific Ni surface area, dispersion, particle size, specific BET area, and carbon equivalents formed during TPO experiments after 10 h of DRM at 900 °C.

Ni content / mol%	Ni surface area / $m^2\ g^{-1}$	Ni dispersion / %	Ni particle size / nm (TEM)	BET area / $m^2\ g^{-1}$	C equivalents / mmol g_{cat}^{-1}
0	0.0	—	—	134	33
1	0.1	1.0	7.0	180	13
5	3.0	6.9	9.3	205	12
25	5.0	2.5	7.3	221	22
50	6.0	1.6	19.4	226	24

The reduction behavior of the calcined materials was investigated using TPR in 5% H_2 in Ar (Figure 4.3A). Upon reduction with H_2, the Ni oxide components of the calcined samples were reduced to metallic Ni. The maximum reduction temperature was decreasing with increasing Ni content from 915 °C for 1 mol% Ni to 670 °C for 50 mol% Ni, suggesting autocatalytic reduction kinetics due to hydrogen spill-over. The reduction profiles revealed that at a reduction temperature of 1000 °C, Ni was completely reduced in all samples. According to the criterion developed by Monti and Baiker [42], the amount of sample used in the TPR experiments was adjusted to obtain comparable peak areas. Upon reduction at 1000 °C, a nanoscopic segregation of the components had taken place and XRD clearly confirmed the presence of metallic Ni (Figure 4.2B). While the oxidic components in the catalyst with the highest Ni content were still only poorly crystalline structures, the intensity of the MgO and $MgAl_2O_4$ phases increased with decreasing Ni content. In order to determine the accessible Ni metal surface area, H_2 pulse chemisorption measurements were applied using samples reduced at 1000 °C. An increasing Ni surface area was found for increasing Ni contents (Table 4.2). It is remarkable that the Ni dispersion of the 25 mol% Ni catalyst is 2.5 times higher than the Ni dispersion of the 1 mol% Ni sample, pointing to a strong embedding effect of the support matrix. Therefore, sintering of the Ni particles is suppressed and even at higher loadings a degree of Ni dispersion in the range 1–7% is achieved (Table 4.2).

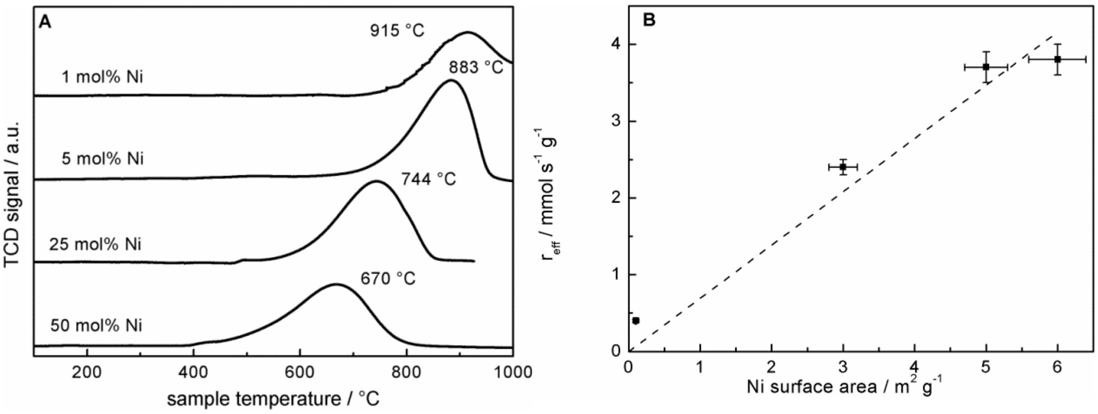

Figure 4.3 (A) TPR profiles of the calcined samples with different Ni contents using 5% H_2 in Ar with a total flow of 80 Nml min^{-1} and a linear heating rate of 6 °C min^{-1}. (B) Determined specific reaction rates during the DRM at 900 °C after reductive pretreatment up to 1000 °C as a function of the specific Ni surface area. The accuracy of the measurements is estimated to be ±5% in the case of the average reaction rates and ±6% for the specific Ni surface area.

4.3.2 Catalytic testing

The TPR results revealed a strong influence of the catalyst composition on the reducibility of Ni. Therefore, the studies on the effect of the Ni loading on the catalytic performance were carried out with a reductive pre-treatment up to 1000 °C for all catalysts to ensure a complete reduction of Ni and to exclude the influence of different pre-treatment temperatures. During the reduction, the H_2 consumption was only detectable for the samples with the highest Ni contents of 25 mol% and 50 mol% Ni due to the low amount of the catalyst used in the reactor. In good agreement with the TPR results, reduction peaks at around 720 °C for 25 mol% Ni and 670 °C for 50 mol% Ni were observed.

We showed recently that the catalyst with 50 mol% Ni had a higher stability in DRM at 900 °C than at 800 °C [22]. Therefore, the comparison of the ex-htl catalysts with varying Ni contents was performed at 900 °C. During the DRM, the catalysts with Ni contents between 5 mol% and 50 mol% achieved a stable degree of conversion over 10 h on stream as shown in Figure 4.4B, whereas for the catalyst with 1 mol% Ni an activation period of about 2 h was observed (Figure 4.4A). The detected H_2/CO ratio was lower than the stoichiometric ratio of 1:1, which would be expected for the exclusively occurring DRM (Table 4.3). In addition, the formation of water was detected, indicating the simultaneously occurring reverse water–gas shift reaction (RWGS, eqn (4.5)). The degrees of methane conversion ($X_{\mathrm{CH_4}}$) as well as the integral specific rates of methane conversion ($r_{\mathrm{CH_4}}$, eqn (4.2)) after 10 h on stream are summarized in Table 4.3. The degree of methane conversion increased with higher Ni content and correlated almost linearly with the specific Ni surface area (Figure 4.3B). During the catalytic test using pure SiC, no significant conversion within the detection limits was observed.

Table 4.3 Degree of methane conversion, average reaction rate, metal sites, average turnover frequency, H_2/CO ratio, and H_2 yield after 10 h of DRM at 900 °C.

Ni content / mol%	$X_{\mathrm{CH_4,10\,h}}$ / %	Reaction rate / mmol s^{-1} g_{cat}^{-1}	Metal sites / µmol g_{cat}^{-1}	TOF / s^{-1}	H_2 / CO	H_2 Yield
0	0	0.0	—	—	—	—
1	7	0.4	3	—	0.7	0.07
5	42	2.4	77	31	0.7	0.36
25	66	3.7	128	29	0.8	0.61
50	67	3.8	154	25	0.8	0.63

The almost linearly increasing degree of conversion with increasing Ni surface area might indicate that the average turnover frequency does not depend on the Ni particle size

(Table 4.3). However, both the dispersion (1–7%) and the mean particle size of the nickel particles estimated by TEM (7–19 nm) are comparable for all investigated catalysts (Table 4.2). Therefore, the catalytic data do not allow us to draw any conclusions on the structure sensitivity of DRM over Ni catalysts, which is known to be structure-sensitive [10].

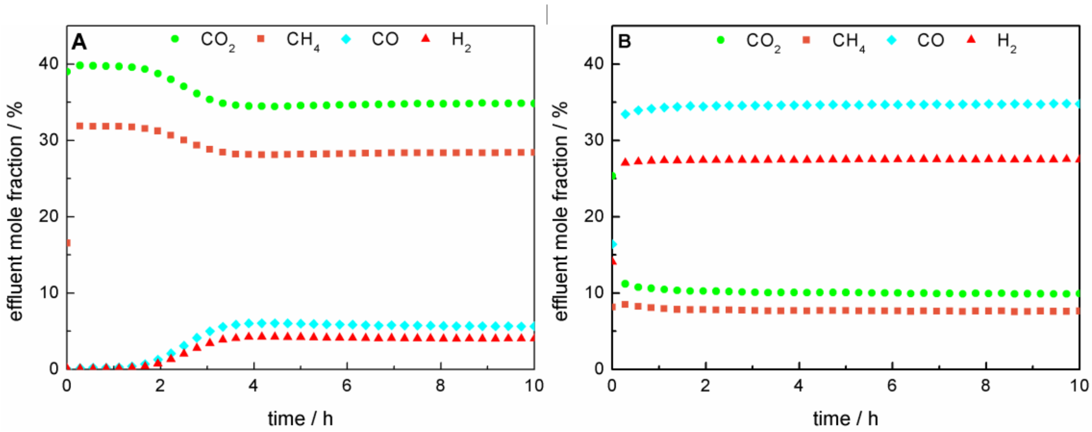

Figure 4.4 Effluent mole fractions during DRM at 900 °C in a total flow of 240 Nml min^{-1} consisted of 32% CH_4 and 40% CO_2 in Ar for A) 1 mol% Ni and (B) 50 mol% Ni catalysts.

In the following, the kinetic DRM investigations were focused on the most active catalyst with 50 mol% Ni. Instead of 1000 °C maximum reduction temperature for the comparison of the different Ni contents, the catalyst was pre-reduced at temperatures only up to 800 °C, which should lead to complete reduction according to the TPR results. The lower pretreatment temperature led to a slightly higher activity in the DRM due to less severe sintering of the Ni particles as detected by TEM [22]. After the pre-reduction, the catalyst was tested in the DRM at 800 °C and 900 °C. The integral specific rates of methane conversion determined after 60 min on stream were 3.5 mmol s^{-1} g_{cat}^{-1} at 800 °C and 4.2 mmol s^{-1} g_{cat}^{-1} at 900 °C [22]. Due to the outstanding activity the catalyst mass had to be lowered to 10 mg to avoid operating the reaction in thermodynamic equilibrium. The resulting WHSV was as high as 1.44 × 106 ml g_{cat}^{-1} h^{-1} corresponding to 240 Nml min^{-1} total gas flow. The calculated thermodynamic equilibrium and the highest observed degrees of methane conversion are plotted against temperature in Figure 4.5, as these are closest to equilibrium. For this purpose, the lowest measured temperature in the catalyst bed was used. Figure 4.5 clearly shows that both DRM measurements at 800 °C and at 900 °C were below the thermodynamic equilibrium conversion.

The catalysts with Ni contents of 25 and 50 mol% were additionally tested in long-term measurements for 100 h at 900 °C after optimized maximum temperatures of pre-treatment of T_{Red} = 850 °C for 25 mol% and T_{Red} = 800 °C for 50 mol%. Both catalysts showed remarkable stability during the DRM as a function of time. For the catalyst with 50 mol%

Ni, a degree of conversion of 94% of the initial conversion was detected after 100 h of DRM, while the stability of the 25 mol% Ni catalyst was even higher, amounting to 98% of the initial conversion.

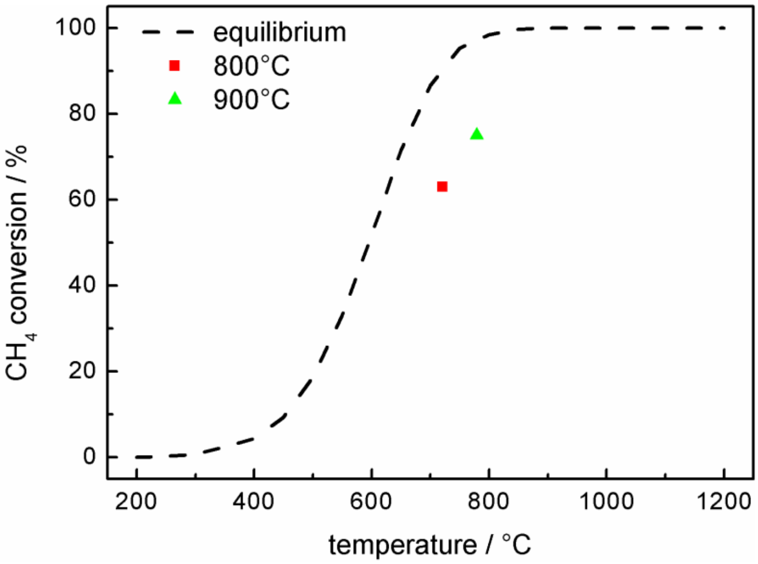

Figure 4.5 Comparison of experimental methane conversion over the 50 mol% Ni catalyst and equilibrium methane conversion in DRM. Equilibrium conversion was calculated using CHEMCAD and a feed composition of 32% CH_4, 40% CO_2 and 28% Ar.

4.3.3 Temperature profiles

To assess the influence of the high endothermicity of the DRM (eqn (4.1)), axial temperature profiles of the catalyst bed were measured under reaction conditions. The profiles were determined after 1 h of DRM at 900 °C and during the catalytic tests after the reductive pre-treatment up to 1000 °C. With the exception of the 1 mol% Ni sample, steady-state conditions were achieved for all catalysts (Figure 4.4). Three temperature profiles are shown in Figure 4.6: a profile of pure SiC under DRM conditions and the profiles of the catalysts with Ni contents of 5 mol% for medium activity and 50 mol% for high activity under DRM conditions (Table 4.3). The recorded temperatures are plotted as a function of the axial position with respect to the beginning of the catalyst bed at 0 mm. As verified by the temperature profile of pure SiC, a homogeneous and due to the heat up of the feed gas asymmetric temperature distribution was established in the fixed bed by the furnace. For the active catalysts, the formation of significant cold spots was observed: for 5 mol% Ni $\Delta T > 80$ °C and for 50 mol% Ni $\Delta T > 130$ °C. This temperature gradient lowered the temperature even in the pre-catalyst region. As expected for an endothermic reaction, the temperature difference in the cold spot became larger with increasing conversion of methane. The control thermocouple of the furnace was placed close to the catalyst bed in the annular gap between the quartz reactor and the heater. The large temperature gradient in the catalyst bed led to a lower measured temperature at the control thermocouple. For this reason, the furnace adjusted the temperature and the temperature profile was shifted to higher temperatures. Therefore, temperatures slightly higher than 900 °C were detected in the pre-catalyst zone for the active catalysts.

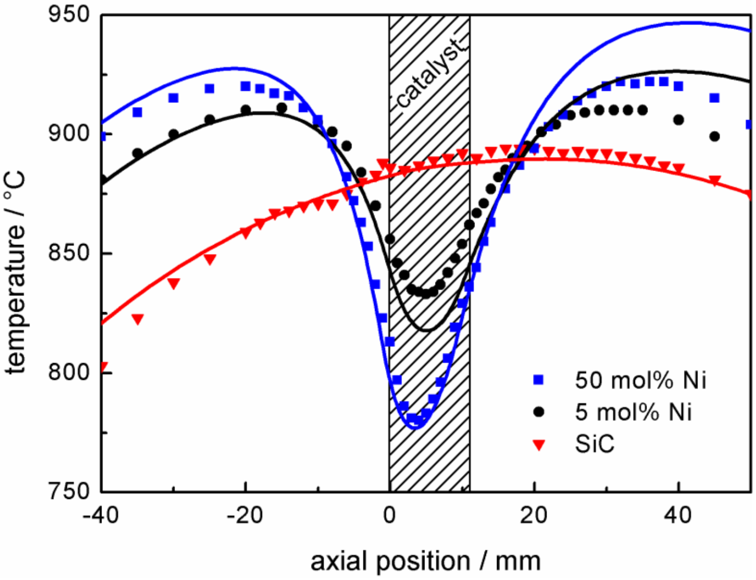

Figure 4.6 Measured axial temperature profiles (symbols) and the corresponding simulated temperature profiles (lines). The catalyst bed is positioned between 0 and 11 mm using 10 mg of catalyst diluted in 490 mg of SiC with a total flow rate of 240 Nml min^{-1} and a composition of 32% CH_4 and 40% CO_2 in Ar.

The measured axial temperature profiles were compared to the simulated ones (Figure 4.6). The axial position of the simulated profiles was adjusted such that the turning point matches with the measurements. The simulations of the temperature profiles are in good agreement with the measured temperatures reproducing the qualitative and the quantitative characteristics of the temperature profiles with a maximum deviation of 15 °C close to the fixed-bed area. The model accurately describes the pre-heating phase in front of the bed and the temperature drop in the catalyst bed. The simulation showed further that due to the strong influence of thermal radiation, the lowest temperature in the catalyst bed is not the measured one (radial center of the reactor), but can be located in the radial center of the annular catalyst bed. The temperature difference between the measured and the simulated lowest temperature was detected to be only 5 °C. The heat is transported *via* two ways: the major part is the heat transfer from the quartz reactor into the SiC, and the minor part is from the ceramic tube into the SiC. In the catalyst bed and the pre-heating zone, conduction is the dominant mechanism, whereas the radiative heat transfer merely controls the bed and the gas temperature indirectly by heating up the aluminum oxide and the quartz tube. For the simulation of the temperature profiles, a simple extension of the Richardson kinetics was used to apply the Rh-based kinetics to our Ni-based catalysts. The catalytic activity was multiplied by a constant factor of 16 in the case of 50 mol% Ni and by a factor of 6 in the case of the 5 mol% Ni catalyst. It is worth noting that the investigated Ni-based catalysts are much more active than what Richardson kinetics [27] based on Rh catalysts predicts.

4.3.4 TPO experiments

Ni catalysts tend to form coke deposits during the DRM, which can lead to fast deactivation. To investigate the carbon deposits, temperature-programmed oxidation was applied, and the amounts of O_2 consumed and CO_x formed during a TPO experiment were used as a measure of the amount of carbon deposited during the DRM. Although the catalysts did not show significant deactivation during the DRM, the consumption of O_2 and the simultaneous formation of CO_x due to the removal of carbonaceous species were detected for all samples (eqn (4.6)). Due to the re-oxidation of Ni, the consumption of O_2 is not a suitable measure for the formed carbon deposits during DRM. Therefore, C equivalents were calculated as the sum of the formed CO_x species. In the presence of Ni, the carbon formation was suppressed compared with the pure support (0 mol% Ni). For Ni contents higher than 1 mol%, the amount of carbon formed can be correlated with the degree of methane conversion during the DRM (Table 4.2).

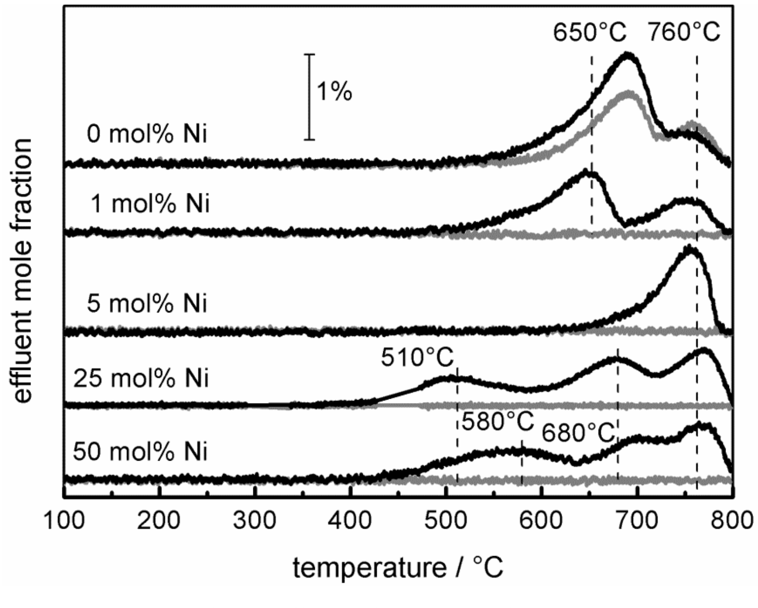

Figure 4.7 TPO profiles of all samples after 10 h of DRM at 900 °C. Effluent mole fractions of CO_2 (black) and CO (grey), with a heating rate of 5 °C min^{-1} up to 800 °C in a total flow of 20 Nml min^{-1} of 4.5% O_2 in Ar.

Depending on the composition of the sample, total and partial oxidation of the carbonaceous deposits was observed. During the TPO experiments with pure $MgAlO_x$ and

SiC, the formation of CO_2 and CO occurred, while for the Ni-containing catalysts exclusively the formation of CO_2 was detected due to Ni-catalyzed CO oxidation. In the TPO profiles shown in Figure 4.7, different peaks can be detected, which are assigned to carbon deposits differing in their stability under oxidizing conditions. The TPO profiles of pure $MgAlO_x$ and 1 mol% Ni contain two peaks with comparable burn-off temperatures. In the presence of Ni, the maximum of the first peak was shifted from 690 to 650 °C. Furthermore, the intensity of this shifted peak was lowered significantly. Simultaneously, the overall amount of removed C was lower compared with the Ni-free sample. For the catalyst with 5 mol% Ni, only one peak at 760 °C was found. In the rather similar TPO profiles of the catalysts containing 25 mol% and 50 mol% Ni, three peaks appeared. The first one was observed in the temperature range between 450 and 570 °C, the second one between 650–700 °C, and the last one at 770 °C.

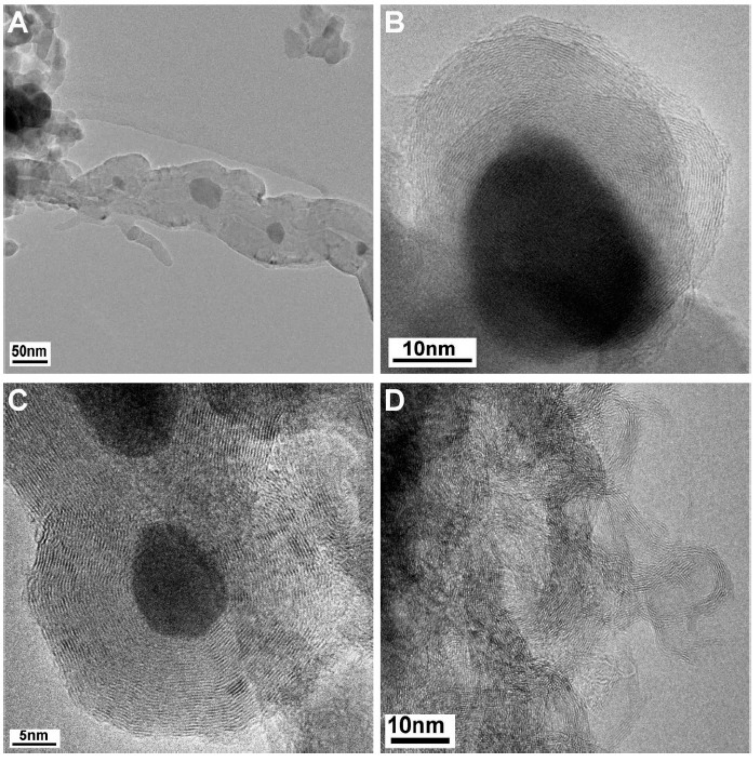

Figure 4.8 TEM micrographs after DRM of 50 mol% (A), 25 mol% (B), 5 mol% (C), and 0 mol% (D) Ni after 10 h of DRM at 900 °C in a total flow of 240 Nml min^{-1} and a composition of 32% CH_4 and 40% CO_2 in Ar.

For the assignment of the different TPO peaks, several approaches were used. TEM micrographs of spent samples revealed the presence of different carbon species as a function of the Ni content as expected from the TPO profiles. The micrographs of the 25 and 50 mol% Ni catalysts show mainly graphite as well as filamentous carbon, *i.e.* multi-walled carbon nanofibers (CNFs, Figure 4.8A and B). For the 5 mol% Ni catalyst, mainly graphitic carbon and no filaments were found (Figure 4.8C), which is in agreement with the TPO profile showing only one major signal at 760 °C. The Ni-free sample led to the formation of far less ordered graphitic carbon layers (Figure 4.8D), in agreement with its TPO profile showing an additional signal at lower temperatures compared to the 5 mol% Ni catalyst. Based on the local microscopy observations, the presence of less ordered graphite cannot be excluded for the catalysts with ≥5 mol% Ni.

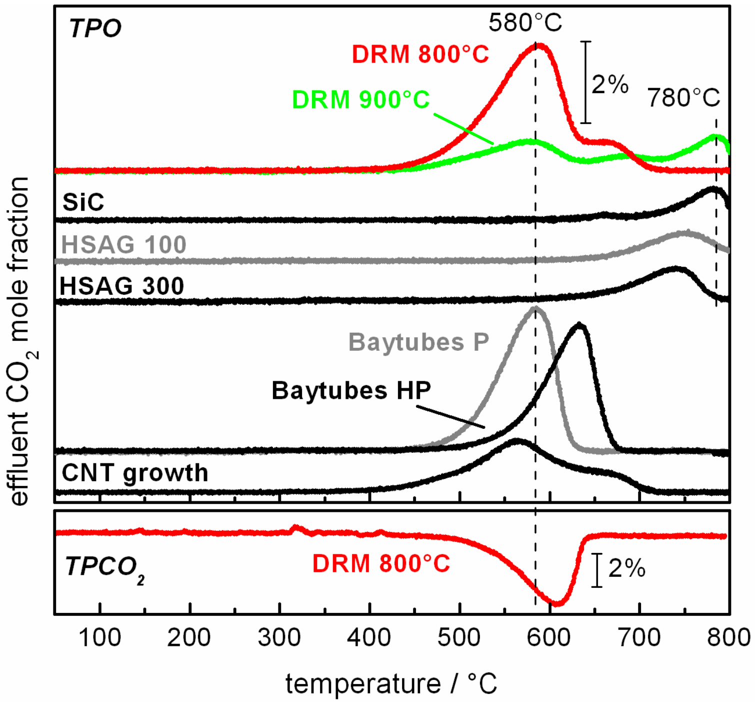

Figure 4.9 TPO profiles of 50 mol% Ni after DRM at 800 °C and 900 °C, SiC after 10 h of DRM at 900 °C, following the CNT growth experiment using the 50 mol% Ni catalyst, and commercially available carbon for the assignment of the TPO peaks. The effluent mole fractions of CO_2 were detected while heating with a rate of 5 °C min^{-1} up to 800 °C in a total flow of 40 Nml min^{-1} of 4.5% O_2 in Ar (top) or 10% CO_2 in Ar (bottom).

To clarify the correlation between the different carbon species detected by TEM and the TPO peaks, TPO experiments after a blank experiment, a CNF growth experiment, and TPO experiments with commercially available carbon reference materials were carried out. After the DRM blank experiment, only one peak at T_{max} = 760 °C was observed during the subsequent TPO (Figure 4.9). For the HSAG samples with different surface areas, it was found that these metal-free graphite powders showed burn-off temperatures higher than 700 °C, which increased with decreasing surface area (Figure 4.9). These observations are in good agreement with results obtained by Gaur et al. [43] and Serrano-Lotina et al. [44], who found burn-off temperatures of graphite at temperatures higher than 675 °C. Thus, the high-temperature TPO peak found after the DRM blank experiment is assigned to graphite on the diluent originating from methane pyrolysis.

Furthermore, TPO experiments with commercially available CNFs showed a strong influence of the residual amount of the metallic growth catalyst on the oxidation kinetics (Figure 4.9). The metal residues in Baytubes C70 P lowered the burn-off temperature by 50 °C from 630 °C to 580 °C, and the same trend was found by Becker et al. [45]. A TPO profile after a CNT growth experiment using the 50 mol% Ni catalyst showed a clear peak at 580 °C with a shoulder at higher temperatures (Figure 4.9). This burn-off temperature is in very good agreement with the TPO profile of metal-containing CNFs. Therefore, the peak at 580 °C originates from the catalyzed total oxidation of CNFs.

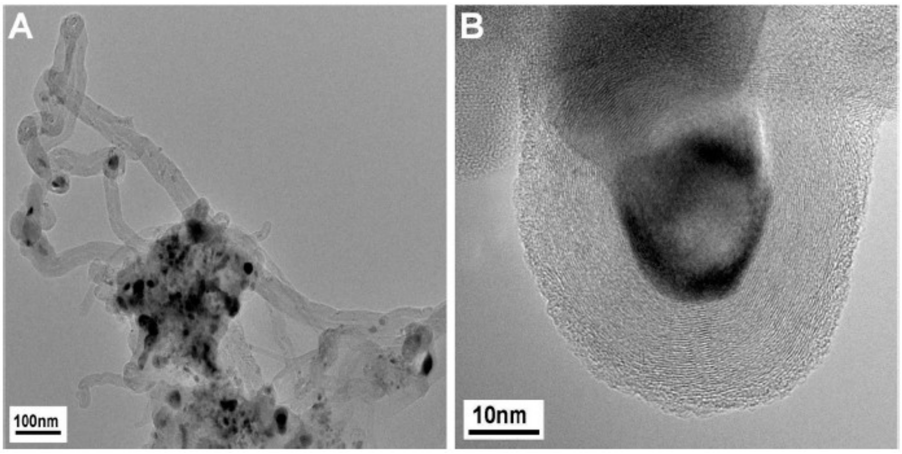

Figure 4.10 TEM micrographs after the CNT growth experiment using the 50 mol% Ni catalyst in a flow of 32 Nml min^{-1} CH_4 and 68 Nml min^{-1} H_2 at 680 °C. CNTs (A, left) and graphite encapsulating Ni particles (B, right).

Additionally, the TEM micrographs of the sample used in the CNF growth experiment showed that in addition to CNFs, graphite-encapsulated Ni particles were formed in low amounts during the growth experiment (Figure 4.10). On the basis of the previous assignment of the peak at 580 °C to the catalytic total oxidation of CNFs, these encapsulating graphite deposits should cause the shoulder at the high-temperature side (680–700 °C) in the TPO profile after CNT growth and DRM at 800 °C (Figure 4.9). In summary, based on the TEM and TPO results, the peak at 580 °C is assigned to the catalyzed oxidation of CNFs, the peak between 650–690 °C to the removal of encapsulating graphite detected for the catalysts with ≥5 mol% Ni and less ordered graphitic carbon for ≤1 mol% Ni, and the peak at 760 °C to the non-catalyzed oxidation of low-surface area graphite.

4.3.5 Deactivation studies

For the identification of the carbon species that lead to deactivation, the stabilities during DRM were correlated with the subsequent TPO profiles. After a reductive pretreatment with optimized maximum temperatures for 25 and 50 mol% Ni, as previously used during the long-term measurements, the DRM reaction was performed at 900 °C for 1, 10, and 100 h. Thereby, the consecutive formation of the carbon deposits was observed by TPO for both catalysts (Figure 4.11). Initially, CO_2 formation was observed between 500–700 °C, attributed to the removal of CNFs based on the established assignment. When performing the reaction for 10 and 100 h, the formation of graphite based on the pyrolysis of CH_4 took place to a larger extent. The formation of the pyrolytic graphite was much more pronounced during the long-term measurements than the formation of other carbon species without much differences for both catalysts.

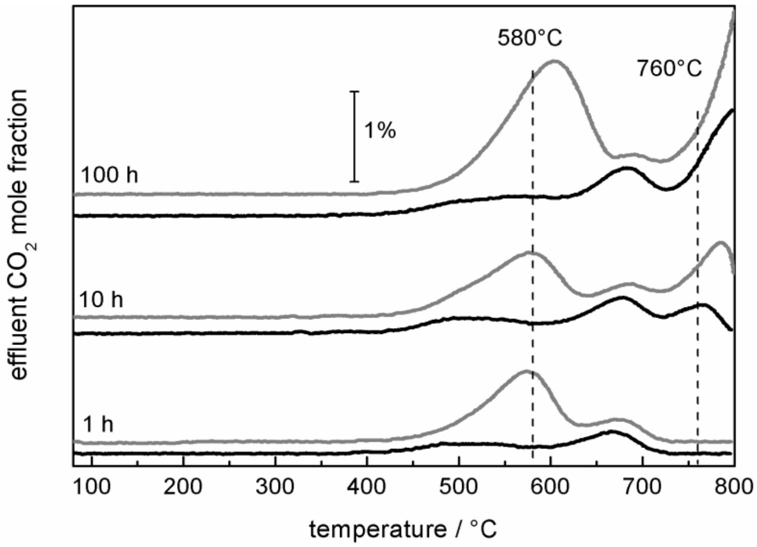

Figure 4.11 TPO profiles after 1, 10, and 100 h of DRM at 900 °C with 25 mol% Ni after T_{Red} = 850 °C (black) and 50 mol% Ni after T_{Red} = 800 °C (grey). The effluent mole fractions of CO_2 were detected while heating with a rate of 5 °C min^{-1} up to 800 °C in a total flow of 40 Nml min^{-1} of 4.5% O_2 in Ar.

The TPO profiles looked nearly identical, but the intensity of the CNF oxidation peak at 580 °C was different (Figure 4.11). For the catalyst with the higher Ni content, the amount of CNFs removed by TPO after 100 h on stream was slightly higher than for the 25 mol% Ni catalyst. During the corresponding DRM measurements, different stabilities were observed as well. The methane conversion after 100 h of DRM compared to the initial one was higher for the 25 mol% Ni catalyst amounting to 98% than the conversion of the highly loaded catalyst with 94%. Furthermore, as already presented in ref. [22] for the 50 mol% Ni catalyst, the CNT peak was dominant in the TPO profile after DRM at 800 °C. The formation of low surface area graphite (TPO peak 760 °C) was only observed during the DRM at 900 °C. In addition, the higher temperature resulted in higher stability in the corresponding DRM experiments. Therefore, graphite originating from methane pyrolysis cannot be the main deactivating carbon species, because it was not formed during the DRM at 800 °C and the amounts of graphite were similar after 100 h on stream for the 25 mol%

and the 50 mol% Ni catalysts at 900 °C. It is reasonable to assume that the formed graphite was not blocking the active Ni sites, but was located on the oxide matrix, the inner reactor wall, the SiC particles or the quartz wool. The major difference in the presented TPO profiles (Figure 4.7) was the amount of CNFs. This observation points to a correlation between the stability during the DRM and the amount of formed CNFs; the higher amount formed at the lower reaction temperature and during 100 h of the DRM at 900 °C suggests that CNFs are the most deactivating carbon species.

4.3.6 Regeneration of the catalyst

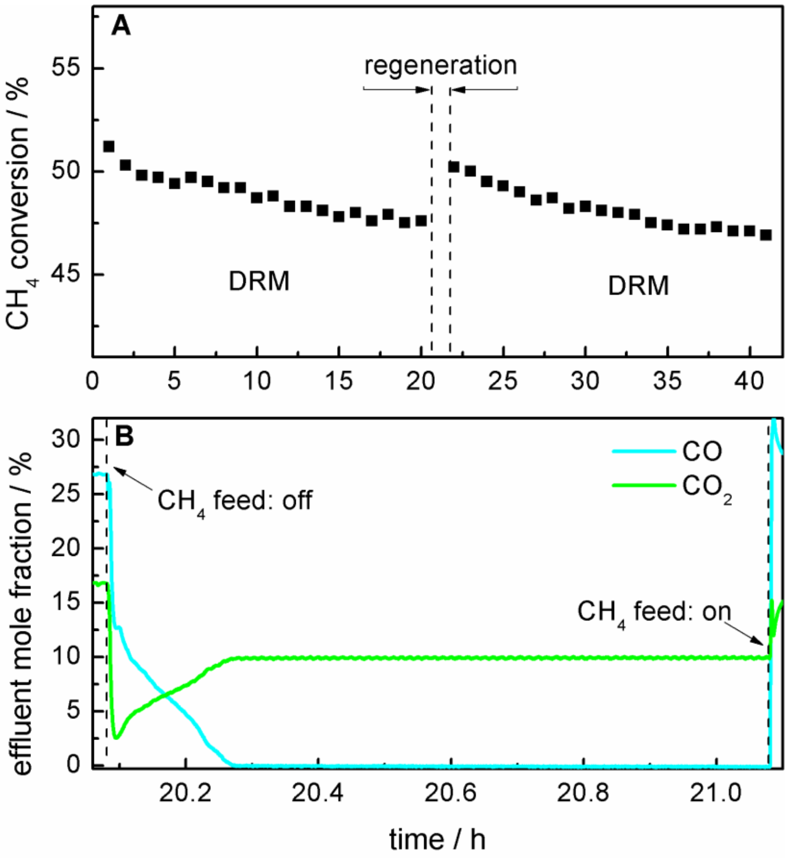

Figure 4.12 Isothermal regeneration with CO_2 of the 50 mol% Ni catalyst during DRM at 800 °C after thermal pre-treatment up to 800 °C. (A) Methane conversion in DRM as a function of time. (B) Effluent mole fractions of CO and CO_2 during the isothermal regeneration with 40 Nml min^{-1} of 10% CO_2 in Ar.

The catalytic DRM activity can be recovered by removing the deposited carbon species, as shown by performing the DRM subsequent to a TPO experiment [22]. Instead of O_2, the carbon species can also be removed by CO_2 according to the Boudouard reaction (eqn (4.3)). A slight shift to higher burn-off temperatures was observed when the TPO experiment was performed with CO_2 instead of O_2 (Figure 4.9, bottom), whereas the effect on the catalytic activity was identical. In addition to the temperature-programmed mode, this regeneration can be performed in an isothermal way at the reaction temperature by changing the feed gas composition to CO_2 and Ar only (Figure 4.12A). The latter can easily be achieved by stopping the feed of methane for 60 min, inducing the removal of carbonaceous deposits by CO formation. After stopping the feed of CH_4, initially a fast drop of the effluent mole fractions of CO and CO_2 was observed. Thereafter, a slight increase in the effluent mole fraction of CO_2 was detected, whereas a slight decrease of CO was observed. After 12 min, no further CO_2 consumption and CO formation was observed, indicating complete removal of the carbonaceous deposits (Figure 4.12B). Subsequent to the removal of carbonaceous deposits, methane can be added again, resulting in an increase in the effluent mole fraction of CO due to the ongoing DRM. After the regeneration, the initial activity is regained due to complete removal of carbonaceous deposits (Figure 4.12A).

4.4 Conclusions

The synthesis of hydrotalcite-like precursors for DRM catalysts is an effective route to obtain highly active and stable catalysts with different Ni contents. These catalysts with efficiently embedded Ni nanoparticles show outstanding stabilities in the high-temperature dry reforming reaction at 900 °C. Measured axial temperature profiles as well as CFD simulations demonstrated the strong influence of the endothermic DRM on the temperature gradient in the catalyst bed. During the reaction, different carbon species were formed, depending on the metal loading and the reaction temperature. At a higher temperature, the formation of non-deactivating graphite originating from methane pyrolysis is enhanced, whereas at lower temperature the formation of CNFs is favored, causing the continuous deactivation with time on stream. It was shown that the carbon species can easily be removed by O_2 and CO_2 either isothermally or using a temperature ramp to reestablish the original methane conversion.

4.5 References

[1] K. Tomishige, M. Nurunnabi, K. Maruyama, K. Kunimori, *Fuel Process. Technol.* **2004**, 85, 1103.

[2] L. Yuliati, H. Yoshida, *Ind. Eng. Chem. Res.* **2008**, 37, 1592.

[3] J. H. Butler, http://www.esrl.noaa.gov/gmd/aggi/.

[4] A. Holmen, *Catal. Today* **2009**, 142, 2.

[5] T. V. Choudhary, V. R. Choudhary, *Angew. Chem., Int. Ed.* **2008**, 47, 1828.

[6] L. Kahle, T. Roussiere, L. Maier, K. H. Delgado, G.Wasserschaff, S. A. Schunk, O. Deutschmann, *Ind. Eng. Chem. Res.* **2013**, 52, 11920.

[7] Z. Jiang, T. Xiao, V. L. Kuznetsov, P. P. Edwards, *Philos. Trans. R. Soc., A* **2010**, 368, 3343.

[8] K. Wang, X. Li, S. Ji, B. Huang, C. Li, *ChemSusChem* **2008**, 1, 527.

[9] V. Havran, M. P. Duduković, C. S. Lo, *Ind. Eng. Chem. Res.* **2011**, 50, 7089.

[10] J. Wei, E. Iglesia, *Ind. Eng. Chem. Res.* **2011**, 50, 7089.

[11] D. Baudouin, U. Rodemerck, F. Krumeich, A. D. Mallmann, K. C. Szeto, H. Ménard, L. Veyre, J. P. Candy, P. B. Webb, C. Thieuleux, C. Copéret, *J. Catal.* **2013**, 297, 27.

[12] T. Wurzel, S. Malcus, L. Mleczko, *Chem. Eng. Sci.* **2000**, 55, 3955.

[13] C. H. Bartholomew, *Appl. Catal., A* **2001**, 212, 17.

[14] D. San José-Alonso, M. J. Illán-Gómez, M. C. Román- Martínez, *Int. J. Hydrogen Energy* **2013**, 38, 2230.

[15] J. Newnham, K. Mantri, M. Amin, J. Tardio, S. Bhargava, *Int. J. Hydrogen Energy* **2012**, 37, 1454.

[16] V. Choudhary, B. Uphade, A. Mamman, *Appl. Catal., A* **1998**, 168, 33.

[17] J. Claridge, A. York, A. J. Brungs, C. Marquez-Alvarez, J. Sloan, S. Chi Tsang, M. L. Green, *J. Catal.* **1998**, 180, 85.

[18] A. I. Tsyganok, T. Tsunoda, S. Hamakawa, K. Suzuki, K. Takehira, T. Hayakawa, *J. Catal.* **2003**, 213, 191.

[19] V. R. Choudhary, A. M. Rajput, *Ind. Eng. Chem. Res*. **1996**, 35, 3934.

[20] A. Horváth, G. Stefler, O. Geszti, A. Kienneman, A. G. L. Pietraszek, *Catal. Today* **2011**, 169, 102.

[21] D. Liu, X. Y. Quek, W. N. Cheo, R. Lau, A. Borgna, Y. Yang, *J. Catal.* **2009**, 266, 380.

[22] K. Mette, S. Kühl, H. Düdder, K. Kähler, A. Tarasov, M. Muhler, M. Behrens, *ChemCatChem* **2014**, 6, 100.

[23] Chemical Energy Storage, ed. R. Schlögl, de Gruyter, Berlin/Boston, **2013**.

[24] K. Kugler, H. F. Niessen, K. A. Theis, *Nucl. Eng. Des.* **1975**, 34, 65.

[25] T. A. Chubb, *Chem. Tech.* **1976**, 6, 654.

[26] G. DeMaria, L. D'Alessio, C. A. Tiberio, *Sol. Energy* **1985**, 35, 409.

[27] J. T. Richardson, S. A. Paripatyadar, *Appl. Catal.* **1990**, 61, 293.

[28] S. Sharma, Z. Hu, P. Zhang, E. McFarland, H. Metiu, *J. Catal.* **2011**, 278, 297.

[29] T. Shishido, M. Sukenobu, H. Morioka, R. Furukawa, H. Shirahase, K. Takehira, *Catal. Lett.* **2001**, 73, 21.

[30] K. Takehira, T. Shishido, P. Wang, T. Kosaka, K. Takaki, *Phys. Chem. Chem. Phys.* **2003**, 5, 3801.

[31] K. Takehira, T. Shishido, P. Wang, T. Kosaka, K. Takaki, *J. Catal.* **2004**, 221, 43.

[32] K. Takehira, T. Shishido, D. Shouro, K. Murakami, M. Honda, T. Kawabata, K. Takaki, *Appl. Catal., A* **2005**, 279, 41.

[33] K. Takehira, T. Kawabata, T. Shishido, K. Murakami, T. Ohi, D. Shoro, M. Honda, K. Takaki, *J. Catal.* **2005**, 231, 92.

[34] O. W. Perez-Lopez, A. Senger, N. R. Marcilio, M. A. Lansarin, *Appl. Catal., A* **2006**, 303, 234.

[35] M. Fadoni, L. Lucarelli, *Stud. Surf. Sci. Catal.* **1999**, 123, 289.

[36] O. F. Schlüter, B. I. Wehner, D. Hu, W. Xia, T. Quandt, G. Marginean, W. Brandl, M. Muhler, *Appl. Catal., A* **2004**, 274, 71.

[37] M. Nijemeisland, A. G. Dixon, E. H. Stitt, *AIChE J.* **2004**, 50, 906.

[38] H. P. Calis, J. Nijenhuis, B. C. Paikert, F. M. Dautzenberg, D. M. van den Bleek, *Chem. Eng. Sci.* **2001**, 56, 1713.

[39] H. A. Jakobsen, H. Lindbor, V. Handeland, *Comput. Chem. Eng.* **2002**, 26, 333.

[40] X. Gao, Y. P. Zhu, Z. H. Luo, *Chem. Eng. Sci.* **2011**, 66, 6028.

[41] S. S. Elnashaie, S. S. Elshishini, *Chem. Eng. Sci.* **1993**, 48, 567.

[42] D. A. Monti, A. Baiker, *J. Catal.* **1983**, 83, 323.

[43] S. Gaur, D. J. Haynes, J. J. Spivey, *Appl. Catal., A* **2011**, 403, 142.

[44] A. Serrano-Lotina, L. Rodríguez, G. Muñoz, A. J. Martin, M. A. Folgado, L. Daza, *Catal. Commun.* **2011**, 12, 961.

[45] M. J. Becker, W. Xia, J. P. Tessonnier, R. Blume, L. D. Yao, R. Schlögl, M. Muhler, *Carbon* **2011**, 49, 5253.

5 Redox dynamics of Ni catalysts in CO_2 reforming of methane

Katharina Mette, Stefanie Kühl, Andrey Tarasov, Hendrik Düdder, Kevin Kähler, Martin Muhler, Robert Schlögl, Malte Behrens

Abstract

The influence of redox dynamics of a Ni/MgAl oxide catalyst for dry reforming of methane (DRM) at high temperature was studied to correlate structural stability with catalytic activity and coking propensity. Structural aging of the catalyst was simulated by repeated temperature-programmed reduction/oxidation (TPR/TPO) cycles. Despite a very high Ni loading of 55.4 wt%, small Ni nanoparticles of 11 nm were obtained from a hydrotalcite-like precursor with a homogeneous distribution. Redox cycling gradually changed the interaction of the active Ni phase with the oxide support resulting in a crystalline Ni/$MgAl_2O_4$-type catalyst. After cycling the average particle size increased from 11 to 21 nm – while still a large fraction of small particles was present – bringing about a decrease in Ni surface area of 72%. Interestingly, the redox dynamics and its strong structural and chemical consequences were found to have only a moderate influence on the activity in DRM at 900 °C, but lead to a stable attenuation of carbon formation due to a lower fraction of graphitic carbon after DRM in a fixed-bed reactor. Supplementary DRM experiments in a thermobalance revealed that coke formation as a continuous process until a carbon limit is reached and confirmed a higher coking rate for the cycled catalyst.

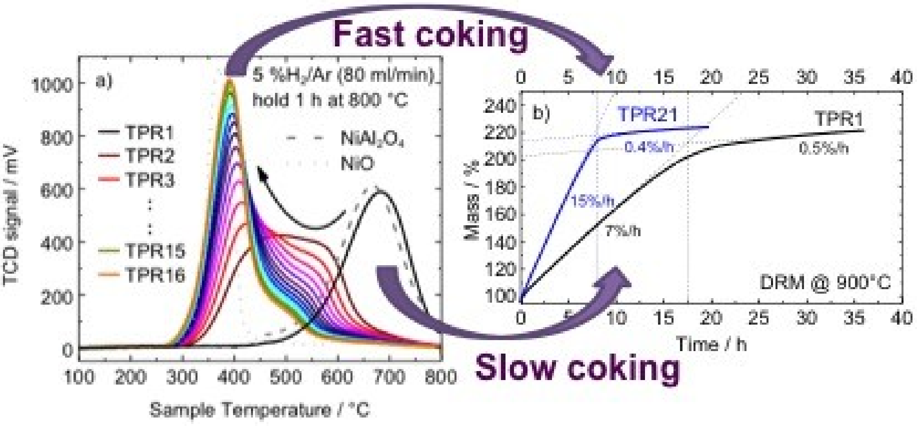

5.1 Introduction

Fossil power generations emit large amounts of the greenhouse gas CO_2 [1,2]. For the energetic utilization of anthropogenic CO_2, dry reforming of methane (DRM, Eq. (5.1)) is an interesting option to convert these two greenhouse gases into syngas (CO/H_2 mixtures) [3]. DRM can be integrated in the well-established downstream syngas chemistry leading to synthetic fuels like alcohols or hydro-carbons [4]. Reforming with CO_2, rather than steam reforming with H_2O yields syngas with lower H_2/CO ratios, which is especially attractive for oxo synthesis (hydroformylation) of aldehydes from alkenes and possibly also for Fischer–Tropsch synthesis of long-chain hydrocarbons [5,6].

Apart from expensive noble metals, abundant nickel based catalysts are known to be highly active in the dry reforming reaction, but suffer from fast deactivation by coking [7,8] that can even lead to reactor blocking. Carbon deposition originates mainly from the exothermic Boudouard reaction (Eq. (5.2)) or from methane decomposition (Eq. (5.3)). Additionally, a deviation from the expected $CO:H_2$ ratio of 1:1 composition is usually observed due to the reverse water gas shift reaction (Eq. (5.4)). We have recently reported that mitigation of coking over a Ni-based catalyst is possible by operating the reaction at elevated temperatures of 900 °C [9].This effect is likely due to the thermodynamic suppression of the Boudouard reaction at such high reaction temperature. Thus, operation at high temperature might be an attractive option for the application of cheap Ni-based catalysts for the DRM reaction.

$$CO_2+CH_4 \rightarrow 2\ CO+2\ H_2 \qquad \Delta H_{298} = 247\ \text{kJ mol}^{-1} \tag{5.1}$$

$$CO \rightarrow CO_2+C \qquad \Delta H_{298} = -172\ \text{kJ mol}^{-1} \tag{5.2}$$

$$CH_4 \rightarrow C+2\ H_2 \qquad \Delta H_{298} = 75\ \text{kJ mol}^{-1} \tag{5.3}$$

$$CO_2+H_2 \rightarrow CO+H_2O \qquad \Delta H_{298} = 41\ \text{kJ mol}^{-1} \tag{5.4}$$

While Ni-based catalysts are extensively studied in this reaction [10,11], most reports have looked at reaction temperatures up to around 800 °C. It is thus desirable to learn more about the coking behavior, the structural and catalytic stability at higher temperature where only limited information is available in the literature.

Several attempts have been made to suppress coke formation on Ni catalysts using different supports. The addition of basic promoters such as CaO or MgO to Ni/Al_2O_3 catalysts can increase the activity and reduce carbon formation [12,13]. The Lewis basicity of these promoters enhances the chemisorption of CO_2 [14], a characteristic that is proposed to reduce the Boudouard reaction by shifting the equilibrium toward CO. The relation of carbon deposition and the catalyst structure was studied by Chen and Ren [15] for a Ni/Al_2O_3 catalyst. They reported on the influence of strong $Ni-Al_2O_3$ interactions on the catalytic properties during DRM. The formation of a $NiAl_2O_4$ spinel was found to have a suppressing effect on the carbon formation. Furthermore, the reduction of $NiAl_2O_4$ compared to NiO results in smaller Ni crystallites [16].

In this work we present an attempt to relate structural stability and redox dynamics of a Ni catalyst with its coking propensity. The catalyst under study contains 55.4 wt.% Ni supported on a mixed Mg, Al oxide that was obtained from a co-precipitated hydrotalcite-like precursor as described in a previous report [9]. The structural and redox stability of the catalyst was tested by subjecting the precursor either to only one calcination and reduction treatment or to multiple TPR/TPO cycles. It has been recently shown that the calcination conditions can have substantial effects on the catalytic performance of $Ni/La_2O_3–ZrO_2$ catalysts in the low-temperature DRM reaction [17]. On Ni/Al_2O_3 catalysts, Guilhaume et al. [18] have observed significant structural and chemical changes of Ni/Al_2O_3 catalysts as a consequence of such redox cycling. They found, that Ni is initially incorporated in a spinel phase formed with the support and that redox cycling at low temperatures progressively extracts metallic Ni from the spinel-type structure. While their catalysts were tested in sequential cracking of acetic acid, we have tested our materials for their DRM activity and coke formation rates in a tubular plug-flow reactor and in a magnetic suspension thermobalance. With this approach the effect of structural ageing as simulated by repeated TPR/TPO cycles can be decoupled from the structural effect induced by coking, e.g. by enhanced metal mobility during carbon filament growth.

5.2 Results and discussion

5.2.1 Catalyst preparation and characterization

We have shown recently [9] that Ni nanoparticles supported on a matrix of Mg and Al oxide can be obtained by the preparation of hydrotalcite-like compounds (htl) as well-defined precursor materials. The resulting catalysts are characterized by a homogeneous metal distribution and very small Ni particles that are embedded and therefore stabilized at high temperatures in a Mg,Al mixed oxide matrix. The catalyst used here was prepared via a hydrotalcite-like (htl) precursor of the nominal composition $Ni_{0.5}Mg_{0.17}Al_{0.33}(OH)_2(CO_3)_{0.17} \cdot mH_2O$. The precursor compound can easily be prepared from metal nitrates in a phase-pure form by pH-controlled co-precipitation [9]. The Ni content of 50 mol% (metal based) corresponds to a 55.4 wt% Ni loading in the final catalyst. The 1:2 ratio of Mg to Al in the oxidic matrix was chosen to enable $MgAl_2O_4$ spinel formation, a sintering-stable ceramic compound. The platelet-like precursor particles provides a specific BET area of 131 $m^2\ g_{cat}^{-1}$. The calcination was performed at 600 °C. We have previously shown that this temperature is sufficient to completely decompose the hydrotalcite-like precursor [9]. The calcination in air leads to an increase to 213 $m^2\ g_{cat}^{-1}$ due to shrinkage of the platelets. The characterization details of the phase-pure precursor and the calcined product are described in our previous study [9].

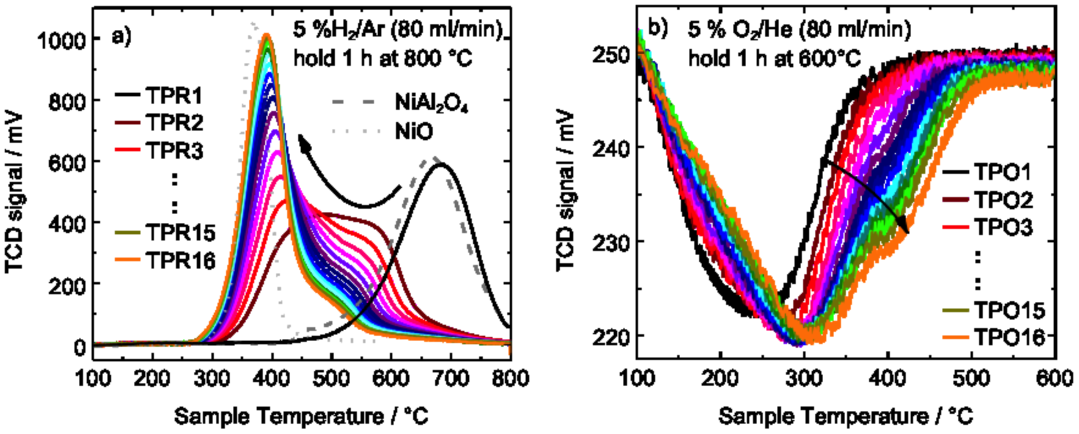

Figure 5.1 TPR cycles of Ni/MgAl oxide catalyst calcined at 600 °C and of $NiAl_2O_4$ (dark grey dashed line) and NiO (light grey dotted line) as references (a); TPO cycles of Ni/MgAl oxide catalyst (b).

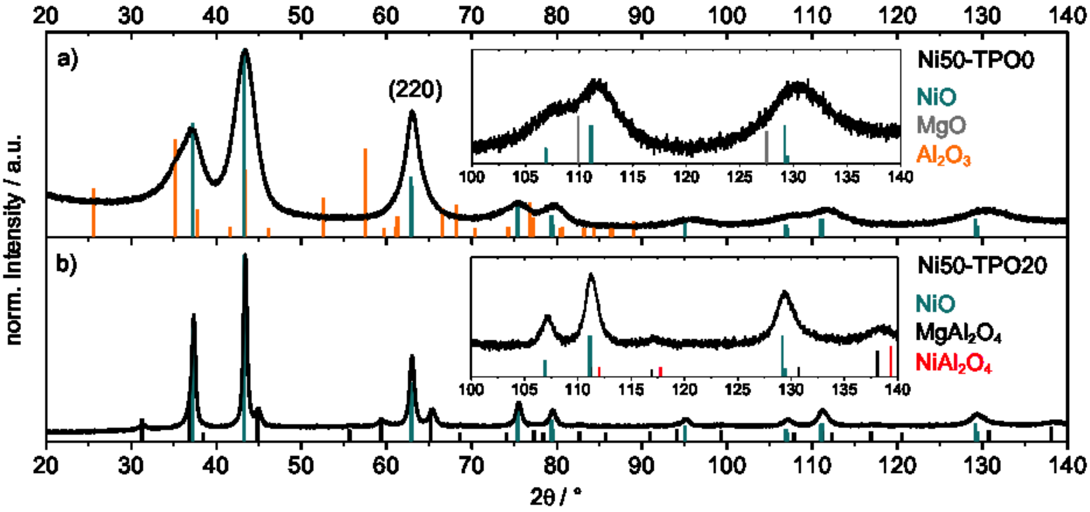

Figure 5.2 Powder XRD patterns of the mixed oxides after 1. Calcination (TPO0) at 600 °C (a), after TPO20 (b), ICDD 44-1159 NiO (blue), ICDD 89-4248 MgO (grey), ICDD 46-1212 Al_2O_3 (orange), ICDD 21-1152 $MgAl_2O_4$ (black), ICDD 10-0339 $NiAl_2O_4$ (red). Inset figures are magnifications of the range from 100 to 140 °2θ.

The reduction behavior of the calcined material has been investigated using TPR. A single broad peak was observed in the temperature range between 450 and 850 °C. The TPR profile reflects a one-stage process with a maximum at 685 °C (Ni50-TPR1, Figure 5.1a). On the basis of the TPR profile with a peak maximum around 700 °C a reduction temperature of 800 °C was chosen for the following experiments. At this temperature the reduction of Ni will be complete after a subsequent holding period of 1 h. The catalyst obtained after reduction at 800 °C is labeled Ni50-TPR1 in this study. It is characterized by small Ni particles of 11 nm, which are partially embedded in an oxide matrix with a high specific Ni surface area of 25 m^2 g_{cat}^{-1} (Table 5.1, Figure 5.3) [9]. The elemental distribution (Figure 5.6a), determined by TEM-EDX at different locations is rather homogeneous and the average molar composition is close to the nominal values (Ni/Mg/Al: 57/14/30 (±5); nominal 50/17/33).

Table 5.1 Composition and particle sizes of the reduced samples determined by TEM and H_2 chemisorption.

Sample label	Particle size distribution[a] / nm			Ni SA[d] / m^2 g_{cat}^{-1}	Ni Dispersion[d] / %
	PS dn[b]	Median d_{50}	PS dv[c]		
Ni50-TPR1	10.4 ± 3.2 (St.D.)	10.4	11.4	25.0	6.8
Ni50-TPR2	-	-	-	20.5	5.6
Ni50-TPR3	-	-	-	14.3	3.9
Ni50-TPR18	-	-	-	7.0	1.9
Ni50-TPR21	13.4 ± 10.1 (St.D.)	10.3	21.0	-	-

[a] determined by TEM
[b] number-weighted mean particle size
[c] volume-weighted mean particle size
[d] measured with H_2 pulse chemisorption

A comparison of the TPR profile with the reduction profile of a $NiAl_2O_4$ reference material, suggests on a first sight the presence of Ni^{2+} in a$NiAl_2O_4$ phase formed during the first calcination (TPO0). However, the corresponding XRD pattern revealed the presence of a rock salt-type oxide MO (M = Ni, Mg) and a small fraction of Al_2O_3 (Figure 5.2a). The reflexes in general are relatively broad indicating a low crystallinity. An unambiguous discrimination of NiO and MgO is difficult due to very similar lattice constants and the low crystallinity of the obtained material. Though, the presence of NiO seems more likely regarding higher angles > 100° 2θ, where the differences are more distinct due to the widening of the d-space (see inset Figure 5.2a).Thus, although the formation of $NiAl_2O_4$ in nickel/alumina catalysts during oxidation is reported in many publications [16,19,20,21,22], our catalyst might be better described as a NiO phase that is strongly interacting with the oxide matrix. Based on XRD, a spinel phase seems to be absent or X-ray amorphous, as no peaks corresponding to $MgAl_2O_4$ or $NiAl_2O_4$ are detectable (Figure 5.2a). However, the interpretation of the XRD results is usually difficult. Zieliński [16] suggested that the nickel oxide particles are covered by a tight nickel aluminate layer, which determines the reduction behavior while large particles of pure NiO covered by the nickel aluminate layer can be seen in XRD as NiO. This would explain the spinel-like character of the TPR1 profile with simultaneous absence of $NiAl_2O_4$ in the XRD. It has been shown, that higher calcination temperature and longer calcination time increases the metal-support interaction and the fraction of nickel aluminates, resulting in a higher reduction temperature compared to free nickel oxide and increased crystallinity [9,16].

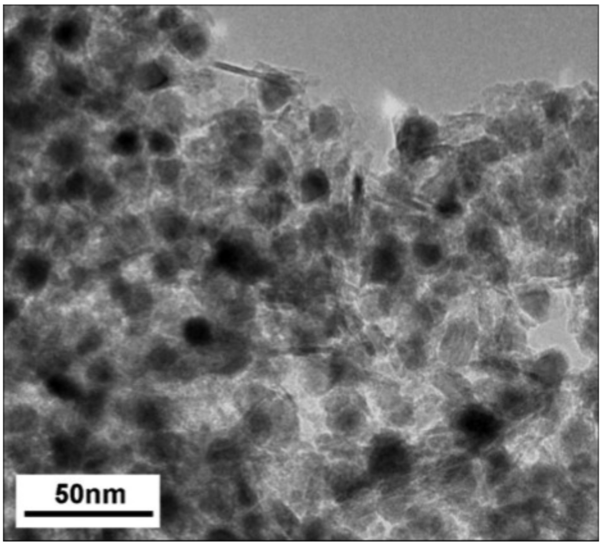

Figure 5.3 TEM micrographs of reduced Ni50-TPR1 catalyst agglomerate with Ni particles in oxidic matrix.

5.2.2 TPR/TPO cycling

To investigate the influence of redox cycling on the structural properties and on the catalytic performance of the catalyst in detail, consecutive TPR/TPO experiments were conducted. The TPRs were performed up to 800 °C, the TPOs up to 600 °C, analogous to the calcination process. This procedure was repeated several times and the results are presented in Figure 5.1. The TPR experiments of the calcined or reoxidized Ni50 catalyst are labeled TPR*n*, where *n* is the number of cycles, and the corresponding samples are named Ni50-TPR*n*. Accordingly, the reoxidation profiles are labeled TPO*n*, with *n* as the number of cycles, and the corresponding sample are denoted Ni50-TPO*n*.

During the redox cycles the TPR profile markedly changed (Figure 5.1a), whereas the total amount of H_2 consumed remained constant and corresponds to a reduction degree of 98% of the NiO. The temperature of maximum hydrogen consumption shifted from 685 °C to 392 °C. Although slight changes might still be present, we consider the system as stable after 16 cycles. Comparison of the profile of TPR16 with the profile of an unsupported NiO reference shows a clear agreement, except for the slowly vanishing shoulder at higher temperatures. We conclude that the (final) Ni phase after 16 reduction–reoxidation cycles consist primarily of NiO. Thus, redox cycling under the applied conditions causes the gradually transition from a strongly interacting "$NiAl_2O_4$-like" into a NiO-like phase with considerably lower interaction to the support. Changes are also observed in the corresponding TPO profiles during reoxidation (Figure 5.1b). Starting from a single broad peak at 220 °C, the peak maximum is shifted upward to 313 °C with an arising shoulder at higher temperatures. The still slightly "bimodal" profiles after the cycling (TPR16 and TPO16) suggest the presence of more than one Ni phases, with the above-mentioned NiO being the dominant one. We note that the different nature of the catalytic materials used in calcination and TPO – a well dispersed hydrotalcite on the one hand and metallic Ni^0 dispersed on the oxide on the other hand – needs to be considered as the activity of Ni0toward the support oxide is different in the two cases. In the second case, the kinetics of the"$NiAl_2O_4$-like" formation is expected to be slower and the NiO-like phase might be kinetically stabilized.

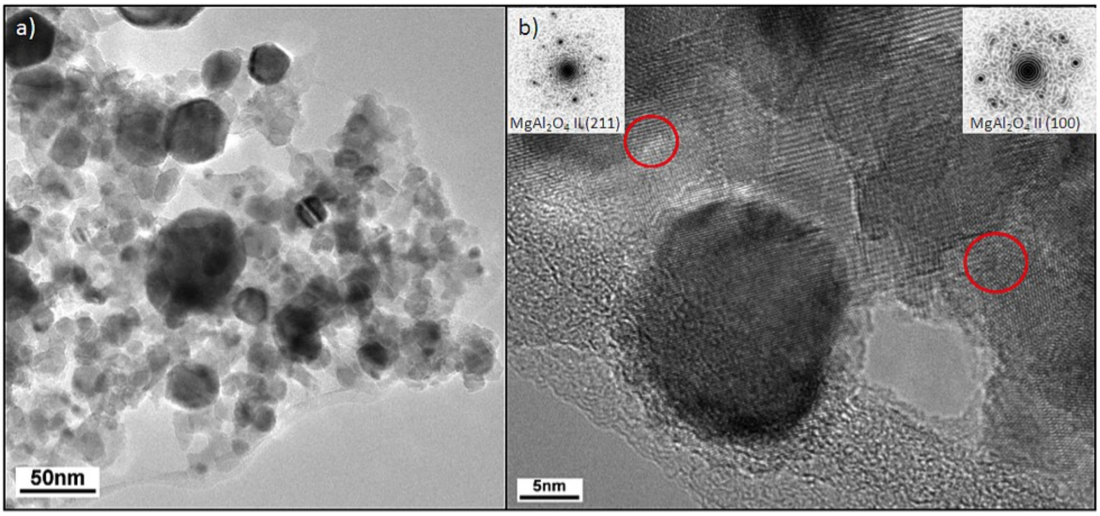

Figure 5.4 TEM micrographs of 21 times redox cycled sample, Ni50-TPR21; a) catalyst agglomerate with sintered Ni particles, b) Ni nanoparticle in crystalline matrix. Insets are showing the power spectra of selected marked areas of the $MgAl_2O_4$ matrix.

After the 20th TPO run, the corresponding XRD pattern revealed an increase in crystallinity of the material in comparison to the primary calcined sample, as suggested by more narrow reflections (TPO20, Figure 5.2b). The sample can be identified as mainly NiO, which is in agreement with the TPR experiments. The major difference to Ni50-TPO1 is the presence of a spinel phase, which is presumably $MgAl_2O_4$. It is noted that an unambiguous assignment of the spinel phase is not possible by XRD, due to similar lattice constants of $NiAl_2O_4$ and $MgAl_2O_4$ and the still relatively low crystallinity.

The average molar composition of Ni50-TPR21, as determined by TEM-EDX, is still close to the nominal values (Ni/Mg/Al: 52/16/31(±5); nominal 50/17/33). However, the elemental distribution determined at different locations is not homogeneous anymore. The Ni content is strongly fluctuating (Figure 5.6b), while the local Mg:Al ratios stays constant at approximately 1:2 in agreement with the formation of $MgAl_2O_4$. This observation indicates that the NiO and the $MgAl_2O_4$ phase segregated as a result of redox cycling as is also suggested by XRD.

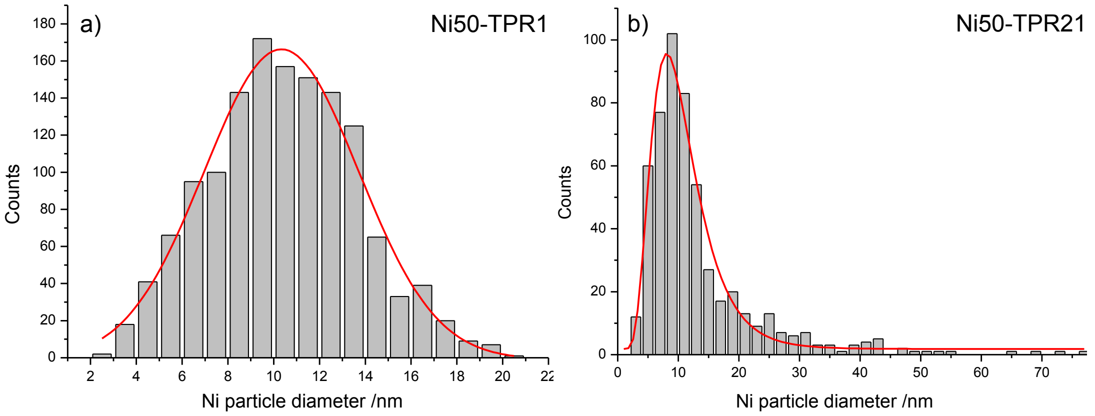

Figure 5.5 Particle size distributions of Ni50-TPR1 (Gauss distribution) (a) and Ni50-TPR21 (log-normal distribution) (b).

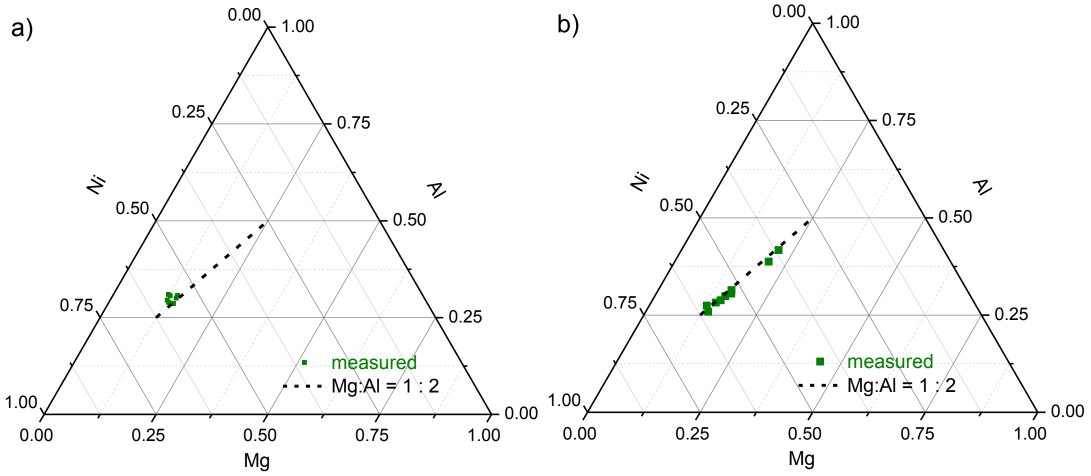

Figure 5.6 TEM-EDX elemental Ni,Mg,Al distributions of Ni50-TPR1 (a) and Ni50-TPR21 (b).

TEM and H_2 pulse chemisorption measurements were performed to estimate the dispersion and size of the metallic Ni particles after redox cycling. The structural changes and the thermal stress during cycling result in a significant decrease in Ni surface area and Ni dispersion. The metallic Ni surface area shrinks from 25 for Ni50-TPR1 to 7 $m^2\ g_{cat}^{-1}$ for

Ni50-TPR18 (Table 5.1). This loss of surface area is also reflected in the TEM images where some sintered Ni particles were observed (Figure 5.4a). However, a statistical evaluation of the particle sizes revealed that the average particle size (arithmetic mean) increased only slightly to 13.4 nm (Table 5.1) compared to Ni50-TPR1, while the median particle size d_{50} (the diameter where 50% of the measured particles are below/above) even remained constant. However, the size distribution is substantially skewed to larger sizes because of sintering, which is described by the log-normal distribution (Figure 5.5b). Accordingly, the volume-weighted mean Ni particle size, which is more sensitive to the presence of larger particles, increased to 21.0 nm (Table 5.1). Ni50-TPR1 on the other hand is characterized by a quite narrow size distribution, as described by the Gauss function (Figure 5.5a). Hence, the volume-weighted mean Ni particle size is only slightly larger than the arithmetic one in this sample. The presence of crystalline $MgAl_2O_4$ is proven from power spectra evaluation of selected areas of the matrix in TEM images (Figure 5.4b). In summary, the structural ageing of the Ni50 catalyst upon redox cycling leads to lower dispersion and sintering of the Ni particles produced by reduction. This effect is accompanied by crystallization of the oxide matrix into$MgAl_2O_4$. In the resulting stable Ni/$MgAl_2O_4$ catalyst the interaction of the redox-active Ni phase to the crystalline support is lower than in the starting material as indicated by the lower temperature of the TPR signal. This lower interaction with the crystalline support is likely the origin of a higher particle mobility leading to sintering at high temperature.

5.2.3 Catalytic properties and coking behavior

The effect of the microstructural changes upon redox cycling on the catalytic performance of the fresh catalyst Ni50-TPO0 and of the catalyst Ni50-TPO18 after 18 TPRO cycles was investigated in the dry reforming of methane (DRM) in a tubular reactor. After a reduction up to 800 °C in 4% H_2 in Ar, DRM was performed at an oven temperature of 900 °C for 10 h time on stream with a CO_2/CH_4 feed ratio of 1.25 at atmospheric pressure. According to Gadalla et al. [5] the temperature limit for carbon deposition increases as the CO_2/CH_4 feed ratio decreases and the slight excess of CO_2 is chosen to reduce coke formation. The degree of methane conversion is given after 1 and after 10 h. The "fresh" catalyst (equivalent to Ni50-TPR1) performs stably over 10 h with a high degree of methane conversion of 76% (Table 5.2, Figure 5.7a). Even in a long-term experiment of 100 h on stream that we published earlier, the catalyst showed a remarkable stable activity at 900 °C, still achieving 94% of the initial CH_4 conversion at the end of the measurement [9]. This is attributed to the stabilizing effect of the oxide matrix. Even though the number of surface metal sites is reduced drastically, the catalytic test of the 19 times TPR/TPO cycled catalyst (equivalent toNi50-TPR19) resulted in a slightly higher degree of conversion of 79% with a likewise stable performance over 10 h (Table 5.2, Figure 5.7a). A non-linear relationship of dispersion and catalytic performance has also been reported for other supported Ni catalysts in the DRM reaction [17]. It is noted however that the temperature of the catalyst bed was 735 °C for Ni50-TPR1 and 760 °C for Ni50-TPR19 indicating stronger heat consumption due to the endothermic reaction over the former material. Thus, the observed conversions should not be used for a direct comparison of rates. It is noted that the bed temperatures however were stable during the 10 h experiment indicating stability of the activity for both catalysts.

Table 5.2 Catalytic test results for the Ni/MgAl oxide catalysts for the dry reforming of methane at a furnace temperature of 900 °C and characteristics of spent catalysts.

Sample label	Metal sites[a] / µmol g_{cat}^{-1}	X_{CH_4} (1h) / %	X_{CH_4} (10h) / %	CO_2 formation[b] / mmol g_{cat}^{-1}	C formation[c] / mmol g_{cat}^{-1}
Ni50-TPR1	639	76	76	54	51
Ni50-TPR19	179	79	79	45	98[d]

[a] measured with H_2 pulse chemisorption
[b] measured by TPO after 10 h DRM at T_{oven} = 900 °C in a fixed-bed reactor
[c] measured in a thermobalance after 10h DRM at 900 °C
[d] investigated sample: Ni50-TPR21

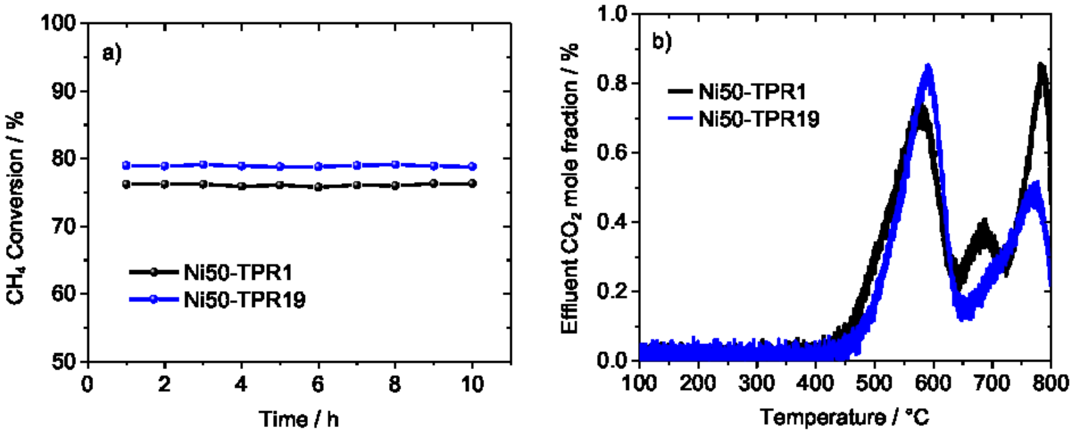

Figure 5.7 DRM at Toven = 900 °C: CH_4 conversion after first reduction and after 18 TPR/TPO cycles (a); TPO profiles of catalysts after 10 h TOS. Effluent mole fractions of CO_2 were detected while heating with 5 K min^{-1} in 4.5% O_2/Ar (b).

In summary, the effect of redox cycling leads to a higher effective bed temperature for the sintered catalyst at otherwise similar conversion. Thus, the significant difference in accessible metal sites between the two catalysts is likely reflected in a lower DRM rate leading to a less efficient self-cooling of the catalyst. Both catalysts performed equally stable over 10 h.

The formation of carbon species on the catalysts during DRM was quantitatively and qualitatively detected by different *in situ* characterization methods, such as TPO and thermogravimetry as well as *ex situ* by TEM. In TPO experiments performed subsequent to DRM, the carbon deposits are oxidized to CO_2 in an O_2-containing feed. Partial oxidation to CO was not observed. Therefore, the amount of CO_2 formed is a measure of deposited carbon on the catalyst. Although the formation of carbonates on the support cannot be excluded and their decomposition can interfere with the CO_2 signal, their potential contribution to the TPO profiles is neglected in the following analysis, because the reaction was followed by a holding period of 10 min at high temperature and cooling in Ar flow for 2.5 h. During this treatment, hypothetical carbonates are likely to decompose. Despite the similar conversion, the amount of carbon is 54 mmol g_{cat}^{-1} on Ni50-TPR1 and only 45 mmol g_{cat}^{-1} on Ni50-TPR19 (Table 5.2). This difference might also be affected by the divergent effective bed temperatures, which thermodynamically can result in a lower amount of carbon at a higher temperature. The corresponding TPO profiles are shown in Figure 5.7b. On Ni50-TPR1, three distinct peaks are distinguishable at 574, 688 and 781 °C, referring to different carbon species. On Ni50-TPR19, the TPO profile displays the presence of only two distinct carbon species at 591 and 776 °C, the latter showing a pronounced shoulder to lower temperatures.

Düdder et al. [23] performed TPO experiments of carbonaceous reference materials. Referring to their results, we assign the low temperature peak to carbon filaments, whereas the high temperature peak fits well with the oxidation of high surface area graphite (HSAG). The origin of the small peak in the middle might be assigned to the oxidation of less ordered carbon. Hence, a similar amount of carbon fibers are formed after DRM on both catalysts, but the amount of graphitic carbon, that is thought to originate from methane pyrolysis [9], was significantly reduced by the redox cycling treatment.

The presence of different amounts and types of carbon obtained was also seen in the TEM analysis of the spent catalysts. After DRM of Ni50-TPR1 the initial catalyst morphology is partially still preserved, but the Ni particles are sintered to some extent under working conditions (Figure 5.8a). In agreement with the TPO results, at least two different carbon species can be found in the TEM micrographs in Figure 5.8: graphitic carbon layers with and without inclusions of Ni particles (b) and tubular carbon nanofibers (c). Similar results were obtained for the redox cycled catalyst Ni50-TPR19 (Figure 5.9a), which is also characterized by graphitic as well as filamentous carbon after DRM (Figure 5.9b and d). In addition to these species, carbon onions with isolated Ni particles were found (Figure 5.9c). All images indicate significant mobility of a fraction of the Ni particles resulting in detachment from the supporting oxide matrix during formation of carbon fibers ("tip growth"). It is noted that carbon exhibits a significant solubility in Ni at high temperatures [24,25].Thus, the graphitic onion-like carbon species might have formed by segregation during cooling of a solid Ni–C solution that can form under steady state conditions [26]. The growth mode of carbon on Ni also depends on the particle size. Only small enough particles, which are present in both catalysts, will favor fiber or tube growth, while highly ordered graphene growth and graphite crystallization was observed predominantly on Ni(111) terraces [27] that can be expected to a greater extent on larger particles. According to these considerations, a design goal for high-temperature Ni DRM catalysts is the formation of particles that are too large to trigger fiber growth, but at the same time exhibit a low fraction of Ni(111) terraces and/or a blocking of carbon dissolution into the bulk by modifications of the surface, e.g. through steps edge blocking [28] or SMSI-layers, or of the bulk, e.g. by the modified sub-surface chemistry of an intermetallic compound [29,30] or alloy [31].

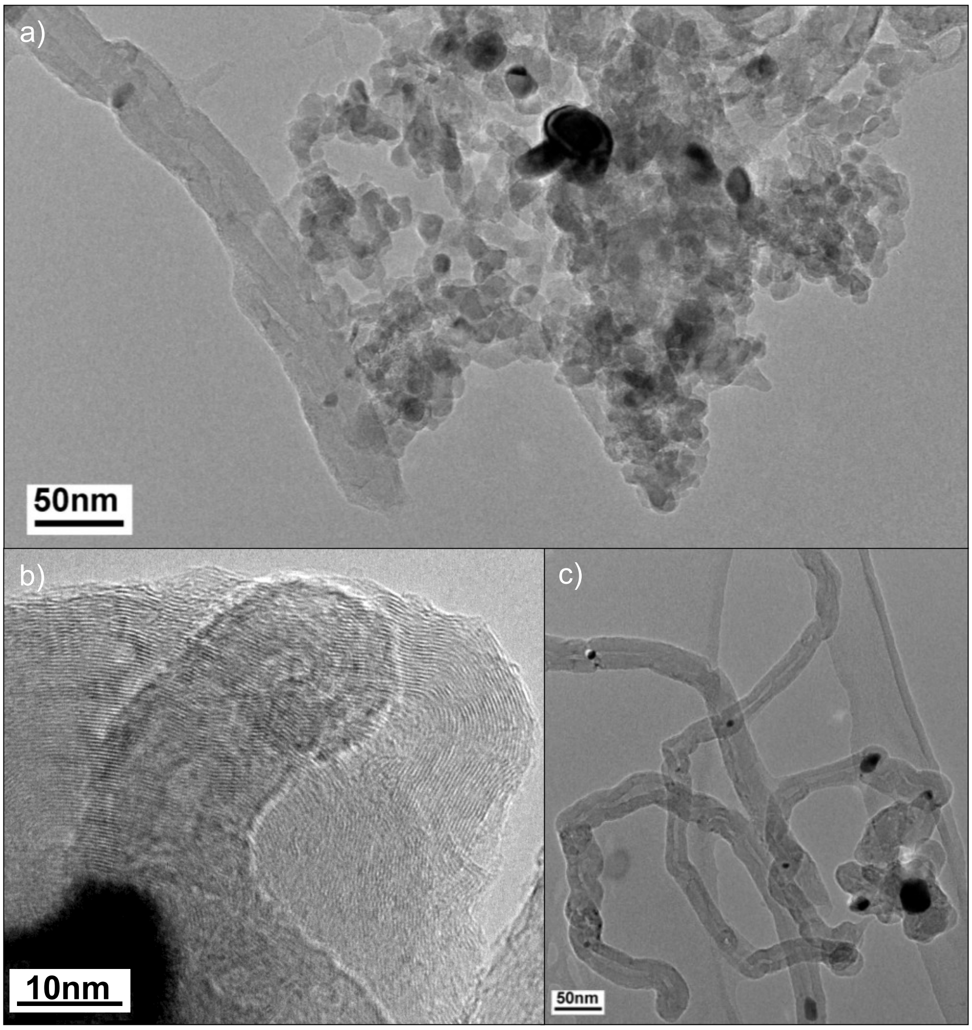

Figure 5.8 TEM micrographs of the spent Ni50-TPR1, run in DRM for 10 h at a reaction temperature of 900 °C: a) catalyst agglomerate, b) Ni particle in graphitic carbon, c) isolated Ni particles in filamentous carbon.

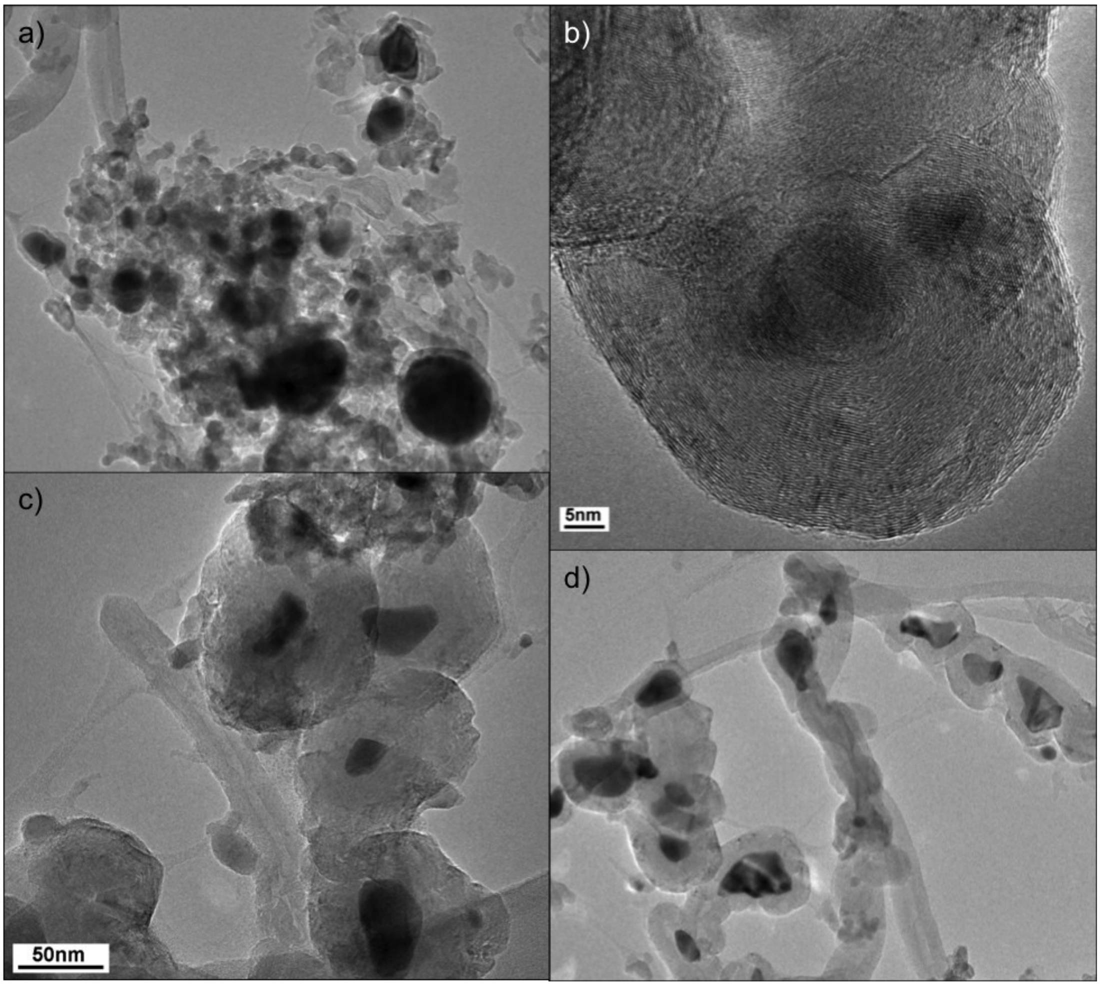

Figure 5.9 TEM micrographs of the spent Ni50-TPR19, run in DRM for 10 h at a reaction temperature of 900 °C: a) catalyst agglomerate, b) Ni particles in graphitic carbon, c) Ni particles in carbon onions, d) Ni particles in filamentous carbon.

Additional to the results obtained in the tubular fixed-bed reactor, the coking kinetics during DRM at $T_{balance}$= 900 °C of the fresh and of the cycled catalyst have been further explored *in situ* in a thermobalance with a vertical geometry (Figure 5.10). As in the tubular reactor, the catalysts have been pre-reduced at 800 °C (Figure 5.10a). The derived mass profiles are in good agreement with the profiles shown during cycling (Figure 5.1a).

The fresh Ni50-TPR1 was compared to a 21 times cycled Ni50-TPR21 catalyst. In both cases an initial continuous weight gain was observed during DRM at 900 °C due to carbon formation (Figure 5.10b). Such an immediate carbon growth without an induction period indicates a rapid saturation of the nickel surface and a prompt nucleation. After 8 h for the redox cycled and after 17.5 h for the fresh catalyst, a sudden leveling of the carbon formation was observed. Afterward, carbon is formed with only 0.4 to 0.5 wt% h^{-1} and a total amount of about 123 wt% carbon was detected for both catalysts. The initial linear formation rate of the carbon deposition was determined to be 7 wt% h^{-1} for Ni50-TPR1 and 15 wt% h^{-1} for

Ni50-TPR21. Thus, the redox cycling resulted in an increased carbon formation rate and an increased total amount of carbon from 51 to 98 mmol g_{cat}^{-1} after 10 h, which is contrary to the observations made in the fixed-bed reactor (Table 5.2). The decrease in coking rate might be caused by a blocked Ni surface due to carbon depositions and sintering. However, CH_4 conversion (Figure 5.10c) and the yield of syngas (Figure 5.10d) were continuously detected in the exhaust gas of the balance by MS. It is noted that a quantitative kinetic evaluation of the MS data is not possible. The large amount of undiluted catalyst, the non-ideal flow conditions and the uncertainties of bed temperature and approach to equilibrium in this experiment do not allow for a reliable catalytic evaluation of activity and stability. Thus, a direct comparability with the experiments in the tubular reactor under much better kinetic control [23] cannot be expected. However, it is noteworthy that the Ni50-TPR21 catalyst seems to be the more active catalyst in the experiment in the thermobalance and shows a higher methane consumption rate. The stability of the catalyst appears to be different in the thermobalance experiment. While both catalysts showed a stable performance over 10 h in the fixed-bed reactor, in the thermobalance the CH_4 consumption rate increases with time as long as carbon is formed (Figure 5.10c). Therefore it can be assumed that carbon is mainly formed by methane pyrolysis. This effect is more pronounced for the Ni50-TPR21 catalyst. Carbon saturation is followed by a slow deactivation. However, in the last about 3 h TOS, the conversion seems almost stable (see insets Figure 5.10c). The H_2 to CO formation ratio (Figure 5.10d) slowly reaches a value of 1.1 after 20 h for both catalysts in the expected regime for DRM.

The DRM test was followed by a TPO for regeneration of the catalysts. The corresponding profiles as well as the detected MS signal of CO_2 are displayed in Figure 5.10e. For both samples, the first weight increase in the TG-TPO profile corresponds to the reoxidation of metallic Ni starting from 250 °C. The subsequent weight decline starting from 450 °C might overlap with the Ni reoxidation and is a result of carbon combustion accompanied by the formation of CO_2. As soon as all CO_2 is evolved the weight increases abruptly around 650 °C. One possible explanation is that next to CO_2, CO is formed during the combustion process. Since CO is a strong reducing agent and can re-reduce the just formed nickel oxide. After all evolved CO is consumed Ni is oxidized again leading to the abrupt weight increase. An alternative explanation is that two different Ni species are present. One readily accessible Ni species that is not covered with carbon and therefore is oxidized first and another isolated Ni species that is enclosed in graphitic carbon onions, as shown in Figure 5.9c. To reoxidize this Ni species, the carbon layers have to be removed first. Due to the higher temperatures this 2nd reoxidation happens faster resulting in the abrupt weight increase. Because the mass loss during the reduction is slightly higher than the overall mass gain during the oxidation, the second explanation is more likely. The distinction between different CO_2 peaks is not possible from these measurements in contrast to the TPO experiments subsequent to activity tests in the fixed-bed reactor. This indicates a diffusion limitation due to the high amount of carbon and a lack of oxygen in the balance. Carbon on Ni50-TPR1 is oxidized at higher temperatures. This is in line with the observation of more thermally stable graphitic carbon in the TPO profiles after DRM in the tubular reactor (Figure 5.7b).

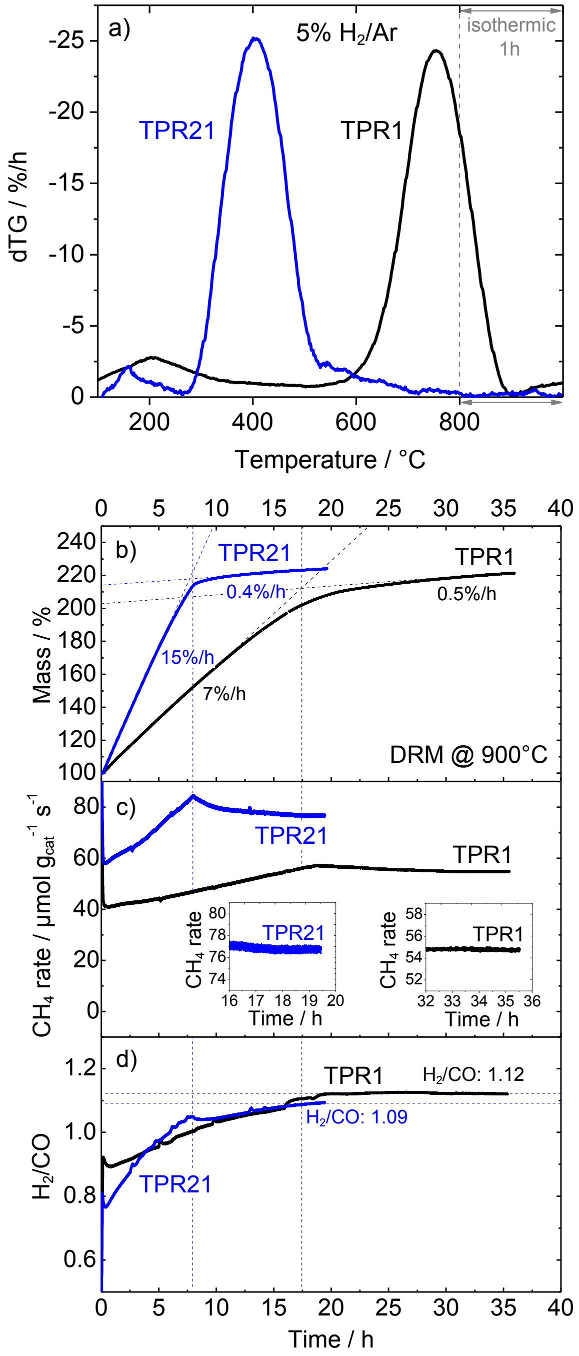

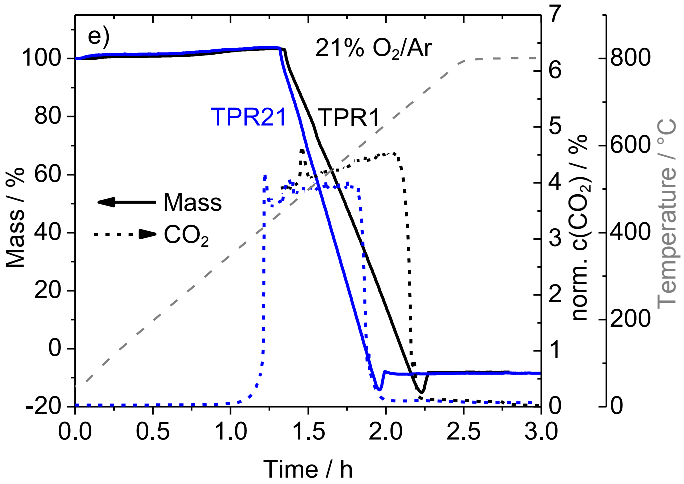

Figure 5.10 DRM in a thermobalance of Ni50-TPR1 and Ni50-TPR21; pre-reduction in 5% H_2/Ar up to 800 °C (a), DRM at 900 °C (b), CH_4 conversion rate during DRM (c), H_2/CO ratios during DRM (d) and subsequent TPO in 21% O_2/Ar (e).

In summary, it was shown that the redox dynamics of the hydrotalcite-derived Ni catalyst have a minor effect on the coking behavior in DRM at high temperatures. While the activity may be increased by the redox cycles, the stability is not affected and a lower amount of graphitic carbon deposits was observed after DRM in a fixed-bed reactor. Whereas, complementary performed thermogravimetric DRM measurements identified a carbon limit, independent of the pretreatment. However, the redox cycled catalyst reached this limit more rapidly. Carbon deposits are likely to be formed by methane pyrolysis, which is an undesired side reaction that is promoted by high reaction temperatures, while the exothermic Boudouard reaction shall be thermodynamically hindered. These results show that even at conditions where pyrolysis is favored, there are kinetic factors due to the catalyst's microstructure that can mitigate this side reaction. In the present case, these microstructural effects can be related to the sintering of the Ni particles, their lower interaction to the support and/or the crystalline nature of the $MgAl_2O_4$ spinel. As the change in the TPR profiles and the XRD patterns was much stronger than that in the Ni particle size distribution, we suspect that this effect might rather be related to changes of the oxide component of the DRM catalyst.

5.3 Conclusion

A methodic approach was presented to address the structural stability and the catalytic properties, in particular the coking behavior of Ni-based DRM catalysts at high reaction temperatures. The structural aging of the catalyst was simulated by repeated redox cycles of a hydrotalcite-derived Ni, Mg, Al catalyst. TPR/TPO cycles were found to gradually change the interaction of the redox-active Ni phase with the oxide support resulting in a crystalline Ni/$MgAl_2O_4$-type catalyst. Despite a very high Ni loading of 55.4 wt% and high reduction temperature of 800 °C, Ni nanoparticles of a size of only 11 nm were present in the initially prepared catalyst. After cycling the particle size was increased to 21 nm with an increased contribution of larger particles, bringing about a decrease in Ni surface area, while the majority of the particles were still relatively small.

These redox dynamics (TPR/TPO) and the related structural changes were found to have only a moderate influence on the activity in the DRM reaction at 900 °C. On the other hand, a significant decrease in coke deposition was observed after DRM in a fixed-bed reactor, mainly due to a lower fraction of graphitic carbon. Complementary DRM experiments performed in a thermobalance revealed that coke formation is a continuous process until a carbon limit of 123 wt% is reached and that the redox cycling leads to a faster approach to this limit.

Further studies for a deeper understanding of the microstructural changes during redox cycling and their positive effect on coking are needed and planned. The presented analytical methods will be used in the future to study, which structural features of Ni catalysts determine the coking rate in DRM at high temperatures and how they can be tuned by catalyst pretreatment with the goal to identify an operational window where coking on Ni catalysts can be suppressed to make them functional alternatives to noble-metal based DRM catalysts.

5.4 Material and methods

5.4.1 Synthesis conditions

The catalyst was prepared from a hydrotalcite-like (htl) precursor with the general formula $Ni_xMg_{0.67-x}Al_{0.33}(OH)_2(CO_3)_{0.17} \cdot mH_2O$ ($x = 0.5$) by constant pH co-precipitation. The amount of nickel was 50 mol%, and equates to a Ni-loading of 55.4 wt% in the final catalyst. The precipitation took place in an automated laboratory reactor (Mettler-Toledo Labmax) at T = 50 °C from aqueous 0.6 M NaOH, 0.09 M Na_2CO_3 solution and 0.4 M aqueous metal nitrate solution at pH 8.5. The precipitate was aged for 0.5 h in the mother liquor at 50 °C, filtrated, thoroughly washed with water until the conductivity of the filtrate was <0.5 mS $cm^{-1}$and dried at 100 °C over night. The obtained precursor was calcined in air at 600 °C for 3 h.

5.4.2 Characterization

Powder X-ray diffraction (XRD) measurements were performed using a Bruker D8 Advance reflection diffractometer equipped with a Lynx-Eye energy discriminating position sensitive detector (1D-PSD) using CuKα radiation. Kβ radiation was suppressed with a Ni-filter. Step scans were performed from 5 to 140° 2θ and a step size of 0.02° with a count time of 1 s step^{-1}.

Specific surface areas of the calcined material and the precursors were carried out by N_2 physisorption (Quantachrome Autosorb-6) and evaluated using the BET method. The samples were outgassed for 4 h at 80 °C.

Temperature-programmed reductions (TPR) of the sample (41 mg) were performed in a fixed-bed reactor (TPDRO-1100, CE Instruments). Prior to the TPR measurements, the sample was pretreated at 300 °C for 30 min in 5% O_2/He to remove moisture and other adsorbed impurities. The TPR measurements were performed up to 800 °C in 5% H_2/Ar (80 Nml min^{-1}), with a heating rate of 6 K min^{-1}, in a quartz tube. The final temperature was hold for 1 h. The H_2 consumption was monitored with a thermal conductivity detector (TCD). The TCD detector was calibrated by reducing a known amount of CuO. Likewise, the temperature-programmed oxidations (TPO) were performed up to 600 °C in 5% O_2/He (80 Nml min^{-1}), with a heating rate of 6 K min^{-1}, in a quartz tube. The final temperature was hold for 1 h.

To determine the nickel metal surface area, a H_2 pulse chemisorption method was applied. Therefore the samples were reduced in 5% H_2/Ar (80 Nml min^{-1}), with a heating rate of 6 K min^{-1} in a fixed-bed reactor. After cooling down to 50 °C in Ar, a defined volume of H_2 gas (100%) is introduced by pulse-dosing with a volume of 250 μl. The pulses were continued until no further uptake was detected. The Ni metal surface area was determined assuming a dissociative chemisorption mechanism of hydrogen (Sf = 2; 2Ni/H_2) [32].

The microstructure of the samples was examined by using Philips CM200 transmission electron microscopes (TEM) equipped with a LaB_6 cathode or a field electron gun. High-resolution images were taken with a CCD camera. For good statistics 40 to 80 images were taken for each sample on different agglomerates and regions of the catalysts. For the investigation of the microstructure of the activated catalysts the samples were reduced and subsequent passivated by slow increase of oxygen partial pressure at room temperature. For the investigation of catalysts after DRM the samples were reactivated by reduction and exposed to a second DRM run with the conditions described above to obtain the spent samples for microstructural characterization. After cooling down, the catalysts were separated from the dilutant by sieving. All samples were dispersed in chloroform and deposited on a holey carbon film supported on a copper grid.

Thermogravimetric experiments for the investigation of coking behavior have been performed in a Rubotherm thermobalance (DynTHERM). Prior the experiment 120 mg catalyst was reduced with 5 K min^{-1} at 800 °C in 5% H_2/Ar. Upon reaching the desired reaction temperature the system was purged in Ar for 1 h. Afterward, the DRM was performed at 900 °C in 120 Nml min^{-1} 40% CO_2/32% CH_4/Ar for 10 h. Subsequent to the reaction the carbonaceous deposits were oxidized in 21% O_2/Ar (214 Nml min^{-1}) and a linear heating rate of 5 °C min^{-1}. The final temperature of 800 °C was held for 1 h.

5.4.3 Catalytic performance

The catalytic experiments were performed in a continuous flow system at atmospheric pressure using a fixed-bed tubular quartz reactor of 8 mm inner diameter. For steady state measurements a calibrated on-line GC (Shimadzu 14-B) was used to analyze the product gas composition. For transient studies a coupled IR-detector (CO, CO_2 & CH_4) and a TCD for H_2 (Emerson MLT4 multichannel analyzer) and a paramagnetic O_2 detector (Magnos 16) were used.

For the catalytic test, 10 mg of the calcined catalyst (sieve fraction of 250–355 μm) was diluted with 490 mg of high purity SiC (sieve fraction of 125–180 μm). Initially, the catalyst was activated by reduction in 4% H_2/Ar (99.9%/99.999%) and a total flow of 20 Nml min^{-1} with a linear heating rate of 5 °C min^{-1}. The final temperature was held constant for 30 min. Afterward, the catalyst was heated to the reaction temperature of 900 °C in Ar (99.999%).The dry reforming reaction was carried out with a gas mixture consisting of CH_4 (99.9995%), CO_2 (99.9995%) and Ar in a ratio of 32:40:28. The total flow was set to 240 Nml min^{-1}. The reaction was performed at constant furnace temperature with a reaction time of 10 h. The reaction was followed by a holding period of 10 min and cooling in Ar for 2.5 h. In case the sample was not *ex situ* characterized by TEM directly after DRM, a subsequent TPO experiment was performed with a flow rate of 40 Nml min^{-1} of 4.5% O_2/Ar (99.995%/99.999%) and a linear heating rate of 5 °C min^{-1}. The final temperature of 800 °C was held constant until no more O_2 consumption was observed.

5.5 References

[1] M. Steinberg, *Int. J. Hydrogen Energy* **1999**, 24, 771–777.

[2] D. A. Lashof, D. R. Ahuja, *Nature* **1990**, 5, 529–531.

[3] R. Navarro, B. Pawelec, M. C. Alvarez-Galván, R. Guil-Lopez, S. Al-Sayari, J. L. G. Fierro, *Green Energy Technol.* **2013**, 137, 45–66.

[4] T. V. Choudhary, V. R. Choudhary, *Angew. Chem. Int. Ed.* **2008**, 47, 1828–1847.

[5] A. M. Gadalla, B. Bower, *Chem. Eng. Sci.* **1988**, 43, 3049–3062.

[6] Y. Lu, T. Lee, *J. Nat. Gas Chem.* **2007**, 16, 329–341.

[7] A. T. Ashcroft, A. K. Cheetham, M. L. H. Green, P. D. F. Vernon, *Nature* **1991**, 352, 225–226.

[8] S. Wang, G.Q. Lu, G. J. Millar, *Energy Fuels* **1996**, 10, 896–904.

[9] K. Mette, S. Kühl, H. Düdder, K. Kähler, A. Tarasov, M. Muhler, M. Behrens, *ChemCatChem* **2014**, 6, 100–104.

[10] M. C. J. Bradford, M. A. Vannice, *Catal. Rev.: Sci. Eng.* **1999**, 41, 1–42.

[11] M.-S. Fan, A. Z. Abdullah, S. Bhatia, *ChemCatChem* **2009**, 1, 192–208.

[12] Z. L. Zhang, X. E. Verykios, *Catal. Today* **1994**, 21, 589–595.

[13] S.-B. Tang, F.-L. Qiu, S.-J. Lu, *Catal. Today* **1995**, 24, 253–255.

[14] G. J. Kim, D.-S. Cho, K.-H. Kim, J.-H. Kim, *Catal. Lett.* **1994**, 28, 41–52.

[15] Y.-G. Chen, J. Ren, *Catal. Lett.* **1994**, 29, 39–48.

[16] J. Zielínski, *J. Catal.* **1982**, 76, 157–163.

[17] S. Sokolov, E. V. Kondratenko, M.-M. Pohl, U. Rodemerk, *Inter. J. Hydr. Ener.* **2013**, 38, 16121–16132.

[18] T. Davidian, N. Guilhaume, H. Provendier, C. Mirodatos, *Appl. Catal., A* **2008**, 337, 111–120.

[19] C. H. Bartholomew, R. J. Farrauto, *J. Catal.* **1976**, 45, 41–53.

[20] P. Salagre, J. L. G. Fierro, F. Medina, J. E. Sueiras, *J. Mol. Catal. A: Chem.* **1996**, 106, 125–134.

[21] J. M. Rynkowski, T. Paryjczak, M. Lenik, *Appl. Catal., A* **1993**, 106, 73–82.

[22] C. Li, Y.-W. Chen, *Thermochim. Acta* **1995**, 256, 457–465.

[23] H. Düdder, K. Kähler, B. Krause, K. Mette, S. Kühl, M. Behrens, V. Scherer, M.Muhler, *Catal. Sci. Technol.* **2014**, 4, 3317–3328.

[24] R. S. Weatherup, B. Dlubak, S. Hofmann, *ACS Nano* **2012**, 6, 9996–10003.

[25] A. Rinaldi, J. P. Tessonnier, M. E. Schuster, R. Blume, F. Girgsdies, Q. Zhang, T. Jacob, S. B. Abd Hamid, D. S. Su, R. Schlögl, *Angew. Chem. Int. Ed.* **2011**, 50, 3313–3317.

[26] R. S. Weatherup, B. C. Bayer, R. Blume, C. Baehtz, P. R. Kidambi, M. Fouquet, et al., *ChemPhysChem* **2012**, 13, 2544–2549.

[27] L. L. Patera, C. Africh, R. S. Weatherup, R. Blume, S. Bhardwaj, C. Castellarin-Cudia, A. Knop-Gericke, R. Schlögl, G. Comelli, S. Hofmann, C. Cepek, *ACS Nano* **2013**, 7, 7901–7912.

[28] F. Abild-Pedersen, J. Greeley, J.K. Nørskov, *Catal. Lett.* **2005**, 105, 9–13.

[29] S. Saadi, B. Hinnemann, S. Helveg, C. C. Appel, F. Abild-Pedersen, J. K. Nørskov, *Surf. Sci.* **2009**, 603, 762–770.

[30] M. Armbrüster, M. Behrens, F. Cinquini, K. Föttinger, Y. Grin, A. Haghofer, B. Klötzer, A. Knop-Gericke, H. Lorenz, A. Ota, S. Penner, J. Prinz, C. Rameshan, Z. Révay, D. Rosenthal, G. Rupprechter, P. Sautet, R. Schlögl, L. Shao, L. Szentmik-lósi, D. Teschner, D. Torres, R. Wagner, R. Widmer, G. Wowsnick, *ChemCatChem* **2012**, 4, 1048–1063.

[31] B. Steinhauer, M. R. Kasireddy, J. Radnik, A. Martin, *Appl. Catal., A* **2009**, 366, 333–341.

[32] M. Fadoni, L. Lucarelli, *Stud. Surf. Sci. Catal.* **1999**, 123, 289–342.

6 Summary & Final Conclusions

In this thesis the characteristics, reactivity and stability of Ni catalysts derived from Ni,Mg,Al hydrotalcite-like (htl) precursors were investigated for the high temperature dry reforming of methane (DRM).

Ni nanoparticles were stabilized at high temperature by the incorporation into a stable Mg,Al oxide matrix. Through the formation of both catalyst components from a single phase precursor a partial embedding of the Ni particles into the oxide was achieved, as well as strong interfacial interactions between the metal and the oxide. By their basic properties, high surface area and thermal stability, hydrotalcite-derived catalysts are suitable to resist carbon formation.

Initially a phase pure Ni,Mg,Al htl precursor was synthesized by co-precipitation, resulting in the following composition: $Ni_{0.5}Mg_{0.17}Al_{0.33}(OH)_2(CO_3)_{0.17} \cdot mH_2O$. Upon calcination in air a mixed oxide was formed, with Ni predominantly as $NiAl_2O_4$. After reduction, the resulting catalyst is characterized by a homogeneous metal distribution and small Ni particles of around 10 nm, which were embedded in an amorphous $MgAl_2O_4$-like matrix. Despite a high Ni loading of 50 mol%, this catalyst only showed minor sintering at 900 °C. This remarkable stability allows the operation at elevated temperatures. Two reaction temperatures were compared; 800 and 900 °C. In the DRM at 900 °C the catalyst showed an outstanding activity over 100 h. These conditions led to the formation of a less-fibrous carbon material and stable CH_4 conversion, compared to the lower reaction temperature. At higher temperatures, carbon formation is thermodynamically less favored.

To study the influence of structural and compositional properties, catalysts with different elemental compositions were prepared, extensively characterized and studied concerning their DRM performance and coking behavior. Therefore Mg was progressively substituted by Ni, resulting in Ni contents of 0 to 55 wt.-%. After reduction at 1000 °C, the resulting Ni/MgAl oxide catalysts exhibited average Ni particle sizes between 7 and 20 nm. The particle size was not directly related to the Ni content. The Ni surface area in contrast is decreasing as the Ni content is also decreasing. Despite similar particle sizes, a volcano-type correlation has been found between the Ni content and the Ni dispersion, with a maximum at 5 mol% Ni. By the employment of surface sensitive techniques (HR-TEM and IR), it was shown that an oxidic overgrowth is formed on the Ni particles. The overgrowth is interpreted as a nickel aluminate formed due to medium metal support interaction. At very high Ni concentrations (50 mol%) the particles are only partially covered. CO adsorption clearly indicates that in this case the surface is characterized by aggregated metallic Ni sites. In catalysts with lower Ni concentration the particles show a complete coverage. CO chemisorption showed predominant interaction with cationic sites and additionally some isolated metallic Ni sites.

The materials reactivity showed a dependency on the composition in the DRM reaction at 900 °C. Increasing integral degrees of methane conversion were detected with increasing Ni content and increasing metal surface area. Although all catalysts have shown low carbon formation, their performance was stable over the investigated 10 h of DRM. With decreasing Ni content the carbon formation decreases likewise. Between 10 and 1 mol% Ni a plateau is reached, where the amount of carbon formed is nearly constant. During the reaction, different carbon species were detected, depending on the metal loading and the reaction temperature. The carbon species were assigned to graphitic, filamentous (CNF) and less ordered carbon. At higher temperature and lower Ni content, the formation of non-deactivating graphite, originating from methane pyrolysis, is enhanced. At lower temperature and higher Ni content the formation of CNFs is favored, causing the continuous deactivation with time on stream. While initially only CNFs and less ordered carbon were formed, the formation of graphitic carbon based on CH_4 pyrolysis was enhanced with longer time on stream. Furthermore, it was shown that coke formation is a continuous process. Higher Ni contents and lower reaction temperatures gave rise to a significantly higher coking rate and total amount of carbon. The continuous coke formation implies that deactivation of the catalysts is probably not related to the total amount of carbonaceous deposits, but rather to the type of carbon formed. The carbon species can easily be removed by O_2 or CO_2 reestablishing the initial methane conversion.

The observed surface properties of the Ni based catalysts were used to propose a structure-performance-relationship. It is suggested that the overgrowth is the main reason for the attenuation of carbon formation observed for certain catalysts. The overgrowth can block extended metallic Ni sites that are nucleation centers for carbon formation. The presence of isolated Ni sites is able to preserve the DRM activity. On free metallic Ni agglomerates, however, the carbon formation is promoted by the growth of graphene islands. In an optimized catalyst the overgrowth will cover just enough of the metallic Ni surface that carbon formation is effectively blocked while the reaction can still proceed on the isolated sites.

The structural aging of the catalyst with 50 mol% Ni was simulated by repeated redox cycles. This allows to link structural stability and redox dynamics to coking propensity, decoupled from structural effects induced by coking, e.g. by enhanced metal mobility during carbon filament growth. Redox cycles gradually changed the interaction of the redox-active

Ni phase with the oxide support resulting in a crystalline Ni/$MgAl_2O_4$-type catalyst, with lower Ni-Al interactions. The particle size was increased from initially 11 nm to 21 nm, bringing about a decrease in Ni surface area. These structural changes had only a moderate influence on the reactivity in the DRM reaction at 900 °C. However, it resulted in a slight decrease in coke deposition during DRM in a fixed-bed reactor, mainly due to a lower fraction of graphitic carbon.

After decades of research, carbon formation over nickel based catalysts is still challenging and requires a systematic solution. Understanding the active sites for carbon formation may pave the way to improve the catalytic performance by rational approaches. The present work demonstrates the relevance of a detailed characterization of a series of materials at all stages of an applied catalyst preparation process as well as after the reaction. In future studies, the presented analytical methods can be used to identify the structural features of catalysts that determine the deactivation and how they can be tuned by catalyst preparation and pre-treatment. Especially the interplay of TG technique and fixed-bed investigations turned out to be a powerful tool to get insights into the change of the catalyst during the reaction and its catalytic activity. From the overall gained insights in this thesis it can be concluded, that a good catalyst have to make a compromise between activity and coke resistance, presumably due to an interplay of Ni dispersion, embedment and metal-support-interactions. With this knowledge an operational window might be identified where coking on Ni catalysts can be suppressed. Only under this precondition it will be possible to make nickel a functional alternative to noble-metal based DRM catalysts.

List of figures

List of SI figures

List of tables

List of SI tables

Appendix

List of Publications included in the Thesis

Katharina Mette, Stefanie Kühl, Hendrik Düdder, Kevin Kähler, Andrey Tarasov, Martin Muhler, Malte Behrens; S*table Performance of Ni Catalysts in the Dry Reforming of Methane at High Temperatures for the Efficient Conversion of CO_2 into Syngas*; ChemCatChem 2014, 6, 100–104.
DOI: 10.1002/cctc.201300699

Hendrik Düdder, Kevin Kähler, Bastian Krause, Katharina Mette, Stefanie Kühl, Malte Behrens, Viktor Scherer, Martin Muhler; *The role of carbonaceous deposits in the activity and stability of Ni-based catalysts applied in the dry reforming of methane*; Catalysis Science & Technology 2014, 4, 3317–3328.
DOI: 10.1039/c4cy00409d

Katharina Mette, Stefanie Kühl, Andrey Tarasov, Hendrik Düdder, Kevin Kähler, Martin Muhler, Robert Schlögl, Malte Behrens; *Redox dynamics of Ni catalysts in CO_2 reforming of methane*; Catalysis Today 2015, 242, 101–110.
DOI:10.1016/j.cattod.2014.06.011